

**MACHINABILITY ANALYSIS OF ALUMINUM-CAST IRON (AlSi-GCI)
BIMETALLIC COMPONENTS THROUGH EXPERIMENTAL AND
NUMERICAL STUDIES**

MACHINABILITY ANALYSIS OF ALUMINUM-CAST IRON (AlSi-GC)
BIMETALLIC COMPONENTS THROUGH EXPERIMENTAL AND NUMERICAL
STUDIES

By

ABDULELLAH HBBANI, B.Sc.

(King Fahd University of Petroleum and Minerals, Saudi Arabia)

A Thesis

Submitted to the School of Graduate Studies

in Partial Fulfilment of the Requirements

for the Degree

Master of Applied Science

McMaster University

© Copyright by Abdullellah Hbbani, August 2019

MASTER OF APPLIED SCIENCE (2019)

McMaster University

(Mechanical Engineering)

Hamilton, Ontario

TITLE: MACHINABILITY ANALYSIS OF ALUMINUM-CAST
IRON (AlSi-GCI) BIMETALLIC COMPONENTS
THROUGH EXPERIMENTAL AND NUMERICAL
STUDIES

AUTHOR: Abdullellah Hbbani, B.Sc.

SUPERVISOR: Dr. Stephen Veldhuis

Department of Mechanical Engineering

McMaster University

NUMBER OF PAGES: 101

Abstract

This thesis includes experimental and numerical investigations to study the machinability of the dry finish turning of an AlSi-GCI (JIS ADC 12- ASTM A48 class 40) bimetallic workpiece with CBN cutting tools by studying tool life, wear behaviour, cutting forces, and workpiece surface roughness. This involved the development of a novel experimental setup that captured the fluctuating cutting forces associated with bimetal parts on the cutting tool. In addition, a numerical finite element method (FEM) model was also developed to investigate the thermo-mechanical behaviour of the CBN cutting tool and simulate the bimetal turning process under different cutting conditions. Finally, a study to reduce the cutting forces was conducted using Taguchi's design of experiment (DOE) approach, which was studied numerically with FEM and validated experimentally. This was done to serve as a model approach that can be applied to study unique machining conditions in the future. The findings of the machinability study comparing two different tool geometries are presented along with the results of the machinability improvement study.

Acknowledgements

First and foremost, I would like to thank God Almighty for giving me the strength, knowledge, ability and opportunity to conduct and complete this research satisfactorily.

I would like to express my appreciation to my supervisor Dr. Stephen C. Veldhuis for giving me the opportunity to work under his supervision in McMaster Manufacturing Research Institute (MMRI) and for his support and guidance throughout my MASc journey. I would also like to thank the Natural Sciences and Engineering Research Council of Canada (NSERC) under the CANRIMT Strategic Research Network for supporting this research (Project# NETGP 479639 - 15).

As a student of the MMRI, I would like to acknowledge Honda of Canada Manufacturing for their collaboration and support to this research. Also, my special thanks and gratitude to Dr. Abul Fazal Arif for his immense support and guidance. He greatly enriched this research with his technical and planning guidance. Also, I would like to thank Mr. Simon Oomen-Hurst and Mr. Ahmed Sweed from the MMRI for their contribution to this industrial research with their technical support and invaluable guidance.

Special thanks to my mother, father, fiancé and friends for their immense support throughout the MASc journey in Canada.

Table of Contents

Abstract	ii
Acknowledgements.....	iii
Table of Contents	iv
List of Figures	ix
List of Tables	1
List of all Abbreviations and Symbols.....	2
Declaration of Academic Achievement	3
Chapter 1. Introduction	1
1.1 Background	1
1.2 Motivation	2
1.3 Research Objectives	2
1.4 Research Methodology.....	3
1.5 Thesis Outline	4
Chapter 2. Literature Review	6
2.1 Machining.....	6
2.1.1 Machining Terminologies.....	6
2.2 Tool Wear.....	8
2.2.1 Types of Tool Wear.....	8

2.2.2 Tool Wear Mechanisms	11
2.3 GCI (GCI)	13
2.3.1 GCI overview and industrial applications	13
2.3.2 Tool wear mechanisms of GCI.....	14
2.3.3 Cutting tools for GCI machining	14
2.3.4 Special characteristics of GCI machining.....	14
2.4 AlSi casting alloys.....	15
2.4.1 AlSi overview and industrial applications	15
2.4.2 Wear mechanisms of AlSi	15
2.4.3 Cutting tools for AlSi machining.....	16
2.5 Bimetal machining of AlSi-GCI	16
Chapter 3: Experimental Procedures.....	21
3.1 Cutting tool design and material properties	21
3.2 Workpiece material properties & design.....	22
3.2.1 Materials of the AlSi-GCI bimetal workpiece:.....	22
3.2.2 Design of AlSi-GCI bimetal workpiece:	23
3.2.3 Manufacturing of AlSi-GCI bimetal workpiece:	28
3.3 Experimental setup & Machining conditions.....	29
3.4 Force measurement	30

3.5 Tool wear & Workpiece surface roughness measurements	32
3.5.1 Flank wear measurement	32
3.5.2 Adhesion measurement.....	33
3.5.2 Workpiece roughness measurement	33
Chapter 4: Numerical & Statistical procedures.....	35
4.1 The Finite Element Numerical Model.....	35
4.1.1 Finite element model	35
4.1.2 FE model calibration.....	40
Chapter 5: Experimental Studies	42
5.1 Tool Design 1	42
5.1.1 Tool life	42
5.1.2 Tool wear behaviour.....	43
5.1.3 Cutting Forces:.....	53
5.1.4 Surface roughness:.....	56
5.2 Tool Design 2.....	58
5.2.1 Tool life	58
5.2.2 Tool Wear behaviour	58
5.2.3 Cutting Forces:.....	65
5.2.4 Surface roughness:.....	67

5.3 Comparison	68
5.3.1 Tool life	70
5.3.2 Wear behaviour.....	70
5.3.3 Cutting forces.....	70
5.3.4 Surface roughness.....	71
 Chapter 6 NUMERICAL INVESTIGATIONS & MACHINABILITY IMPROVEMENT	 72
6.1 Impact of tool design on thermo-mechanical behaviour.....	72
6.1.1 Tool Design 1	72
6.1.2 Tool Design 2	76
6.1.3 Discussion and Comparison	79
6.2 Numerical study on machinability improvement.....	81
6.2.1 Taguchi's DoE:.....	81
6.2.2 DOE setup.....	86
6.2.3 Parametric study- Results and Discussion.....	88
6.2.4 Experimental validation.....	92
 Chapter 7. Conclusions & Future Work	 95
7.1 Conclusions	95
7.2 Future work	97

References98

List of Figures

Fig. 1 Various bimetal applications (a) piston, (b) engine liner and (c) journal bearing. ...	1
Fig. 2 Lathe turning showing a vertical cross-section (reprinted with permission [1]).....	7
Fig. 3 Types of tool wear [5]	9
Fig. 4 Typical tool flank wear stages [5]	10
Fig. 5 SEM images of failed CBN tool (reprinted with permission [19])	17
Fig. 6 (a) Cutting forces for AlSi, (b) Cutting forces for GCI (reprinted with permission [19]).....	17
Fig. 7 AlSi-GCI Piston used for bimetal machining study [20].....	18
Fig. 8 Cast Iron-Steel bimetal crankshaft bore	18
Fig. 9 Overall geometry of the CBN cutting tool	21
Fig. 10 Tool cutting edge geometry (a) unprepared edge (b) prepared honed edge	22
Fig. 11 Reaming & Milling Setup.....	24
Fig. 12 Proposed turning setup	25
Fig. 13 Manufactured AlSi-GCI bimetal workpiece a) Front view (b) Side view.....	28
Fig. 14 Machining setup	30
Fig. 15 (a) Kistler 9121 piezo-electric dynamometer (b) Directions of force components	31
Fig. 16 LabView force acquisition interface.....	31
Fig. 17 Force signal sample measurement (Radial component)	32
Fig. 19 Mitutoyo roughness tester sj-201	34

Fig. 20 (a) Idealization of 3D into 2D model. (b) Geometrical model interface in AdvantEdge.....	36
Fig. 21 (a) Variation in numerical force components, (b) Variation in experimental force components, (c) Comparison of average numerical cutting force against experimental, (d) Comparison of average numerical feed force against experimental	40
Fig. 22 Flank wear progression with cutting length (Tool Design 1).....	43
Fig. 23 Cutting zone of the CBN cutting tools	44
Fig. 24 SEM analysis of the CBN cutting tool	48
Fig. 25 SEM and EDS analysis of cutting tool (a) cutting edge, (b) Chip evacuation zone	52
Fig. 26 Accumulation of adhesion on the cutting edge with respect to cutting length.	53
Fig. 27 Variation in force components (a) cutting force, (b) feed force, (c) radial force, and (d) difference in force (Tool Design 1).....	55
Fig. 28 Progression of Z value with respect to cutting length (Tool Design 1).....	56
Fig. 29 Variation in surface roughness of machined surface (Tool Design1)	57
Fig. 30 Flank wear progression with cutting length (Tool Design 2).....	58
Fig. 31 SEM analysis of Tool Design 2	61
Fig. 32 SEM and EDS analysis of Tool Design2 (a) cutting edge, (b) Chip evacuation zone	64
Fig. 33 Accumulation adhesion on the cutting edge with respect to cutting length.	65
Fig. 34 Variation in force components (a) cutting force, (b) feed force, (c) radial force, and (d) difference in force (Tool Design 2).....	66

Fig. 35 Progression of Z value with respect to cutting length (Tool Design 2).....	67
Fig. 36 Variation in surface roughness of machined surface (Tool Design 2)	68
Fig. 37 Variation of maximum tool temperature with respect to time (Tool Design1)	73
Fig. 38 Cutting tool temperature distribution on rake face (a) AlSi and (b) GCI (Tool Design 1).....	74
Fig. 39 Mechanically induced stresses during cutting process (a) AlSi and (b) GCI (Tool Design 1).....	75
Fig. 40 Variation of maximum tool temperature with respect to time (Tool Design 2) ...	76
Fig. 41 Cutting tool temperature distribution on rake face (a) AlSi and (b) GCI (Tool Design 2).....	77
Fig. 42 Mechanically induced stresses during cutting process (a) AlSi and (b) GCI (Tool Design 2).....	78
Fig. 43 Effect of process parameters on average S/N ratios for ΔF_c	90
Fig. 44 Variation in force components (a) cutting force, (b) feed force, (c) radial force, and (d) difference in force.	92
Fig. 45 Progression of Z value with respect to cutting length	93

List of Tables

Table 1 Tool specification and geometry.....	22
Table 2 Chemical composition of AlSi and GCI. [10]	23
Table 3 Mechanical properties of AlSi and GCI.....	23
Table 4 Comparison of material efficiency of different Setups.....	25
Table 5 Comparison of experimental setup criteria.....	27
Table 6 Optical images of wear and adhesion progression with respect to cutting length (Tool Design 1).....	45
Table 7 Optical images of wear and adhesion progression with respect to cutting length (Tool Design 2).....	59
Table 8 Machinability comparison of Tool 1 against Tool 2.....	69
Table 9 Temperature comparison of Tool Design 1 against Tool Design 2.....	79
Table 10 Von Mises stresses comparison of Tool Design 1 against Tool Design 2.....	81
Table 11 ANOVA computations	85
Table 12 Cutting parameters and their levels.....	87
Table 13 Orthogonal array of Taguchi $L_{16}(4^3)$	88
Table 14 The results of experiments and S/N ratios	89
$S/N_{average}, \Delta F_c = -4.86 + -4.19 + -0.91 + (-3.29)^4 = -3.31$ Table 15 S/N response table for ΔF_c factor.....	89
Table 16 Results for ANOVA for ΔF_c	91
Table 17 Comparison of ΔF for f_1 and f_2	94

List of all Abbreviations and Symbols

AlSi – Aluminum Silicon

GCI – Gray cast iron

CBN – Cubic boron nitride

BUE – Built up edge

BUL – Built up layer

f – Feed

V – Cutting speed

SEM – Scanning electron microscopy

EDS – Energy dispersive spectroscopy

Declaration of Academic Achievement

I, Abdullellah Hbbani, declare that the thesis entitled “MACHINABILITY ANALYSIS OF ALUMINUM-CAST IRON (AlSi-GCI) BIMETALLIC COMPONENTS THROUGH EXPERIMENTAL AND NUMERICAL STUDIES” is my own work and that I am the sole author of this thesis.

Chapter 1. Introduction

1.1 Background

Bimetal machining is metal cutting performed with a single cutting tool under the same cutting conditions on a workpiece composed of two different bulk materials joined together without any changes to their individual properties. Bimetallic components are usually made of materials that strongly differ in their mechanical, chemical, and thermal properties. This is mainly done to leverage each material's properties to enhance product performance. Bimetal components play a significant role in many engineering fields, such as automotive, power generation, and construction equipment industries [1]. AlSi alloys have been widely used by different automotive manufacturers to produce engine blocks, heads and other components. To improve the performance of these lightweight aluminum components, materials such as cast iron have been introduced to different engine parts that need high strength and temperature resistance. Fig. 1 shows multiple AlSi engine components reinforced with GCI at various selected locations.

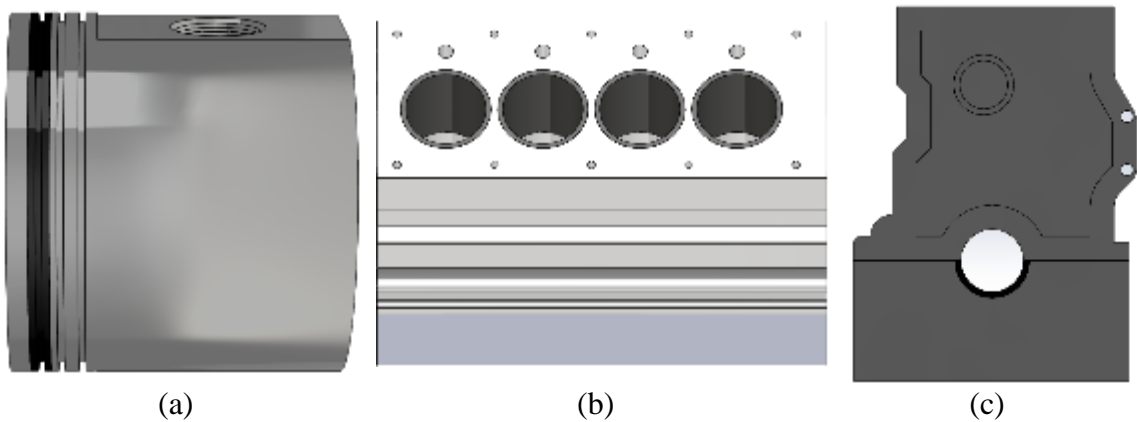


Fig. 1 Various bimetal applications (a) piston, (b) engine liner and (c) journal bearing.

Bimetal engine components require extremely precise machining processes to meet design and performance criteria. Since bimetal components are made of materials with highly divergent properties, their machinability challenges will be discussed in the next chapter. The machinability of AlSi-GCI is investigated by studying tool life, wear behaviour, cutting forces, and workpiece surface roughness.

1.2 Motivation

Despite their importance, there is a limited amount of literature concerning the machinability challenges of bimetallic components. The present research strives to develop an in-depth knowledge profile of bimetallic component machinability. The focus of this research specifically concerns the machinability of an AlSi-GCI workpiece with CBN cutting tools, striving to elucidate the process of bimetal machining and its fluctuating cutting conditions, to enhance cutting tool life, process productivity and produced part quality.

1.3 Research Objectives

Areas that require investigation are identified based on past scientific studies on the machinability of bimetallic components, specifically those of AlSi-GCI reported in Chapter 2. A robust experimental setup and procedure are proposed with which to investigate bimetallic machining. An in-depth cutting performance analysis of tool life, cutting forces, and workpiece surface quality is conducted. Furthermore, the impact of tool geometry on the productivity of machining bimetal components is investigated, along with numerical modeling of bimetallic machining.

The main objective of this research is to assess the cutting performance of bimetallic AlSi-GCI under different cutting conditions with the goal of enhancing the overall cutting performance and process productivity. More specifically, the main objective is divided into three stages:

1. Develop an experimental approach to study the machinability of AlSi-GCI bimetallic components.
2. Investigate the effect of CBN tool design on the machinability of the AlSi-GCI bimetallic workpiece.
3. Improve the machinability of the AlSi-GCI bimetallic workpiece.

1.4 Research Methodology

The research methodology and expected studies to meet the thesis objectives are as follows:

1 st Objective	Literature review. Develop an experimental setup.
2 nd Objective	Conduct a machinability experimental study with Tool 1. Conduct a machinability experimental study with Tool 2.
3 rd Objective	Develop an FEA model with AdvantEdge. Calibrate the FEA model. Study the thermo-mechanical behaviour of bimetals machining with the developed FEA model. Develop a Taguchi design of experiment to improve bimetals machinability. Study the Taguchi design numerically and validate it experimentally.

1.5 Thesis Outline

This thesis is organized into seven different chapters, whose contents are summarized as follows:

CHAPTER 1: INTRODUCTION – Motivation and objectives of the current research are introduced.

CHAPTER 2: LITERATURE REVIEW – A detailed overview is provided of the properties, advantages and machining challenges of GCI and AlSi casting alloys as well as a review of scientific literature concerning bimetal machining. In addition, different cutting tool materials, dry-machining, metal working fluids and tool coatings are considered.

CHAPTER 3: EXPERIMENTAL PROCEDURE – The methodology, cutting tools, conditions and parameters of the cutting test experimental setup are provided. Numerical studies performed using Third Wave System's AdvantEdge software are also presented.

CHAPTER 4: NUMERICAL & STATISTICAL PROCEDURES – The Numerical model along with statistical methods used during the machinability study and improvement are introduced.

CHAPTER 5: EXPERIMENTAL STUDIES – Experimental results of the cutting forces, temperature, surface integrity and tool analysis are provided. This chapter also includes data analysis.

CHAPTER 6: NUMERICAL INVESTIGATIONS & MACHINABILITY IMPROVEMENT – Numerical results of the machinability study, parametric study and experimental validation are provided.

CHAPTER 7: CONCLUSION & FUTURE WORK – The significant findings of this study and the corresponding conclusions and recommendation for future directions for AlSi-GCI bimetallic machining studies are outlined.

Chapter 2. Literature Review

2.1 Machining

Machining is a generic term used in metal cutting to refer to controlled material removal processes, such as turning, milling and drilling, in which unnecessary material is removed from the bulk metal in the form of chips to obtain a desired final geometry. A cutting process occurs during machining when the cutting tool moves through the workpiece with a relative motion. Turning operations were used in the present research. During turning, the workpiece is fixed in a chuck and the cutting tool is held rigidly in a tool holder. Cutting occurs when the chuck is rotated and the tool holder is moved at a constant rate along the axis of the workpiece, cutting away a layer of metal to form a cylindrical geometry. Fig. 2 shows the lathe turning process with a vertical cross-section.

2.1.1 Machining Terminologies

The common terminologies used in machining are defined below:

Cutting speed:

Cutting speed (V), also known as surface speed, is defined as the relative velocity at which the cutting edge of a cutting tool passes over the surface of the workpiece per unit time. Unit: m/min

Feed or Feed rate:

Feed (f) is defined as the velocity at which the cutting tool is advanced into the workpiece along its length. Unit: mm/rev or mm/min

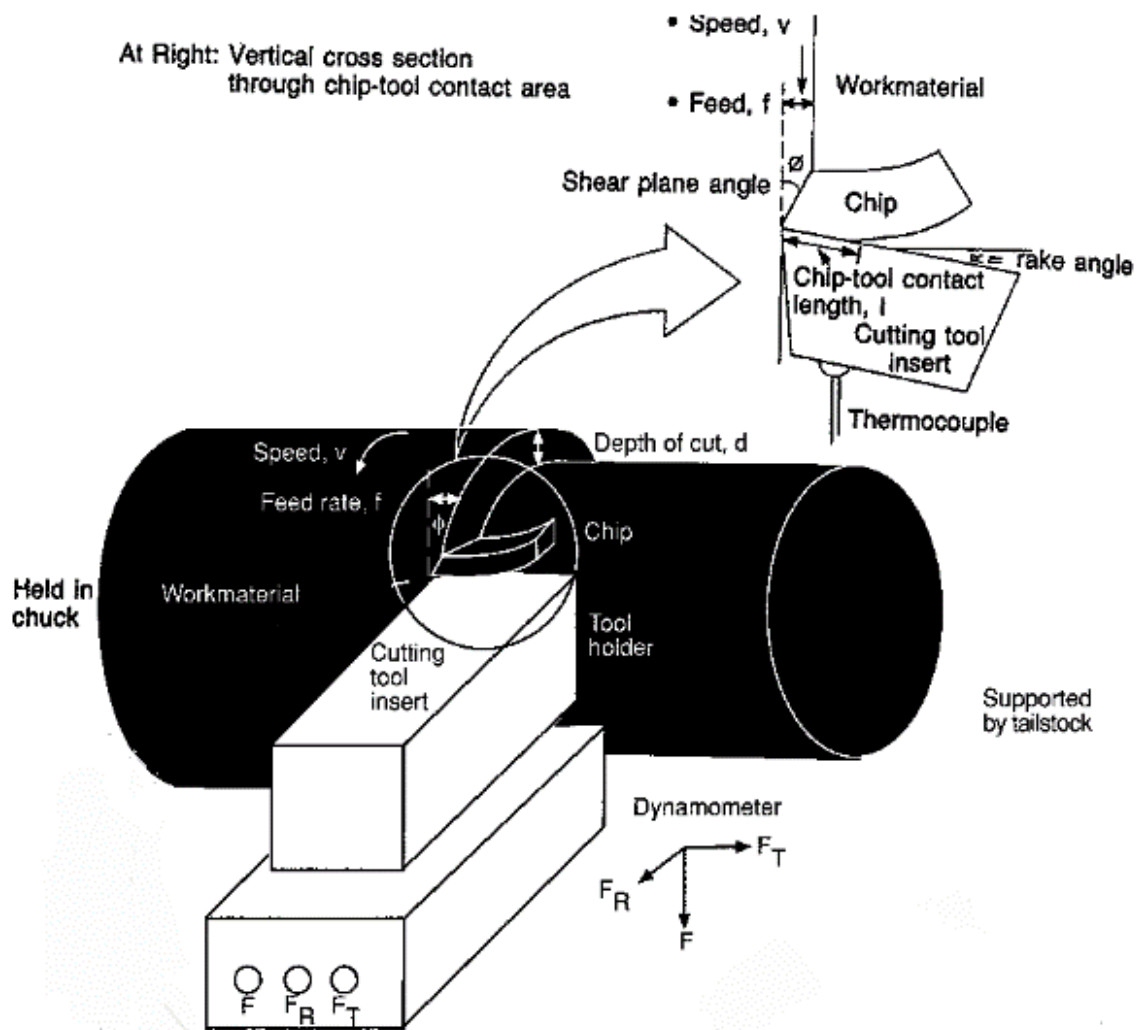


Fig. 2 Lathe turning showing a vertical cross-section (reprinted with permission [1])

Depth of cut:

Depth of cut (DoC) is the thickness of the material layer along the cutting edge. More specifically, it is the uncut chip width. Unit: mm

Rake angle:

Rake angle (α) is the angle between the rake face of the cutting tool and the normal line to the workpiece at the cutting edge.

Clearance angle or relief angle:

Clearance angle is the angle between the flank face of the cutting tool and the workpiece surface.

2.2 Tool Wear

Tool wear can be defined as the gradual degradation in cutting tool geometry during cutting, as a result of the gradual loss of tool material [2]. Tool wear is inevitable in all machining processes and is dictated by several factors, such as relative sliding velocity, stress and temperature generated at the contact surface. It impedes process productivity, dimensional accuracy, and product surface quality. Therefore, it is highly important to reduce tool wear in all machining processes.

Tool wear is mainly affected by the four factors listed below [3]:

- 1- Properties and microstructure of the workpiece material that determine the cutting forces on the cutting tool.
- 2- The tool-workpiece interface condition, which can be influenced by cutting fluids that decrease the temperature and ultimately the tool wear.
- 3- The tool material (substrate and coating), tool geometry, and cutting parameters. These factors should be appropriately selected to obtain the optimum cutting performance.
- 4- The stability of machine tool dynamics.

2.2.1 Types of Tool Wear

There are several types of tool wear, according to the ISO standard 3685:1993. The types of wear relevant to this research, shown in Fig. 3, are as follows:

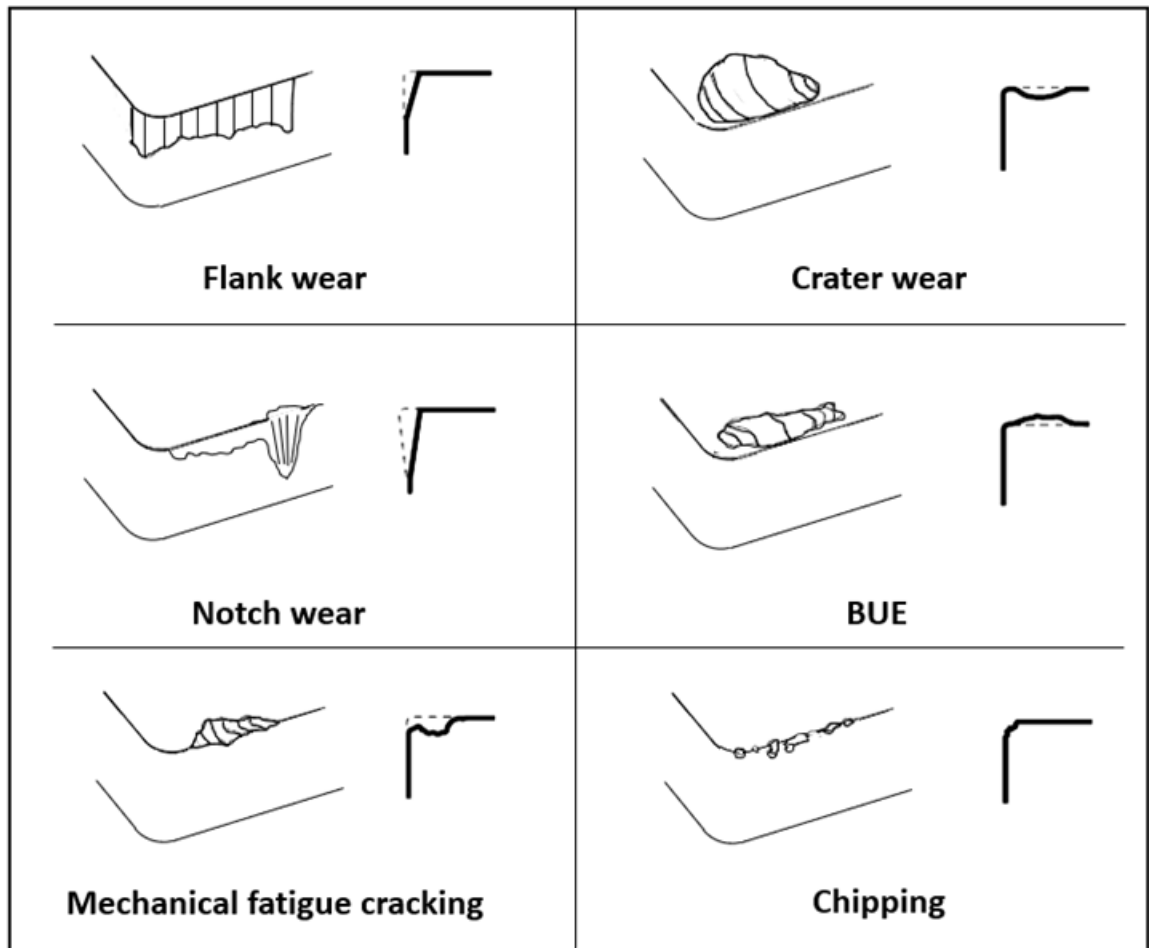


Fig. 3 Types of tool wear [5]

Flank Wear:

Flank wear is defined as the erosion on the flank (relief) face of the tool due to plastic deformation. When the material at the flank surface is removed, the wedge angle of the tool is reduced, which weakens the tool, increasing the cutting-edge contact area with the workpiece. This, in turn, causes the growth of frictional heat generation [4]. The leading cause of flank wear is abrasive wear. Flank wear reduces workpiece surface quality, i.e., dimensional accuracy and hampers surface integrity of the machined part. According to ISO 3685:1993 and ISO 8688-2:1989, the tool failure criterion is set to be 300 μm of flank

wear. **Error! Reference source not found.** shows the different stages of the flank wear progression curve.

Crater Wear:

Crater wear occurs as a result of the wear mechanisms, diffusion, abrasion, and adhesion, that take place between the tool and the chip as it sticks and passes over the rake face of the tool, thereby weakening the cutting edge. Crater depth, K_T , is most commonly used to quantify the crater wear.

Notch Wear:

Notch wear is localized damage on both the rake and flank faces at the depth of cut line. It occurs due to oxidation, adhesion and a deformation-hardened surface.

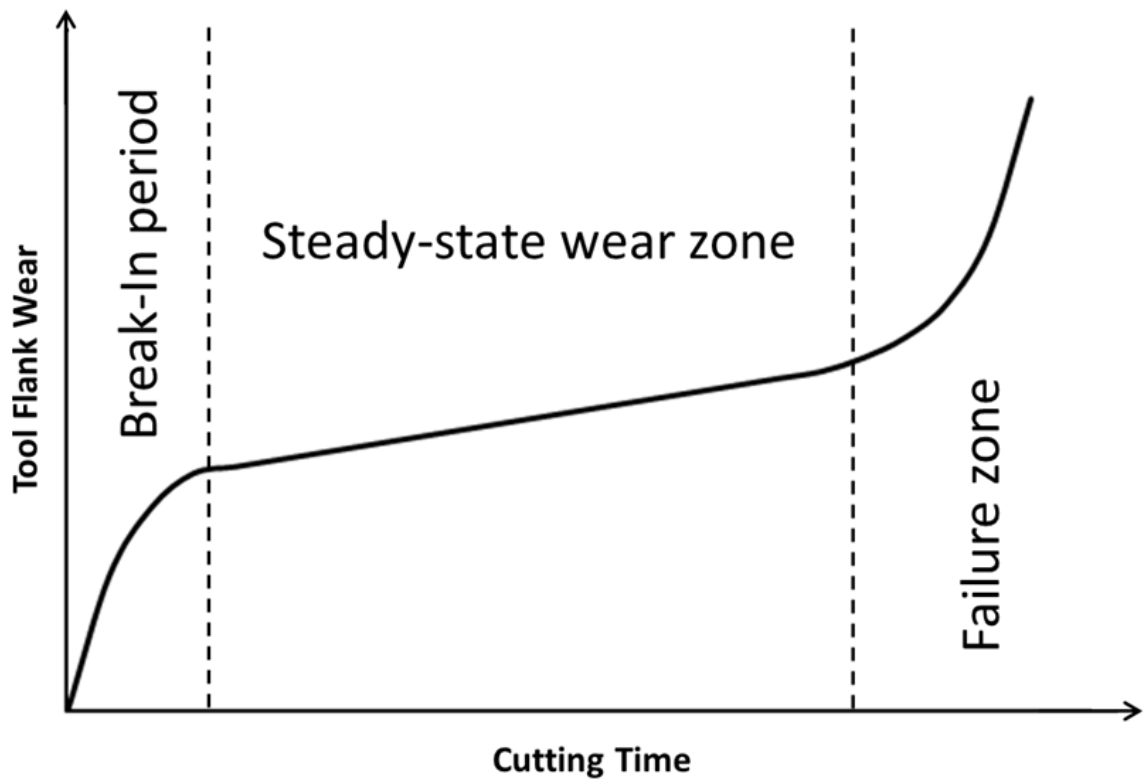


Fig. 4 Typical tool flank wear stages [5]

Built up edge (BUE):

BUE is defined as workpiece material adhering to the cutting edge of the tool. It changes the dimension of the cutting tool and consequently that of the workpiece cut surface. Moreover, as the BUE breaks off upon reaching a critical size, it often carries off a part of the tool material with it, causing edge chipping.

Thermal and Mechanical fatigue:

Thermal and mechanical fatigue occur due to cyclic thermal and mechanical loads on the tool. These modes are more prominent in intermittent cutting processes, such as milling, in which the cutting tool is subjected to alternating heating-cooling and cutting force cycles. Tool wear occurs as a result of crack propagation along the cutting edge caused by the cyclic loads.

Chipping:

Chipping occurs when chunks of material are discretely removed from the cutting tool edge. It depends on the brittleness of the cutting tool and its failure to withstand cyclic loads. Chipping is promoted by discontinuous cutting conditions and BUE formation.

2.2.2 Tool Wear Mechanisms

The wear types outlined above are caused by different wear mechanisms. The incidence of a wear mechanism depends on various metrics, such as the cutting process type, workpiece material, and thermomechanical behaviour. The common wear mechanisms are briefly described below:

Abrasive Wear:

Abrasive wear is when the cutting edge is scratched by hard abrasive particles present in the workpiece material. Abrasion is the most common wear mechanism that primarily happens on the flank face of the tool. It uniformly appears at various locations along the cutting-edge surface.

Adhesion Wear:

Adhesion wear, also known as attrition, is the adherence of workpiece material on the cutting edge due to friction, high temperatures and pressures in the cutting zone. The adhered material is unstable and has a tendency to randomly break away, removing tool fragments along with it. A significant amount of adhered material is known as a built-up edge. Adhesion is commonly evident on both the flank and rake faces. Wear volumes related to adhesion are typically lower as compared to abrasion.

Diffusion Wear:

Diffusion wear arises due to chemical interaction between the tool and the workpiece. Cutting tool and workpiece material components diffuse into each other and generate smooth wear on the rake face, where the cutting temperature is at the maximum. The diffusion rate is proportional to the chemical affinity between the tool and work material, cutting temperature, and the diffusion concentration gradient.

Oxidation Wear:

Oxidation wear occurs near the tool surface due to oxidation of tool components such as tool binder. At high temperatures and pressures, oxygen reacts with the tool material, generating this type of wear. Oxidation wear typically results in depth-of-cut notch wear,

which is a localized, severe wear corresponding to the point of maximum depth of cut (uncut chip width).

Fatigue Wear:

Fatigue wear can be addressed as either mechanical or thermal, based on the nature of the loading. Mechanical fatigue takes place due to cyclic compressive and tensile loading on the cutting tool, whereas thermal fatigue occurs as a result of alternating expansion and contraction. Mechanical and thermal fatigue then promote crack propagation, contributing to tool fracture.

2.3 GCI (GCI)

2.3.1 GCI overview and industrial applications

Cast Iron has been produced since the 14th century C.E., following the invention of the shaft furnace. Cast Iron has seen widespread use in industry due to its relatively high mechanical properties, low cost, excellent castability and high machinability [1]. GCI is a desirable component of machine tools, engine parts and measuring equipment due to its high damping capacity [5]. In 2009, a survey conducted by Modern Casting [6] reported GCI to be the most cast material with 37.6 million tons cast, followed by ductile iron and steel at 19.9 and 9.0 million tons cast, respectively. GCI possesses the best combination of machinability and mechanical properties among cast irons. The machinability advantages of GCI include low power requirements, good surface finish and desirable chip breakability. These beneficial factors are attributed to the GCI graphite phase, which contributes to the free-machining nature of the material [1]. The only detractor is its

relatively high mass density which makes it less attractive for automotive applications where light weighting is an increasing objective.

2.3.2 Tool wear mechanisms of GCI

The main tool wear mechanisms of GCI are oxidization and diffusion [7]. When GCI is cut at high speeds, CBN and its binder are not chemically stable at elevated temperatures. Under such conditions, the CBN breaks down forming boron (B) and nitrous oxides. Binder phases, such as TiC or Ti are also oxidized. Conversely, B and Ti from the cutting tool are found to be diffused in GCI, indicating the decomposition of boron and titanium-containing phases in the cutting tool.

2.3.3 Cutting tools for GCI machining

Coated carbides are most commonly used cutting tools for machining GCI at relatively low cutting speeds (200–300 m/min) under wet conditions. However, CBN has gained a reputation as the best tool material to machine GCI, due to its significantly higher tool life at cutting speeds of 800–2500 m/min under continuous, intermittent, and dry cutting conditions [7–10]. Ceramic inserts are positioned as an intermediate option between coated carbides and CBN in terms of machining performance and cost-effectiveness [11,12]. Nevertheless, they are not suitable for intermittent and wet cutting due to their low impact and thermal shock resistance.

2.3.4 Special characteristics of GCI machining

It is generally known that tool life decreases with a rise in cutting speed. However, in some materials, thin films, also known as tribo-films, are generated between the cutting tool and the workpiece under specific cutting conditions, thereby forming a lubricating

layer that actually enhances tool life. It has been shown that an MnS layer formed on the tool at cutting speeds in excess of 400 m/min, protects the tool and significantly improves the tool life [8][7].

2.4 AlSi casting alloys

2.4.1 AlSi overview and industrial applications

AlSi Casting Alloys have gained popularity due to their high strength-to-weight ratios (about three times higher than that of steel), high machinability and fabricability and high corrosion resistance properties in different environments [13].

AlSi casting alloys have been widely employed in various industries to reduce the weight of the parts and increase their performance and efficiency. For example, AlSi casting alloys are commonly used for automobile engine blocks, gearboxes, aerospace castings, consumer products, marine and architectural applications [13,14].

2.4.2 Wear mechanisms of AlSi

The main wear mechanisms of AlSi alloys are adhesion and abrasion. In adhesion, AlSi sticks to the cutting tool due to the heat generated by friction between the tool and workpiece. It was found that the adhesion layer is observed to form at specific combinations of speeds and normal loads, especially at a high load and low speed. The adhesion of AlSi on the cutting tool becomes more significant under dry cutting conditions and higher temperatures, due to the absence of cutting fluids [15]. Conversely, abrasion on the cutting tool is caused by the presence of hard silicon particles [16].

2.4.3 Cutting tools for AlSi machining

PCD and carbide tools are commonly used to machine Al-Si alloys. However, a study by Ng et al. [17] showed that carbide tools experience edge rounding due to hard silicon particles affecting the surface integrity of the cutting edge. In contrast, PCD is better for machining Al-Si alloys, since it is much harder than carbide, making it more resistant to edge rounding wear caused by the hard silicon particles [17] [18].

2.5 Bimetal machining of AlSi-GCI

Bimetal machining is metal cutting performed with a single cutting tool under equal conditions on a workpiece made from two different bulk materials that are joined without any changes to their properties.

There is a limited number of studies concerning bimetal AlSi-GCI machining. In 2013, Malakizadi et al. [19] briefly analyzed cutting tool failure during the machining of an AlSi-GCI engine block with a CBN cutting tool and studied the cutting forces of two separately machined materials, as shown in Fig. 5 and Fig. 6, respectively. This paper reported numerical studies that separately modelled 3D-milling for each material. However, a thorough analysis of tool life, fluctuating cutting forces, tribofilms and workpiece surface integrity, along with numerical studies of the materials themselves were not presented in this research.

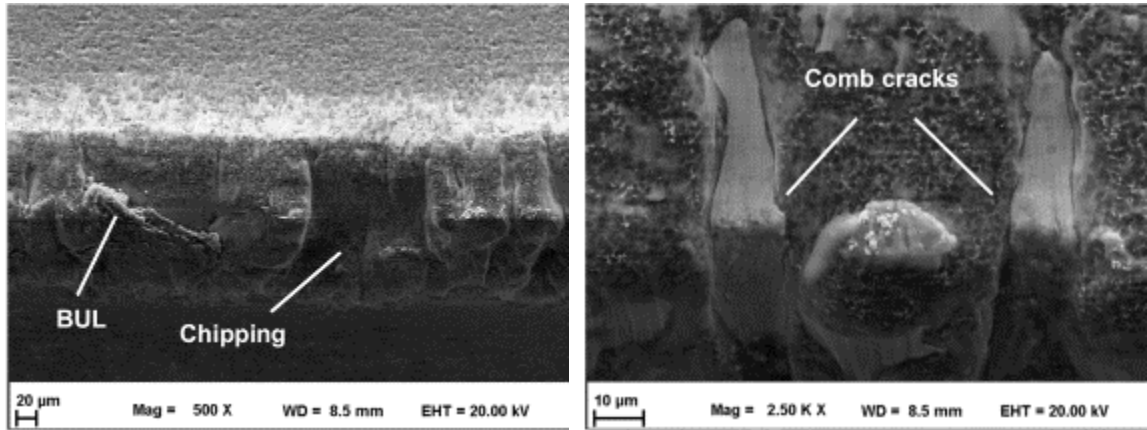


Fig. 5 SEM images of failed CBN tool (reprinted with permission [19])

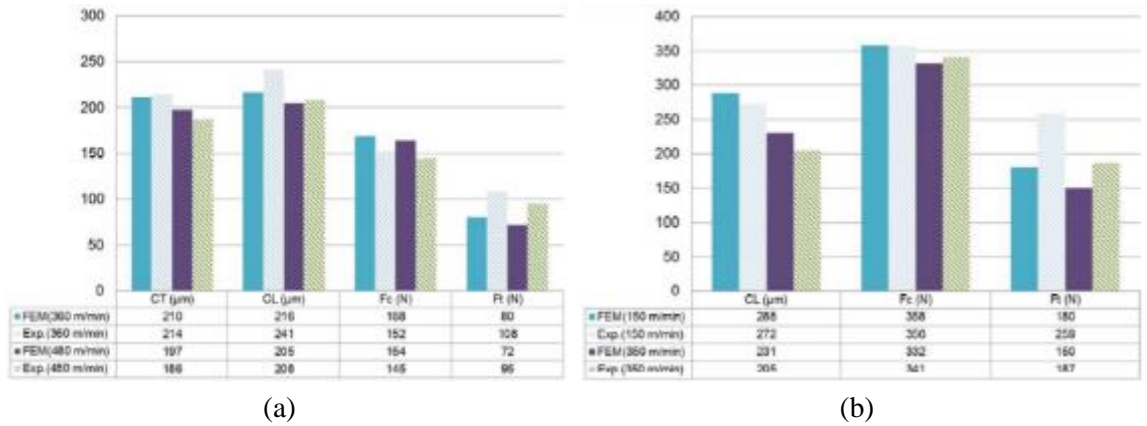


Fig. 6 (a) Cutting forces for AlSi, (b) Cutting forces for GCI (reprinted with permission [19])

Uthayakumar et al. (2009, 2012, and 2017) [20–22] studied the machinability of an AlSi piston reinforced with a Cast Iron insert, shown in Fig. 7, using CBN cutting tools. Process parameters were optimized through a Taguchi approach by evaluating cutting forces, and surface roughness. However, tool wear analysis, and tribofilm formation were not considered in this study, yet are important. In addition, the bimetal cutting in this study was not cyclical due to the workpiece geometry and the process used.



Fig. 7 AlSi-GCI Piston used for bimetal machining study [20]

Correa et al. [23], studied the tool life and wear mechanism for an in-line boring process of a bimetal engine crankshaft bore with cemented carbide tools. Fig. 8 shows the engine block with the highlighted crankshaft bore. During the in-line boring process, the cutting tool undergoes a fully cyclical repeating cutting loads since the journal bearing is composed of half Cast Iron and half steel alloy.

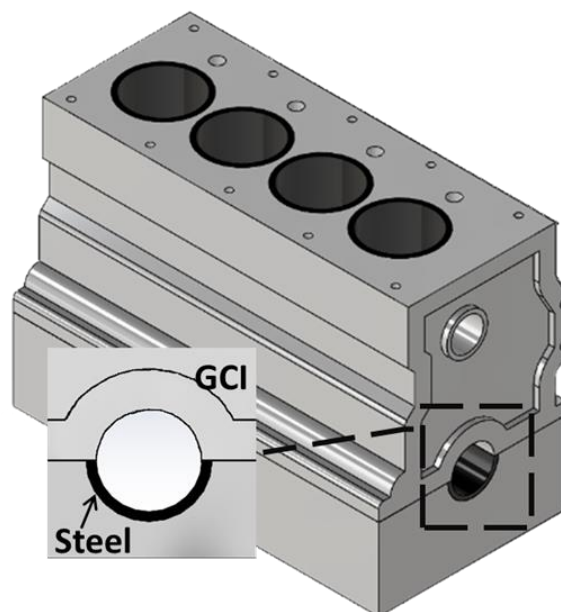


Fig. 8 Cast Iron-Steel bimetal crankshaft bore

The cutting process faces various machining challenges associated with bimetal machining. The first is the fluctuating force on the cutting tool. The fluctuating loading frequency and magnitude would depend on the types of materials and geometry of the bimetallic component. Unlike conventional turning, where the radial force is only 0.3-0.5 of the cutting force, the radial force in this case is predominant in finishing processes for depths of cuts that are lower than the tool nose radius [24]. The radial force significantly impacts the dynamic performance of the process and the dimensional accuracy of the produced parts due to cutting tool deflection. Unlike single material turning, in which dimensional accuracy is compensated, dimensional error is inevitable in bimetal machining. This dimensional error is attributed to the variation in cutting force which changes the tool deflection associated with the compliant structure. The compliance is modelled in the case of an in-line boring bar as a simply-supported beam, as shown in Eq. 2.1.

$$\Delta\delta = \frac{\Delta F_r L^3}{48EI} \quad (2.1)$$

where $\Delta\delta$ is the variation in deflection, ΔF_r is the variation in radial force ($F_{r,GCI} - F_{r,AlSi}$), L is the length, E is the Young's modulus, I is the moment of inertia and $F_{r,GCI}$ and $F_{r,AlSi}$ are the radial forces of GCI and AlSi, respectively. Moreover, the severity of this dimensional error is quantified with the proposed radial force ratio Z as shown in Eq. 2.2.

$$Z = \frac{\delta_1}{\delta_2} = \frac{F_{r,1}}{F_{r,2}} \quad (2.2)$$

where 1 and 2 refer to the stronger material and weaker material, respectively. Ideally, for a single material workpiece, Z is equal to one. However, in the case of a bimetal workpiece,

Z is greater than one. Hence, the greater the Z value the more severe the dimensional error will be.

A consequence of the aforementioned machining challenges is productivity losses due to reduced tool life and worsening quality of the produced parts.

However, the literature on machining bimetallic components is limited to a few application-based studies. The currently existing studies fail to account for cyclic fluctuating cutting forces and to identify the dimensional error caused by elevated radial forces in bimetal components, particularly in AlSi-GCI. Although numerical models for machining processes have been developed, they have been limited to single material machining only.

Chapter 3: Experimental Procedures

Introduction

The main objective of this study is to investigate the machinability of a bimetal AlSi-GCI workpiece with a CBN cutting tool. The machinability study presents the results of tool life, tool wear behaviour, adhesion volume, cutting forces and workpiece surface roughness.

3.1 Cutting tool design and material properties

During this study, two tools were used, Tool 1, and Tool 2. They were customized uncoated CBN inserts mounted in a tungsten carbide (WC) frame, as shown in Fig. 9. In addition, the tools shared the specifications and geometry provided in Table 1. However, Tool 1 had an unprepared edge with 5° rake angle, whereas Tool 2 had a prepared edge with a hone, as shown in Fig. 10.

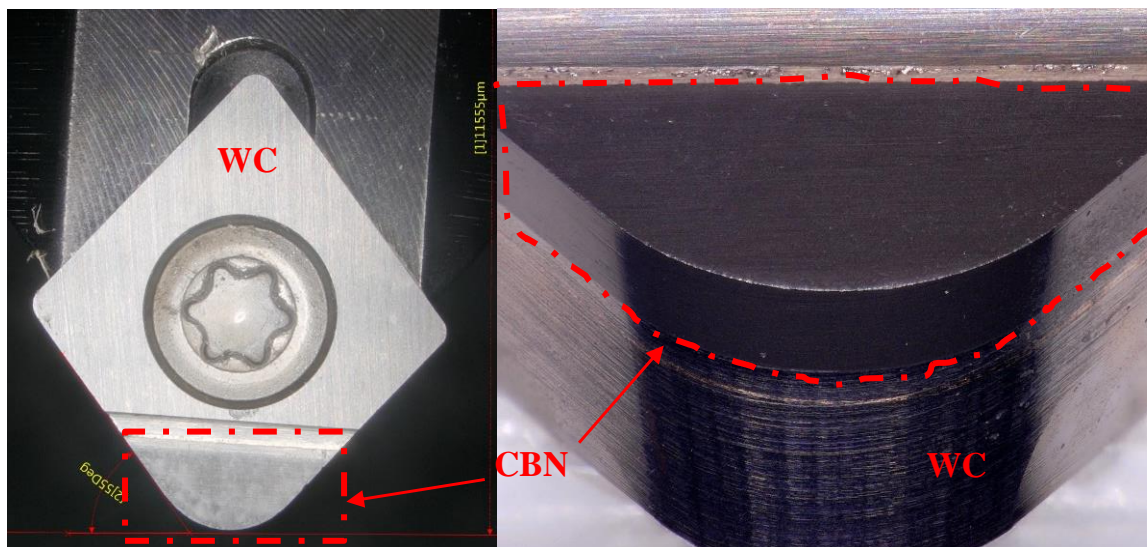


Fig. 9 Overall geometry of the CBN cutting tool

Table 1 Tool specification and geometry

Material	Binder	Content of CBN (vol%)	Particles size	Nose radius	Clearance angle
Uncoated CBN	Ti-alloy	95%	3 μm	1.5 mm	7°

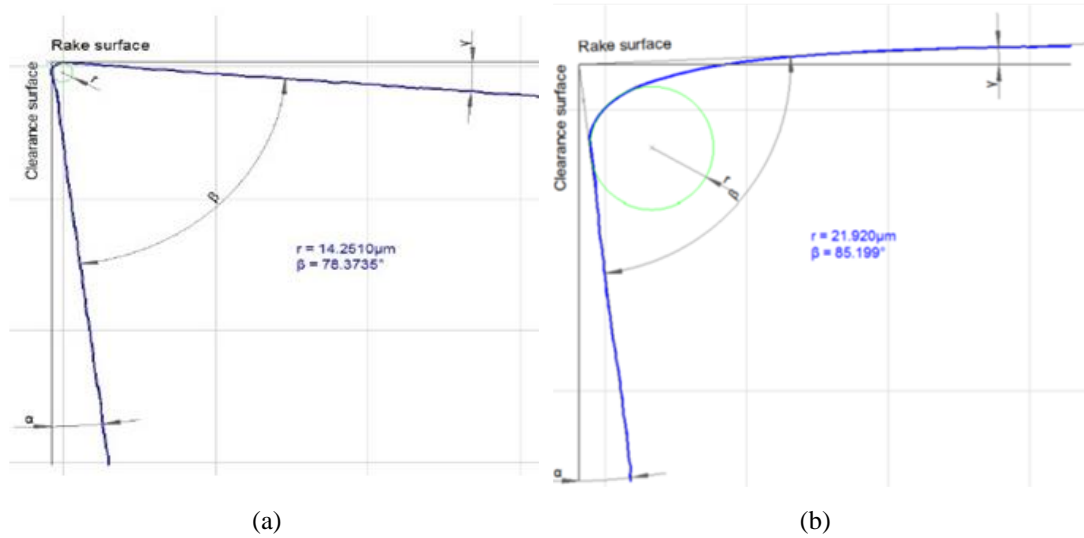


Fig. 10 Tool cutting edge geometry (a) unprepared edge (b) prepared honed edge

3.2 Workpiece material properties & design

3.2.1 Materials of the AlSi-GCI bimetal workpiece:

The workpiece materials were GCI (ASTM A48 class 40), and AlSi (JIS ADC 12). The chemical composition and mechanical properties of the workpiece are given in Table 2, and Table 3, respectively.

Table 2 Chemical composition of AlSi and GCI. [10]

Material	Cu	Mg	Si	Fe	Mn	Ni	Zn	Sn	S	P	Al	C
AlSi	1.5-3.5	0.3	9.6-12.0	1.3	0.3	0.5	1.0	0.3	-	-	Balance	-
GCI	0.36	-	2.25	Balance	0.62	-	-	0.04	0.06	0.11	-	3.02

Table 3 Mechanical properties of AlSi and GCI

Material	Tensile strength	Modulus of elasticity	Hardness
AlSi	310 MPa	71 GPa	75 HB
GCI	167 MPa	125 GPa	207 HB

3.2.2 Design of AlSi-GCI bimetal workpiece:

The few reported studies of bimetal machining in the literature were application limited and dealt with specific components. Consequently, the scope of these studies was very limited. Therefore, designing a bimetallic workpiece that widens the scope of machining studies was found to be essential. To do so, several bimetallic workpiece designs, based on the process type, i.e. reaming, mill boring, lathe boring, and lathe turning, were compared and evaluated according to the following criteria:

- Process rigidity.
- Ease of data collection, i.e. forces, surface roughness, and tool wear.
- Measuring the ability to capture the same conditions on an in-line boring process.

Preparation of test parts and set-up material efficiency:

For boring & reaming, the proposed workpiece design is shown as a CAD drawing in Fig. 11. It is composed of AlSi and GCI alternating, mechanically bolted square bars and equally distributed bores centered at the lines connecting the AlSi and GCI bars.

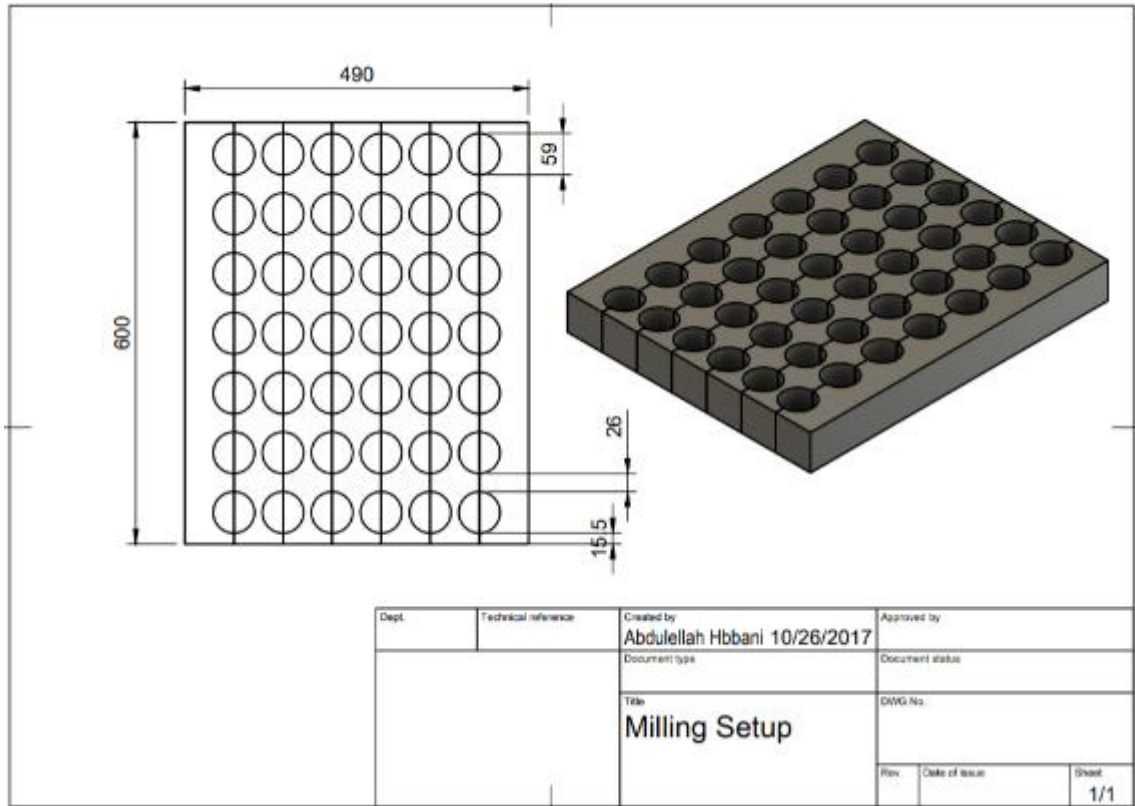


Fig. 11 Reaming & Milling Setup

However, in the turning process, the workpiece is made of AlSi and GCI square bars bolted together and machined into a circular bar, as shown in Fig. 12.

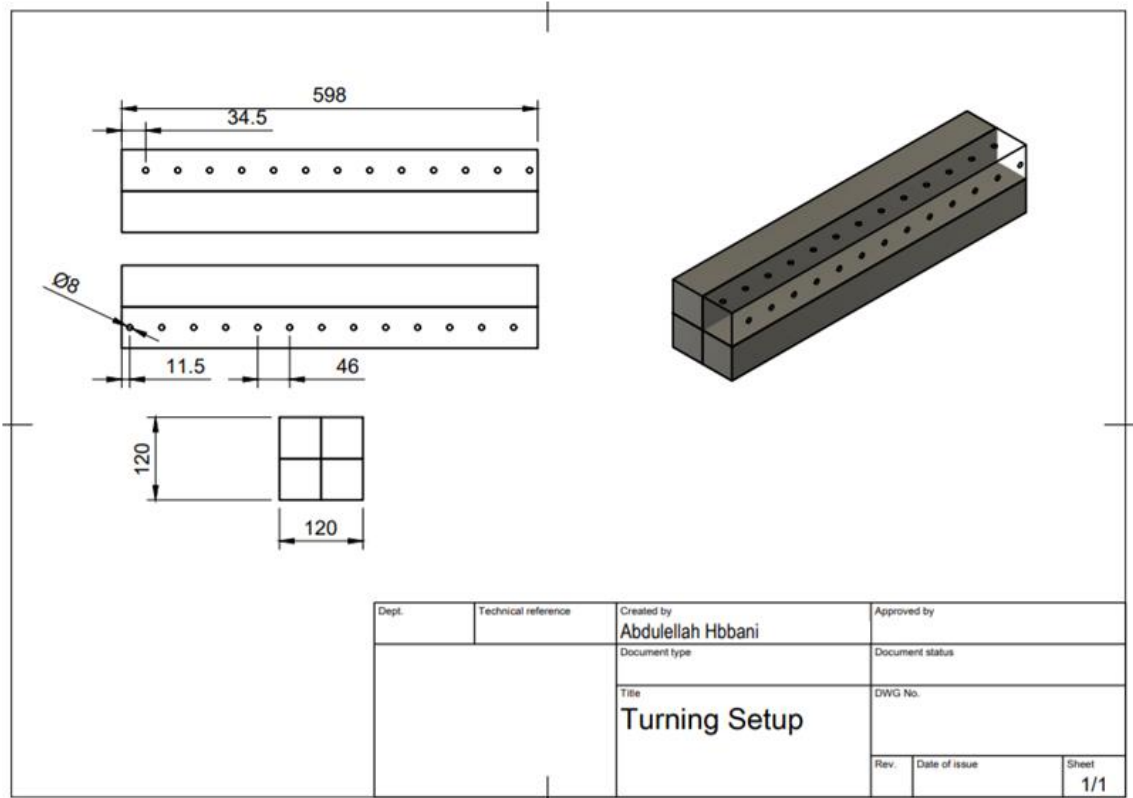


Fig. 12 Proposed turning setup

The final setup used was selected based on the efficiency of material usage, which is determined by calculating the number of crankshaft bores (59 mm in diameter, and 29 mm in width) that any of the two proposed setups can produce, and comparing it to the stock material which was in the form of square rods described in **Error! Reference source not found.**

Table 4 Comparison of material efficiency of different Setups

		Reaming & Milling Setup		Turning setup	
		Aluminum	Cast Iron	Aluminum	Cast Iron
# of used square rods		3	2	2	2
Cross-section of Square rods	Length, mm	70	70	60	60
	Width, mm	70	70	60	60
	Height, mm	430	430	598	598
	Volume, cm ³	6321	4214	4305.6	4305.6

Equivalent Number of bores	48	52
-----------------------------------	-----------	-----------

The above table shows that compared to the turning setup, the reaming and milling setups consume more material to produce the same number of bores. In addition, unlike the turning setup, an additional drilling process is needed to produce the bores on the workpiece in the reaming and milling setups, which would add to the wasted material and extra preparation time and cost.

Process rigidity:

The rigidity of the process is of great importance for testing the process accuracy. For comparison purposes, the machine tools would be taken as rigid structures and only the cutting tool would be compared. Considering the tool as a cantilever beam, its stiffness is represented by Eq.3.1.

$$k = \frac{3EI}{L^3} \tag{3.1}$$

Where:

E= Young’s modulus.

I= Moment of inertia of the cantilever beam.

L= Cantilever beam length.

In this relation, the most important metric is tool length (L). In boring & reaming, the tool length is considerably higher than that in turning. However, unlike boring, reaming is more rigid, since the cutting edges are even in number and thus the forces are balanced.

Ease of data collection, i.e. forces, surface roughness and tool wear:

For AlSi-GCI bimetal machining, forces, tool wear, and surface roughness would be collected during the study. For boring & reaming, and turning processes, milling, and

turning machines are used, respectively. For a milling machine, force sensors are in the form of platforms (except of very limited designs that are attached to the spindle), on which the workpiece is fixed. They are usually less convenient to set up for a milling machine than for lathes, where they can be simply attached to the tool holder. Hence, the sensor is independent of the workpiece and therefore much more convenient in terms of implementation and data collection.

Capability of the process to simulate in-line boring:

In-line boring is performed with a single cutting tool in continuous engagement with the workpiece. Boring with a milling machine could be performed in the same way. In addition, turning an external diameter instead of boring is slightly different, since the cut geometry with respect to the tool is altered. However, reaming would be significantly different as it is an intermittent cutting process where tool cooling is greatly enhanced.

Implementation of Pugh’s decision matrix [25], as shown in Table 5, compared the aforementioned experimental processes based on design criteria to select the best workpiece design for the machinability studies.

Table 5 Comparison of experimental setup criteria

Criteria	Milling Boring Process	Milling Reaming Process	Turning Process
Preparation	D	0	-
Material Efficiency	A	0	+
Process Rigidity	T	+	++
Data Collection	U	0	+
In-line Simulation	M	--	-

Total	£	-1	+3
--------------	----------	-----------	-----------

Hence, the selected workpiece design for the bimetal machinability studies was chosen to be the circular bar with the turning setup.

3.2.3 Manufacturing of AlSi-GCI bimetal workpiece:

To manufacture the bimetal workpiece, the square bars with details and dimensions shown in Fig. 12 were first produced and then mechanically bolted together to form a larger square bar. The larger square bar was then machined into a circular bar.

Since the workpiece was made from two different materials with significantly different densities (2650 Kg/m³, and 7150 Kg/m³, for AlSi and GCI, respectively), balancing issues were inevitable. Therefore, the proposed setup consisted of four bars symmetrically distributed about the circle origin, as shown in Fig. 13, to ensure minimal vibration.



Fig. 13 Manufactured AlSi-GCI bimetal workpiece a) Front view (b) Side view

In addition, as the workpiece is rotated at high speeds, centrifugal forces, that tend to separate the bars, are very critical. Therefore, centrifugal force analysis was carried out to insure proper selection of bolts. Centrifugal was calculated using Eq.3.2.

$$F = \frac{mV^2}{r} \quad (3.2)$$

where:

F = equivalent centrifugal force.

m = mass of one bar.

v = speed of the bar at its center of mass.

r = radius at the centre of mass.

The centrifugal forces (for a defined section) for AlSi₁₀Mg, and GCI were calculated to be 6849 N and 18479 N, respectively.

Since the defined section was supported by two ASTM A574 M8 bolts with a strength of 1172 MPa (property sheet is in the appendix), the strength values were (assuming loads are pure shear):

$$\tau = \frac{F}{A} = \frac{13067}{(\pi * 8^2)/4} = 260 \text{ MPa}$$

Given the bolt strength, the corresponding safety factor was:

$$n = \frac{1172}{260} = 4.51$$

3.3 Experimental setup & Machining conditions

Fig. 14 shows the experimental setup used to perform turning tests on a BOEHRINGER VDF 180 Cm turning center. The machining tests were performed under a dry condition, at a feed rate of 0.062 mm/rev, depth of cut of 0.05 mm and cutting speed of 630 m/min.

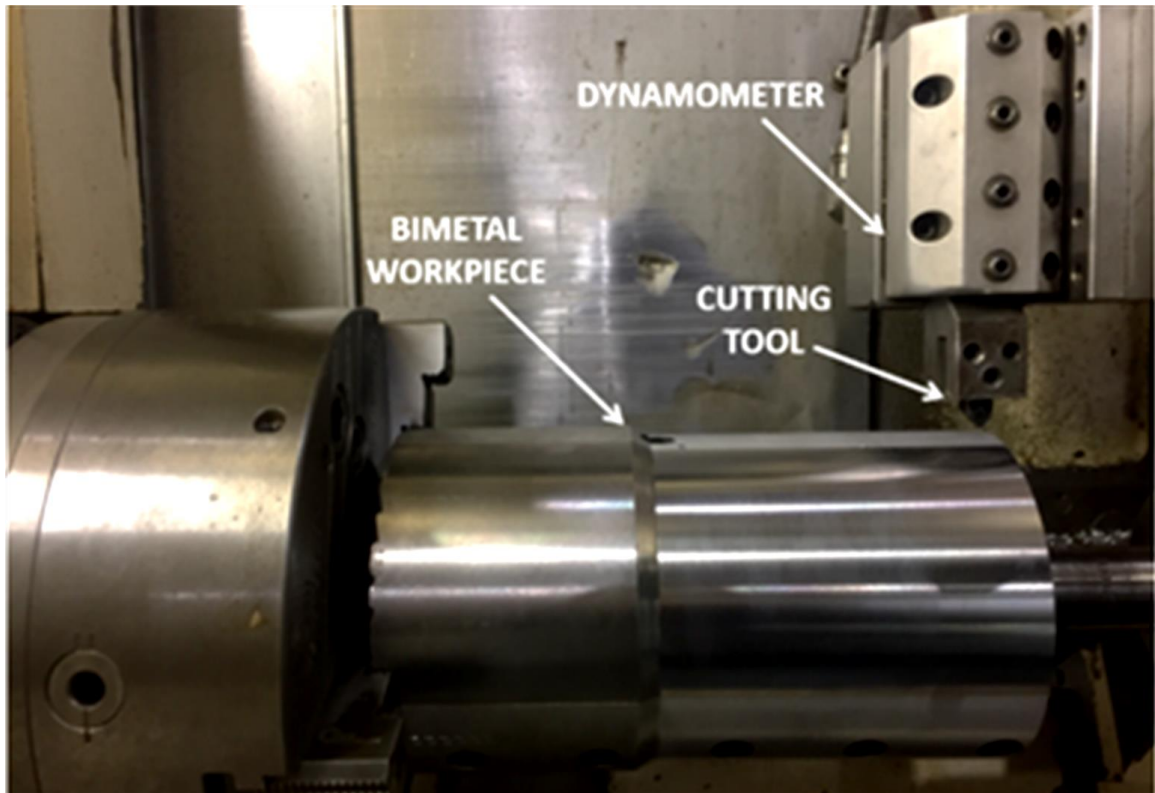


Fig. 14 Machining setup

3.4 Force measurement

Cutting forces were continuously captured throughout the entire turning tests and reported in 8.0 – 10.0 mm intervals of cutting length. The forces were acquired using a piezo-electric dynamometer (Kistler 9121), shown in Fig. 15(a). In addition, the data acquisition setup consisted of:

- Kistler 5010 charge amplifier.
- Data Acquisition Card (National Instruments).
- Customized LABVIEW program.

Fig. 15(b) shows the force component orientation used during testing. The LabView force data acquisition interface is shown in Fig. 16.

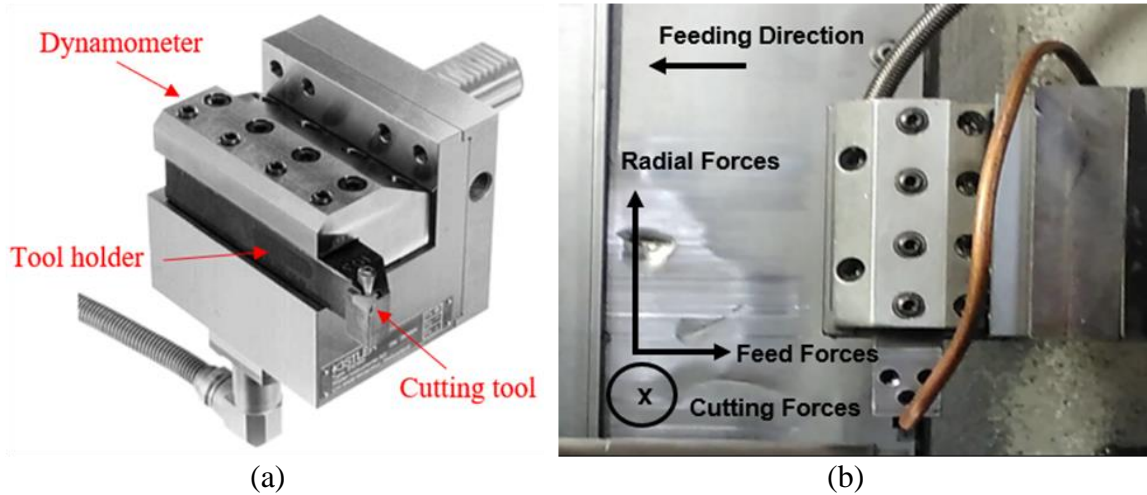


Fig. 15 (a) Kistler 9121 piezo-electric dynamometer (b) Directions of force components

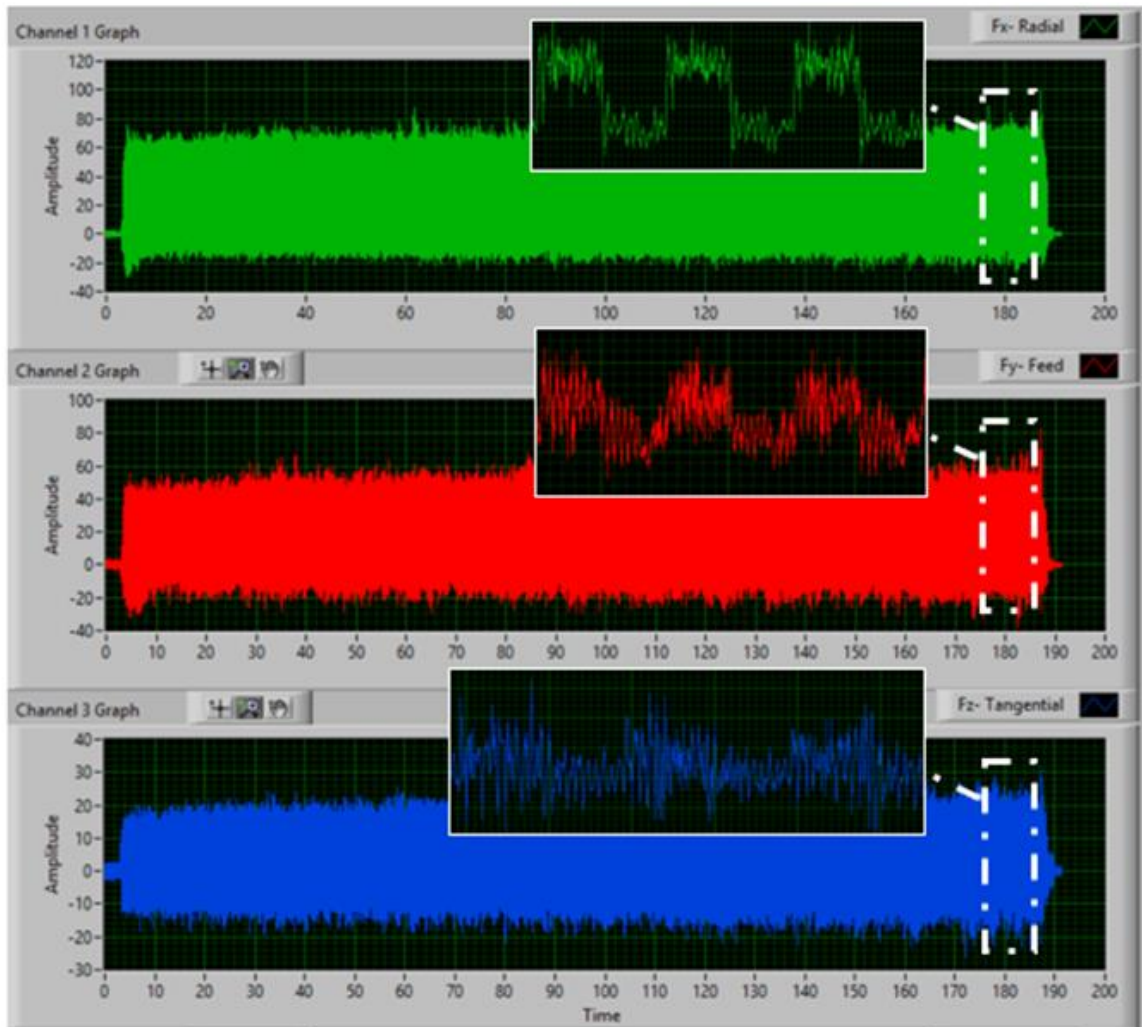


Fig. 16 LabView force acquisition interface.

During testing, the three force components were reported by measuring the average values of GCI and AISi at three different locations within the last third of each pass. Fig. 17 shows the radial force signal at the three measurement locations referred to as 1st, 2nd, and 3rd. A magnification of the latter shows the force ranges of GCI, and AISi, at which the average values were calculated.

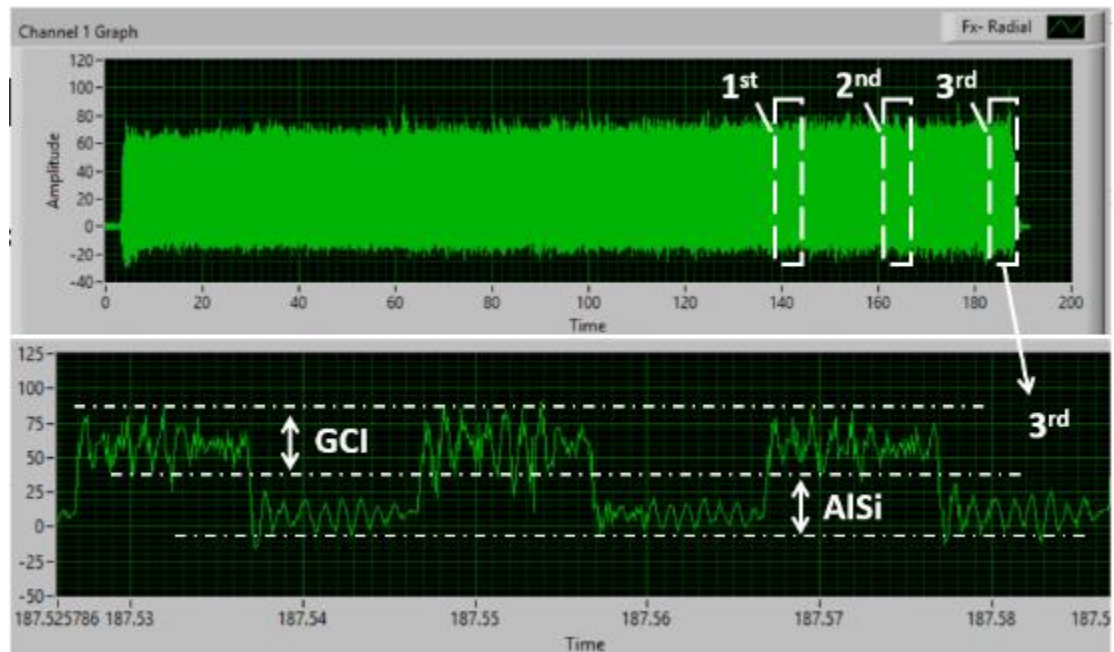


Fig. 17 Force signal sample measurement (Radial component)

3.5 Tool wear & Workpiece surface roughness measurements

3.5.1 Flank wear measurement

A Keyence digital optical microscope (VHX 5000) was used to measure the flank wear of the cutting tools. The flank wear was measured and reported once every five passes, i.e. 8.0 – 10 km of cutting length.

3.5.2 Adhesion measurement

The Alicona InfiniteFocus G5 **Error! Reference source not found.** is a white light interferometry microscope with 60X to 2000X magnification range. In this study, the Alicona was used to perform the volumetric measurements of the cutting tools, which were used to quantify the adhesion accumulated due to machining the AISi-GCI workpiece. The volumetric measurements of Tool Design 1, and Tool Design 2 were analyzed with the Laboratory module of the Alicona system.

3.5.2 Workpiece roughness measurement

Workpiece surface roughness Ra was frequently captured throughout the entire turning test and reported in 8.0 – 10.0 km intervals of cutting length. A Mitutoyo roughness tester sj-201, shown in Fig. 18, was used to measure the workpiece surface roughness.



Fig. 18 Mitutoyo roughness tester sj-201

Chapter 4: Numerical & Statistical procedures

4.1 The Finite Element Numerical Model

A parametric FEM study was conducted through statistically designed experiments, thereby saving time, effort, and material. Specifically, the model was used to measure cutting forces, cutting tool temperature and effective (von Mises) stresses.

4.1.1 Finite element model

Due to the geometrical complexity and numerical difficulties of modelling 3D cutting processes, 2D plain-strain orthogonal cutting models have been widely adopted. However, to ensure plain-strain conditions in the cutting zone, the following assumptions should be taken into consideration [26]:

- The nose of the cutting tool does not engage in the cutting process.
- The cutting edge is wider than the workpiece.
- The undeformed chip thickness (feed) is no less than five times the width of cut.
- The cutting speed direction is perpendicular to the cutting edge.

The turning process meets the above conditions in the current study, except that the nose of the cutting tool was actively engaged in the process. Therefore, the 3D process was reduced to a 2D orthogonal cutting model with some limitations. Fig. 19 shows that the AlSi-GCI experimental workpiece was represented by four alternating pieces of AlSi and GCI for the numerical study. In this figure, lc , f , and V denote the length of cut, feed rate and cutting speed, respectively. The depth of cut in this case was defined to be perpendicular to the view direction.

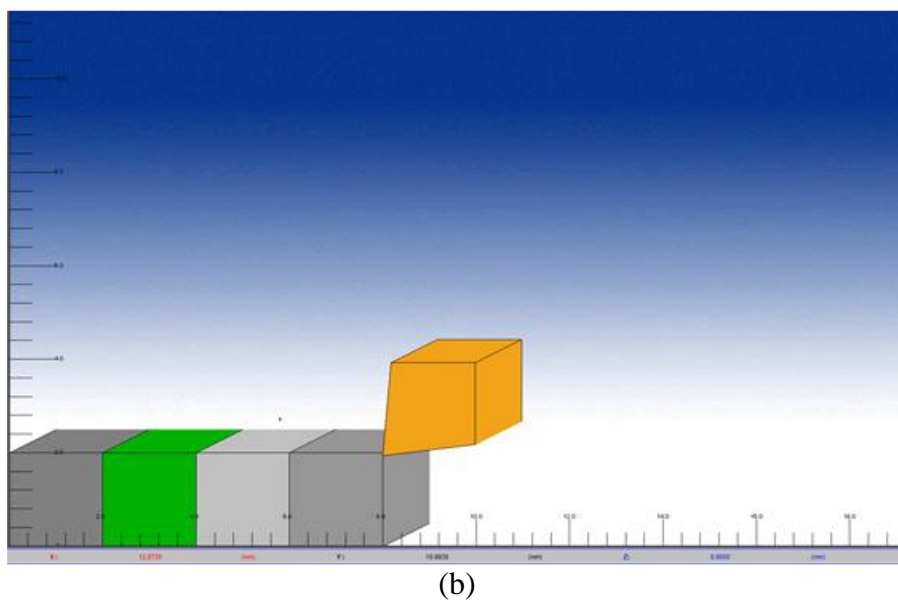
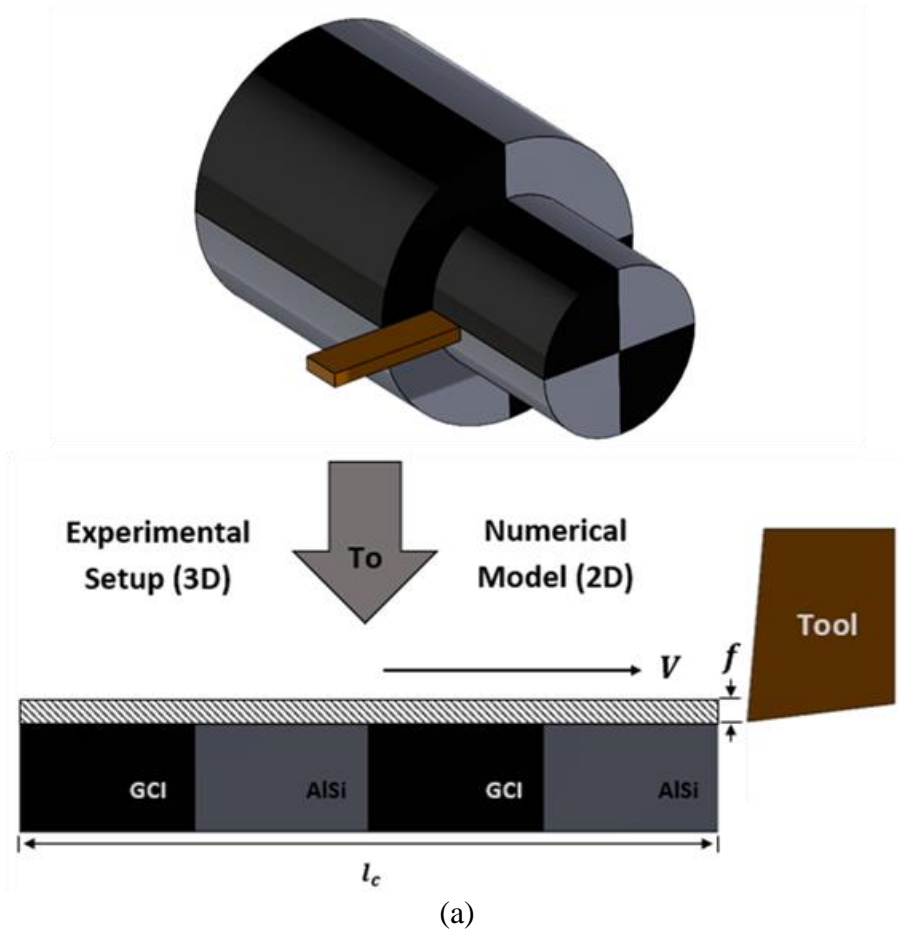


Fig. 19 (a) Idealization of 3D into 2D model. (b) Geometrical model interface in AdvantEdge

Material model

AlSi JIS ADC 12, and GCI ASTM A48 are available as standard material options in AdvantEdge. Material flow stresses with thermal softening were defined by the following Power law model [27]:

$$\sigma_f = \sigma_0 \theta(T) \left(1 + \frac{\varepsilon^p}{\varepsilon_0^p} \right)^{\frac{1}{n}}$$

Also, the strain rate sensitivity of flow stress is given as:

$$\bar{\sigma} = \sigma_f(\varepsilon^p) \left(1 + \frac{\dot{\varepsilon}^p}{\dot{\varepsilon}_0^p} \right)^{\frac{1}{m_1}}, \text{ if } \dot{\varepsilon}^p \leq \dot{\varepsilon}_t$$

$$\bar{\sigma} = \sigma_f(\varepsilon^p) \left(1 + \frac{\dot{\varepsilon}^p}{\dot{\varepsilon}_0^p} \right)^{\frac{1}{m_2}} \left(1 + \frac{\dot{\varepsilon}_t}{\dot{\varepsilon}_0^p} \right)^{\frac{1}{m_1}}, \text{ if } \dot{\varepsilon}^p > \dot{\varepsilon}_t$$

Where:

σ_f = flow stress

σ_0 = initial yield stress at reference temperature T_0

$\theta(T)$ = Thermal softening factor

ε^p = accumulated plastic strain

ε_0^p = reference plastic strain

$\bar{\sigma}$ = effective von Mises stress

$\dot{\varepsilon}_0^p$ = reference plastic strain rate

$\dot{\varepsilon}_t$ = threshold strain rate

m_1 = low strain rate sensitivity component

m_2 = high strain rate sensitivity component

Contact/friction model

AdvantEdge was used to simulate temperature boundary conditions on the rake face, while the remaining faces were characterized with convective heat loss and the isothermal boundary condition. Heat generation during the cutting process in Thirdwave AdvantEdge is due to [28]:

- Plastic deformation on workpiece as described in by Eq. 4.1.
- Friction between the chip and the rake face of the tool according to Eq. 4.2.

Heat generated due to plastic deformation is given by:

$$R = \frac{M f W_p}{\rho} \quad (4.1)$$

Whereas heat generated by friction is:

$$q = F_{fr} V_r M \quad (4.2)$$

The generated frictional heat is distributed to the chip and tool according to Eq. 4.3,

$$Q_{chip} + Q_{tool} = Q_{friction}$$
$$\frac{Q_{chip}}{Q_{tool}} = \frac{\sqrt{k_{chip} \rho_{chip} c_{chip}}}{\sqrt{k_{tool} \rho_{tool} c_{tool}}} \quad (4.3)$$

Where:

q = heat generated due to friction

F_{fr} = friction force

V_r = relative sliding velocity between tool and chip

M = mechanical equivalent of heat ($M=1.0$)

R = heat generated due to plastic deformation

W_p = rate of plastic work

f = is the fraction of plastic work converted into heat

Q_{chip} = heat transferred to the chip

Q_{tool} = heat transferred to the tool

$Q_{friction}$ = total heat generated due to friction

k = conductivity

c = heat capacity

ρ = density

Software and formulation

The FEM model was implemented using AdvantEdge, a commercial software specifically developed for metal cutting applications. AdvantEdge uses a dynamic explicit Lagrangian formulation. Moreover, the model is thermo-mechanically coupled, and a staggered procedure is adopted to combine the thermal and mechanical formulations. First, a mechanical time-step is generated from the current temperature distribution and the generated heat is computed from the plastic work (deformation) and frictional heat.

AdvantEdge uses identical thermal and mechanical model meshes where the calculated heat is transferred to the thermal mesh. The temperatures are then recomputed and transferred to the matching mechanical mesh before being incorporated into the thermal-softening model, which then ends one time-stepping cycle.

4.1.2 FE model calibration

Fig. 20 shows numerical and experimental results of the cutting force for a cutting length of $l_c = 8\text{mm}$ ensuring, temperature steady state conditions are met at the tool rake face.

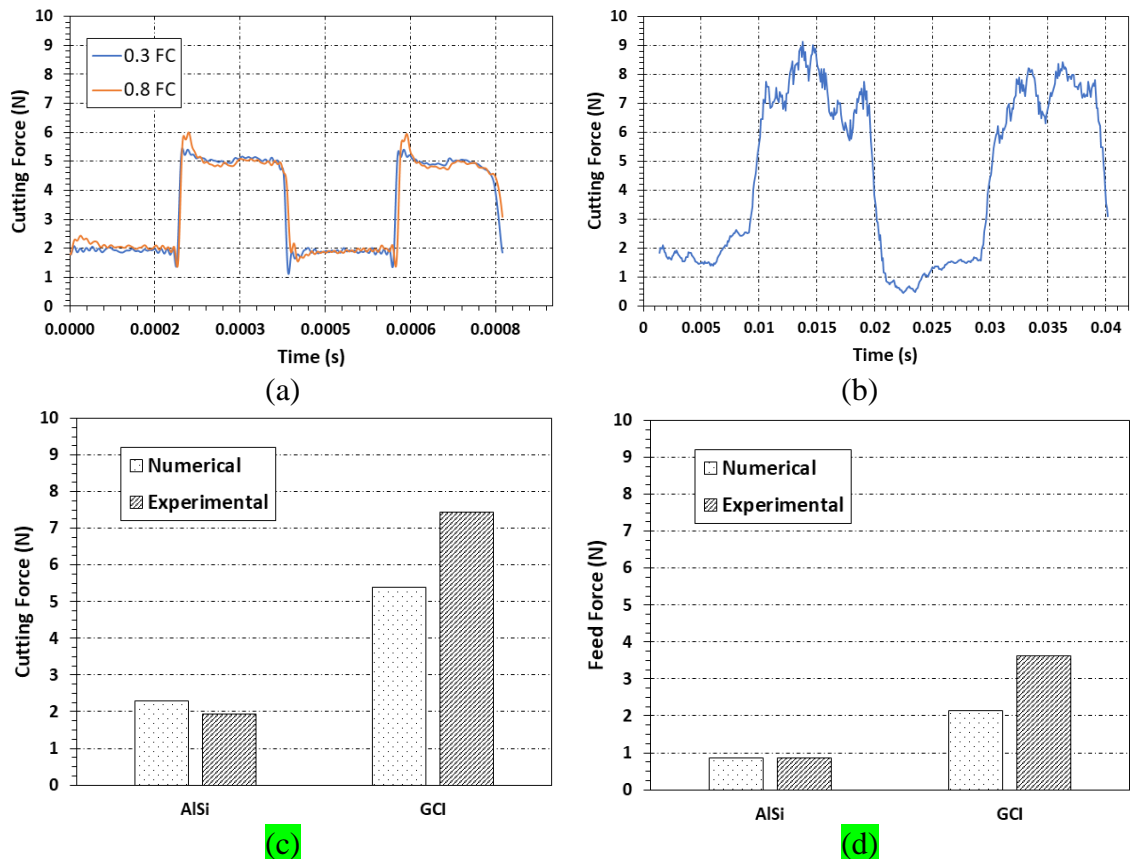


Fig. 20 (a) Variation in numerical force components, (b) Variation in experimental force components, (c) Comparison of average numerical cutting force against experimental, (d) Comparison of average numerical feed force against experimental

In addition, since AdvantEdge allows for one friction coefficient (FC) for the model, the calibration was performed considering two friction coefficients, 0.3 and 0.8, to account any unexpected behaviour. Considering Fig. 20(a) and Fig. 20(b), it was observed that the numerical and experimental results show a similar trend. Fig. 20(a) shows that the effect of FC on the cutting and feed forces was negligible in the numerical simulation. Hence, a FC of 0.8 was set for all the upcoming numerical studies. The numerical prediction of the

average cutting force (Fig. 20(c)) showed a 19% and 27% difference from the experimental measurements for AlSi and GCI, respectively. Similarly, the error in feed force (Fig. 20(d)) for AlSi and GCI was 34%, and 11%.

Chapter 5: Experimental Studies

Results of the experimental work performed on two different CBN tool designs are presented in this chapter.

5.1 Tool Design 1

The objective of this experimental study was to investigate the machinability of bimetal AlSi-GCI workpiece with a CBN cutting tool (an uncoated CBN tool with unprepared edge). The machinability study includes results of tool life, cutting forces, and workpiece surface roughness.

5.1.1 Tool life

The flank face wear pattern of Tool Design 1 under experimental study conditions is shown in Fig. 21. Tool flank wear first rose sharply to 38 μm at 17.5 km cutting length before entering a steady wear zone of 48 μm at a 34.9 km cutting length, which gradually increased to 65 μm at 118.5 km of cut. In the end, the wear increased sharply to 82 μm at 134.7 km.

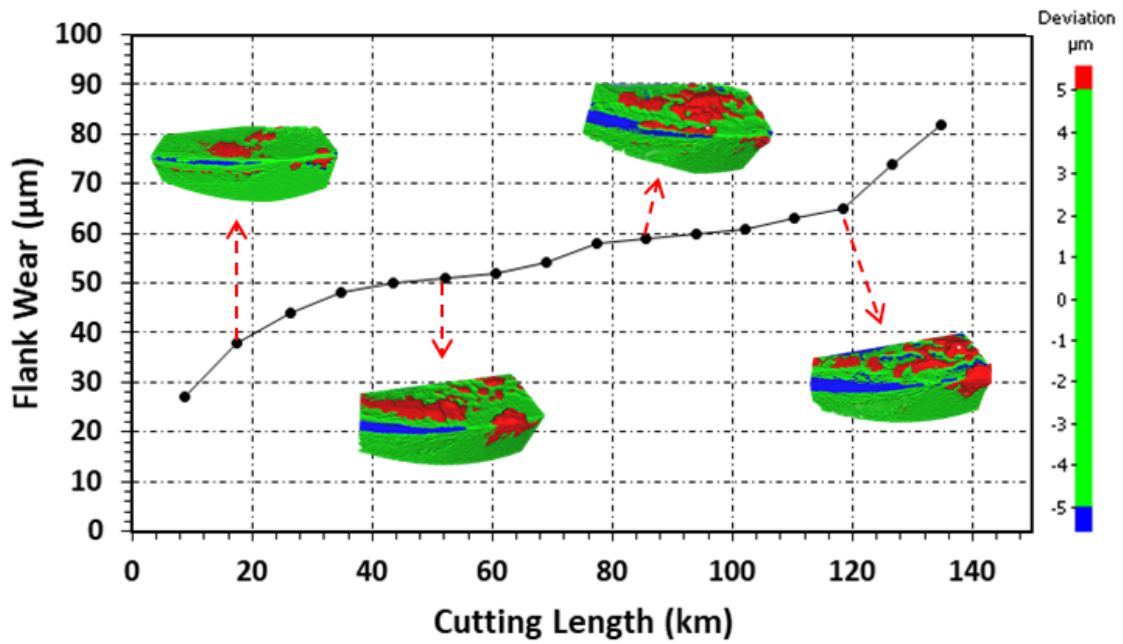


Fig. 21 Flank wear progression with cutting length (Tool Design 1)

In addition to the flank wear, shown in blue, the coloured images in Fig. 21 show workpiece material adhesion in red. The progression of flank wear and the accumulation of adhered workpiece materials are both evident on these volumetric images. The adhered materials will be further discussed as a part of the tool wear behaviour section.

5.1.2 Tool wear behaviour

Optical images are shown in

Table 6 to further assess the progression of tool flank wear and adhesion accumulation on the cutting tool. The orientations in which the images of the flank face cutting side and the adhesion side were taken are illustrated in Fig. 22.

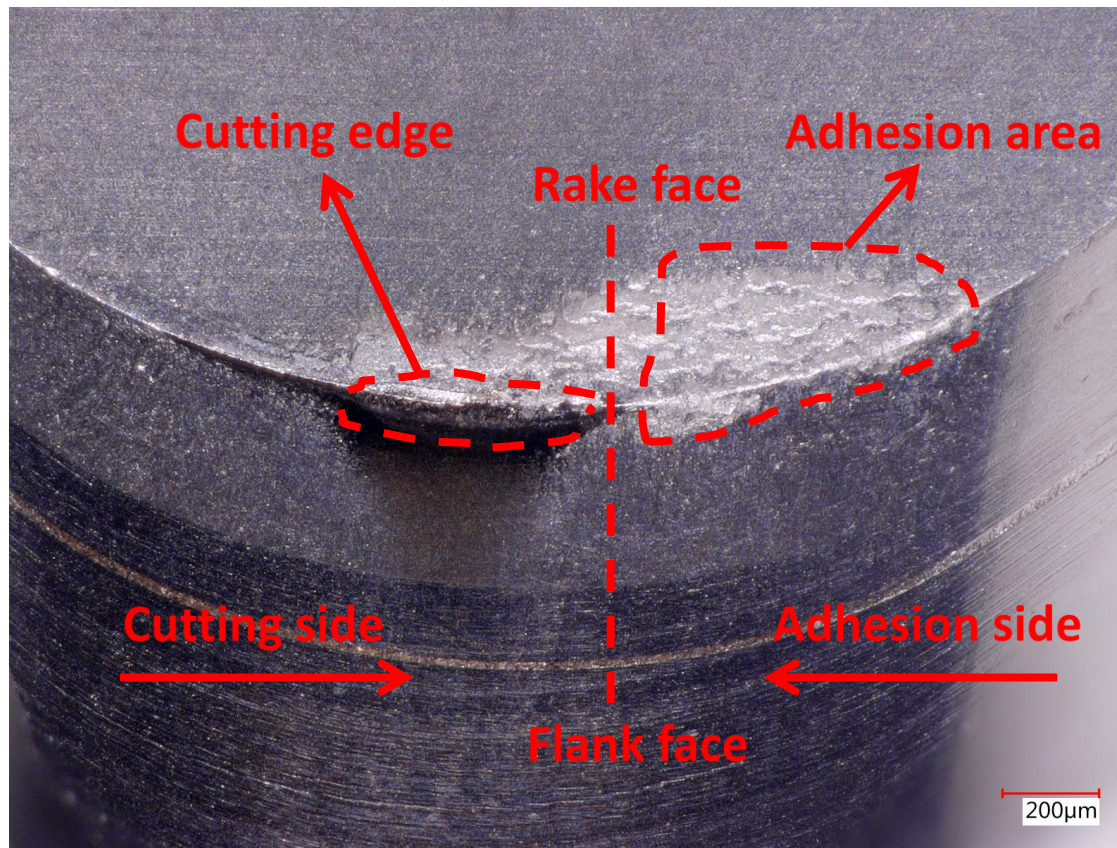
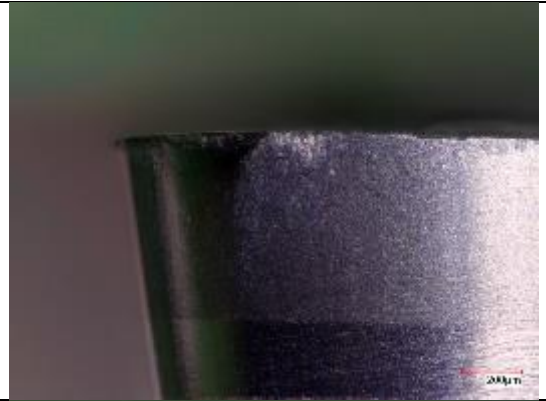
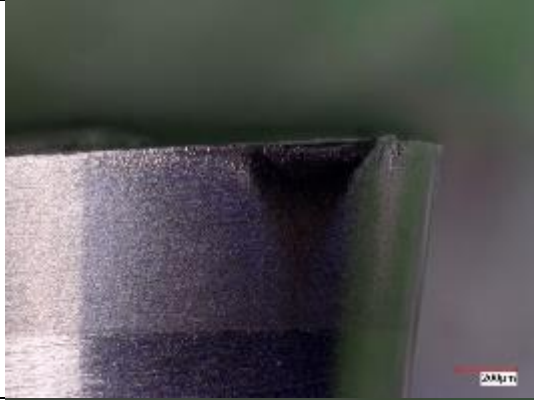
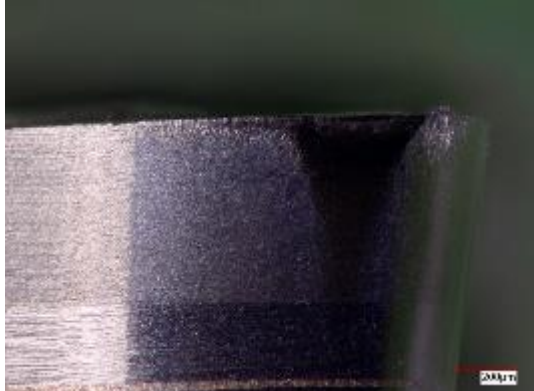
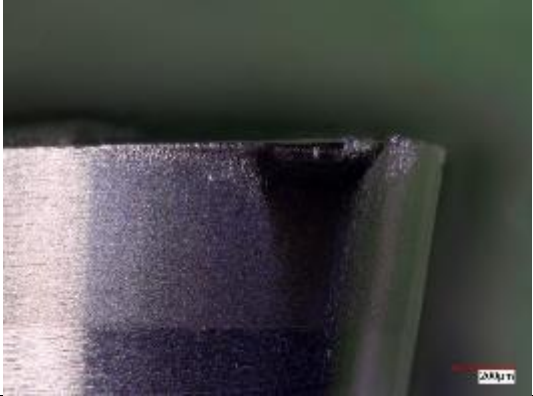
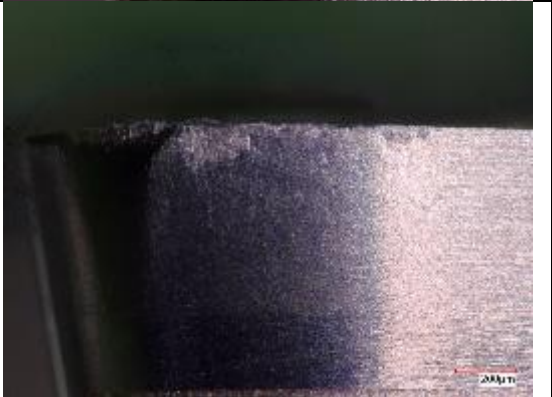
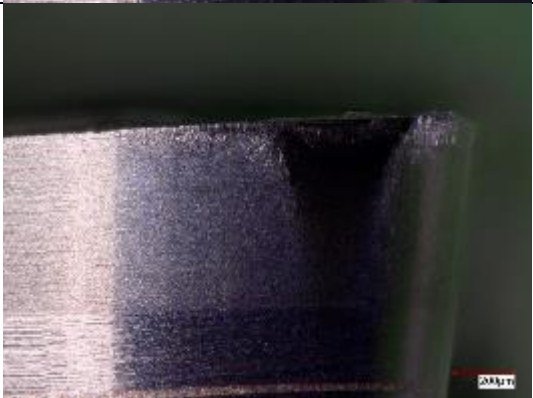
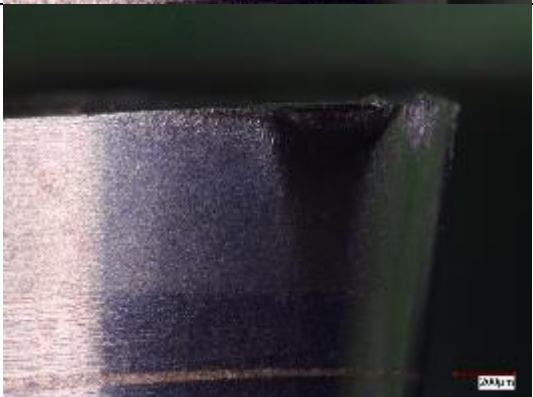


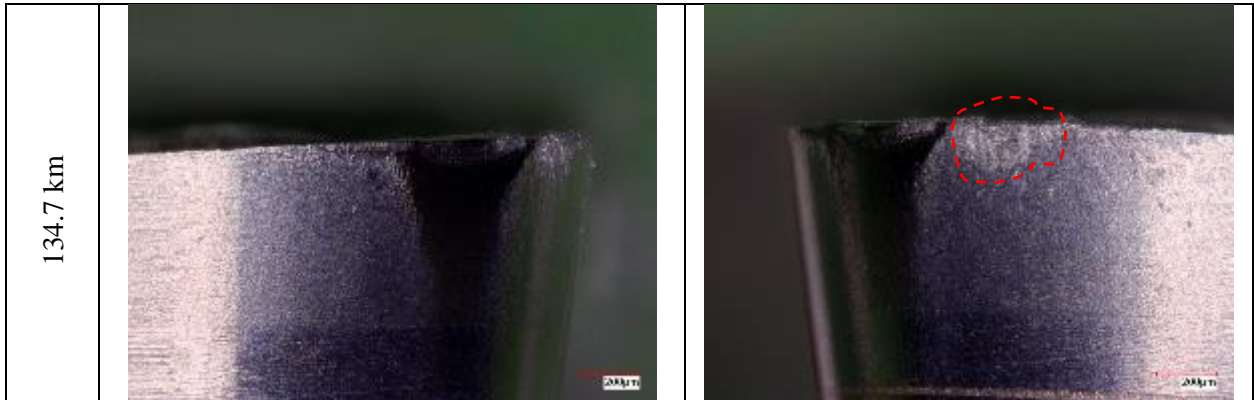
Fig. 22 Cutting zone of the CBN cutting tools

Table 6 shows images of the flank face cutting side along with images of the adhesion side, with the BUE observed and highlighted in red.

Table 6 Optical images of wear and adhesion progression with respect to cutting length (Tool Design 1)

Cutting Length	Flank face (cutting side)	Flank face (adhesion side)
17.5 km		
34.9 km		
52.0 km		

69.0 km		
85.7 km		
102.2 km		
118.5 km		



While turning the AlSi-GCI workpiece, the cutting tool was engaged in cutting two materials with notably different properties: the soft and sticky AlSi and the hard and brittle GCI. Fig. 23, and Fig. 24 show SEM and EDS analysis results of the tool wear at a cutting length of 134.7 km. Fig. 23(a) shows the entire cutting tool with areas of interest such as the cutting edge and the chip evacuation zone. At first, as shown in Fig. 23(b, c), metal transfer, from the workpiece to the cutting tool was considered as a built-up layer (BUL) at both the cutting edge and in the chip evacuation zone. Secondly, as shown in Fig. 23(d), diffusion was evident at the rake face and very close to the cutting edge. Moreover, abrasion marks were observed at the cutting edge along with the accumulated BUL.

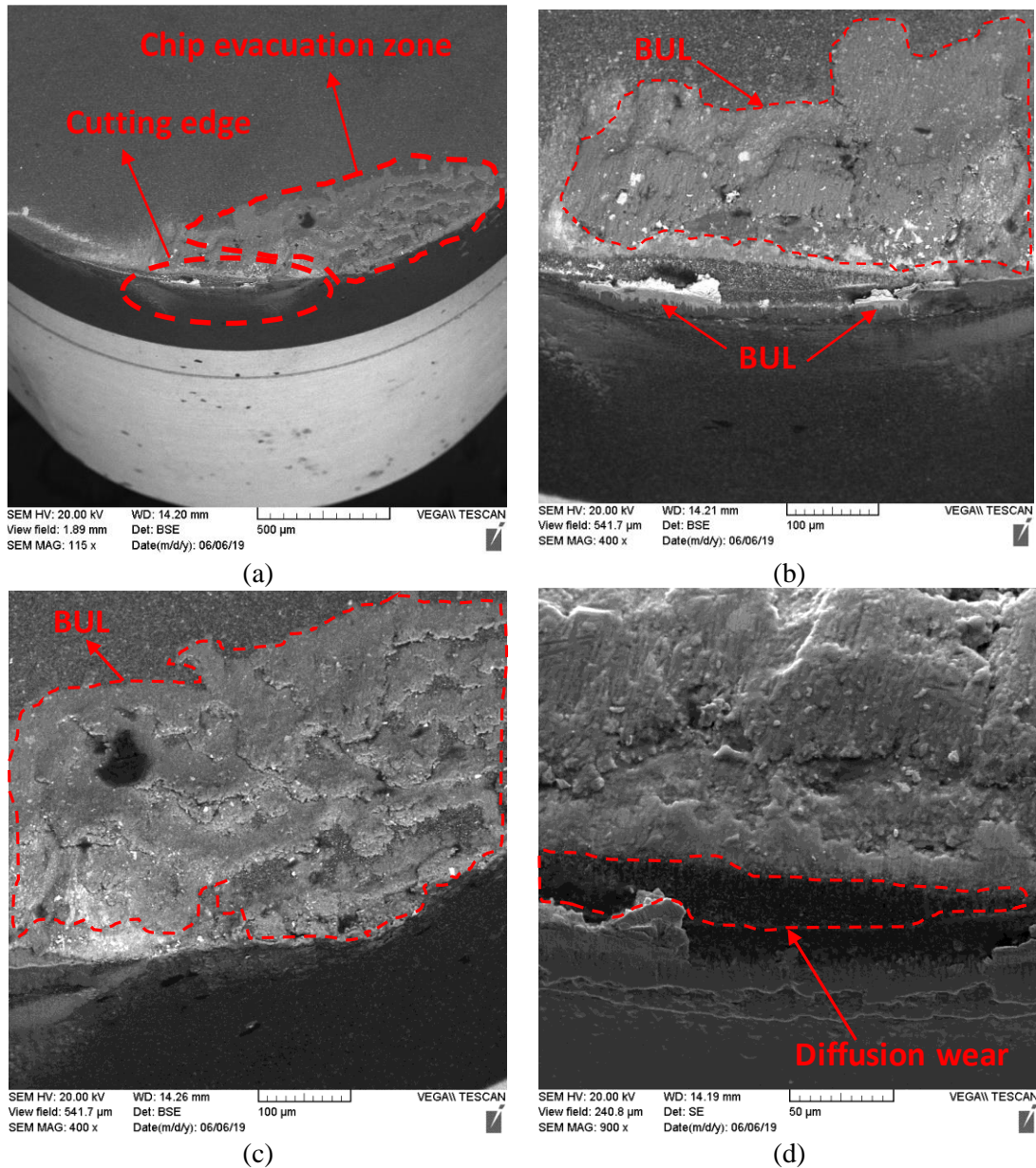


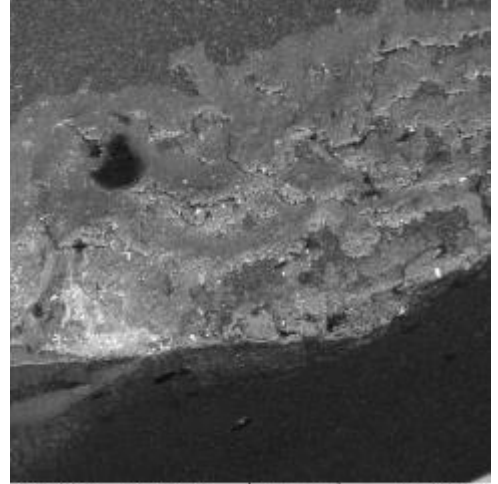
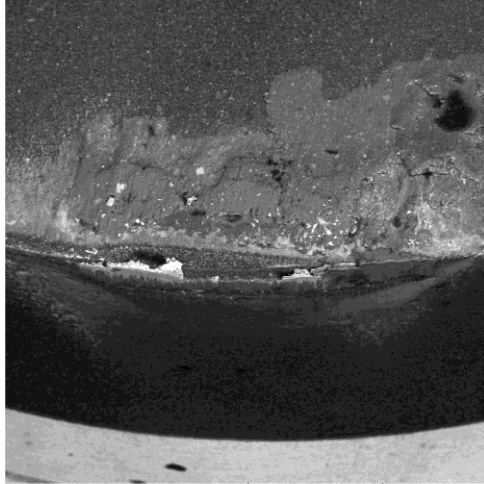
Fig. 23 SEM analysis of the CBN cutting tool

As shown in Fig. 24, the adhered BUL at the cutting edge was found to be composed of aluminum (Al) and iron (Fe), with Al being predominant. Al was abundant at the chip evacuation zone with limited presence of Fe. This is because the brittle GCI chip is much shorter compared to that of the ductile AlSi. Thus, the GCI chip does not extend far enough to accumulate on the chip evacuation zone of the tool as compared to the AlSi chip. When

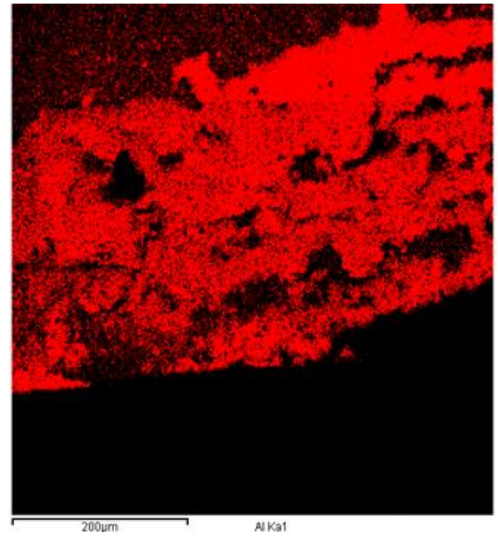
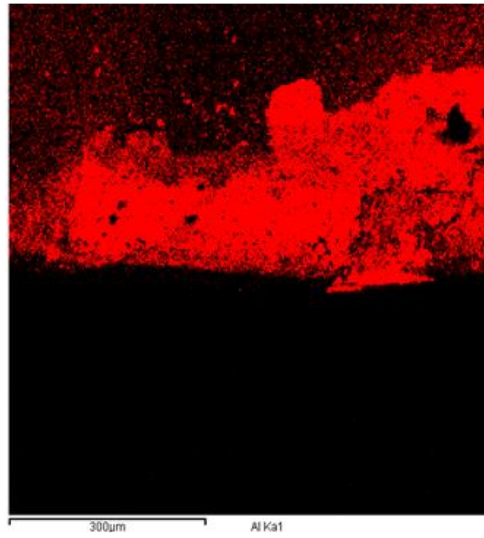
the adhered Fe and Al on the CBN cutting tool were removed by the high cutting stresses, they carried the CBN particles away with them, causing attrition wear. The intensity of attrition was proportional to the hardness of the adhered materials. Hence, attrition was more significant at the cutting edge where more Fe particles were present as compared to the chip evacuation zone further up the tool surface.

As shown in Fig. 24, oxide, and MnS layers were observed at both the cutting edge and the chip evacuation zone. Limited wear progression was evident at areas where oxide and MnS were present. Several studies found that during GCI machining with CBN tools, films, such as oxides and MnS form between the tool and the workpiece, act as protective layers that delay tool wear. Liu et al. [9], showed that a protective oxide layer forms when GCI is machined with CBN tools. In addition, Gastel et al. [7] also found that a protective MnS film forms in this case at speeds higher than 400 m/min.

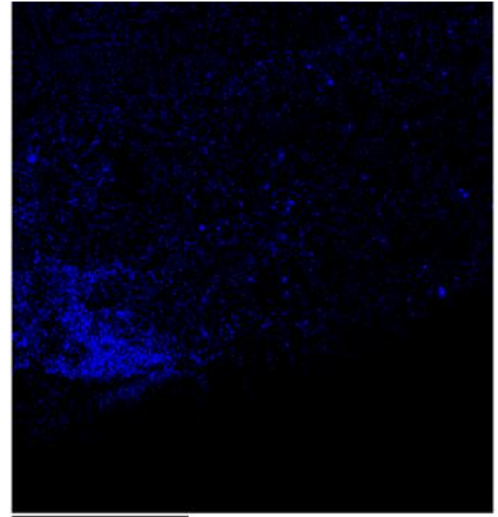
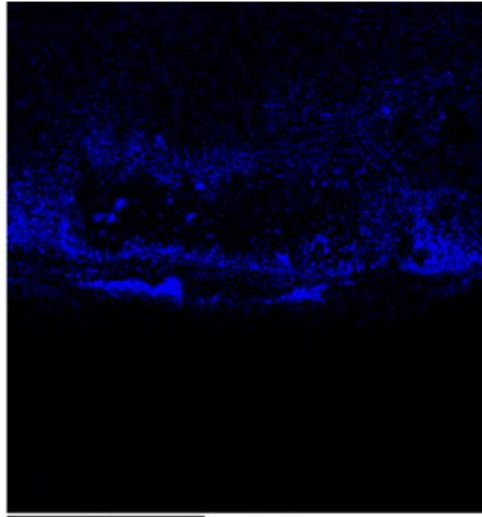
SEM



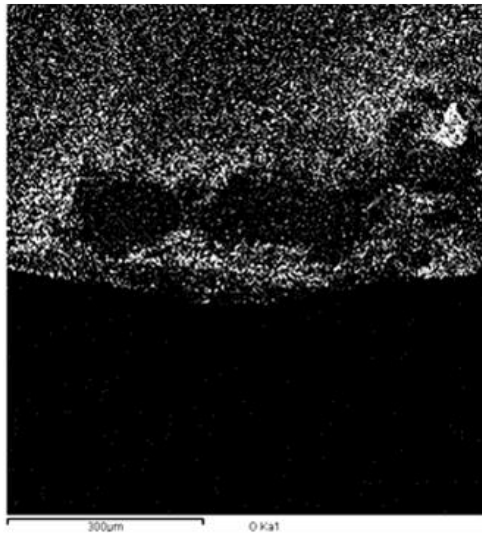
Al



Fe



O



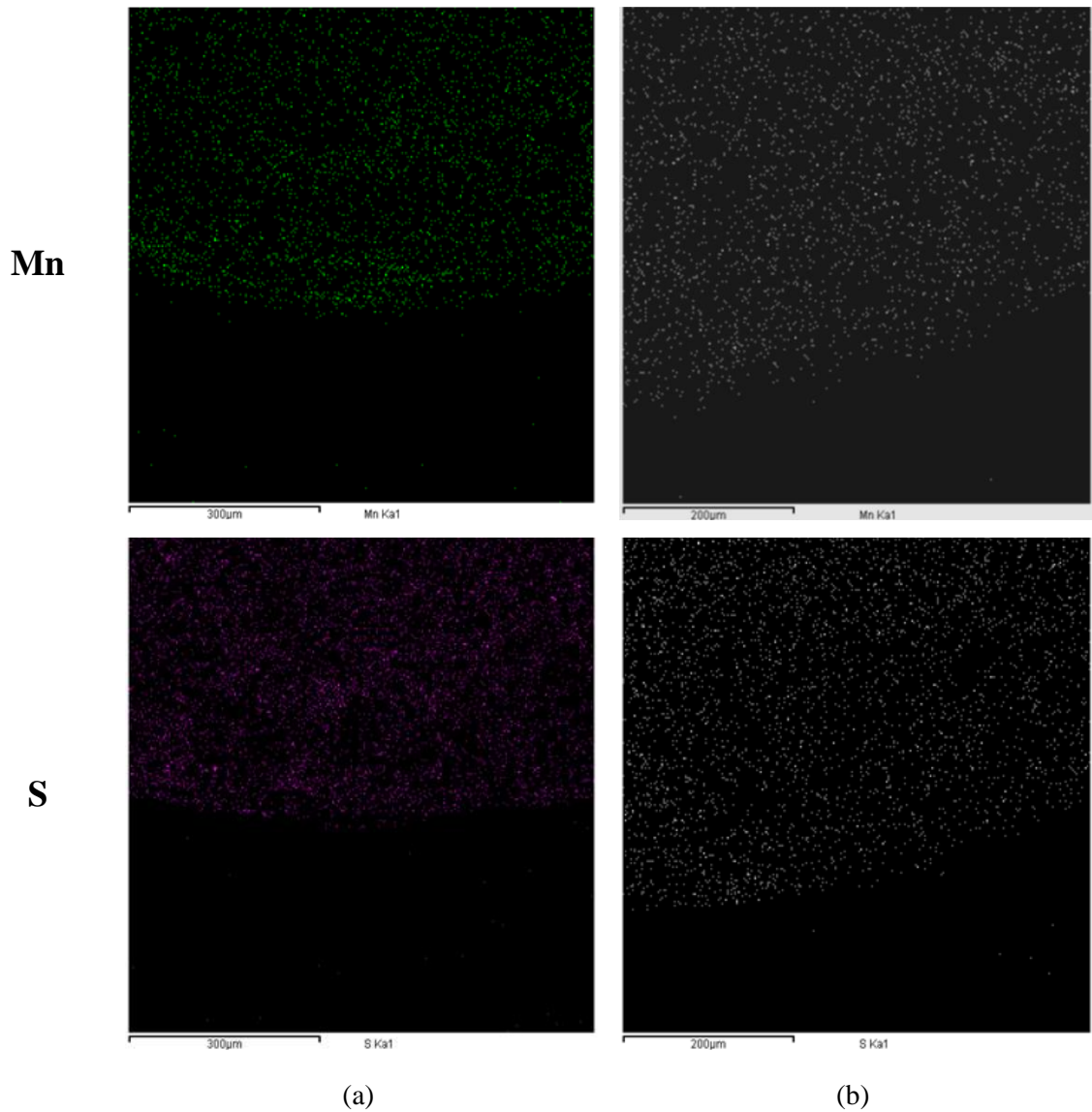


Fig. 24 SEM and EDS analysis of cutting tool (a) cutting edge, (b) Chip evacuation zone

The wear mechanisms of a CBN cutting tool during the turning of a bimetal AlSi-GCI workpiece were observed to be mainly attrition, abrasion, and diffusion.

Aluminum adhesion

To quantify the previously discussed adhesion, a numerical volumetric 3D adhesion measurement is presented in Fig. 25. The adhered layer from the workpiece was mostly present on the rake face, fluctuating between of 0.0002 mm^3 and 0.0013 mm^3 . In addition,

BUE is generated at 52.0 km and 118.5 km, as shown in Fig. 25. The random reductions of adhesion volume were attributed to the fluctuating cutting stresses.

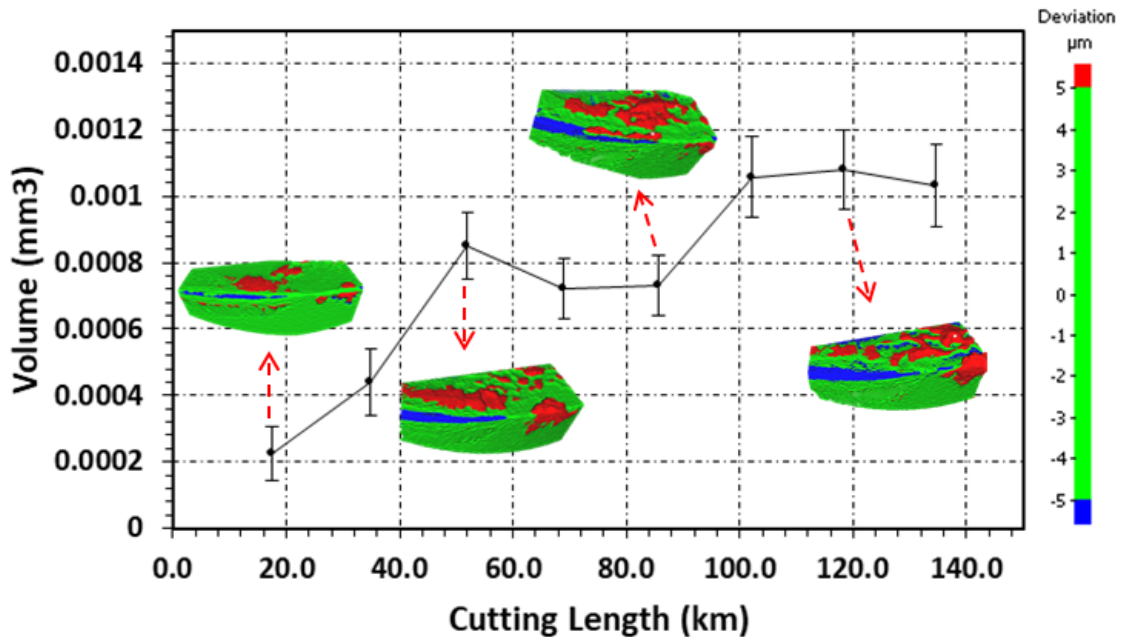


Fig. 25 Accumulation of adhesion on the cutting edge with respect to cutting length.

5.1.3 Cutting Forces:

Fig. 26(a) shows that the cutting force increased for both AISi and GCI until a cutting length of 34.9 km was reached, before becoming stable. However, the rate of increase of the GCI part was greater than that of the AISi section. A similar trend was observed for the feed and radial forces shown in Fig. 26(b) and Fig. 26(c), respectively. Moreover, the radial force component was noted to be the highest, further increasing after 118.5 km. The higher forces of the GCI were caused by its higher hardness as compared to AISi [4]. As shown in Table 3, the hardness of GCI is 64% greater than that of AISi. The predominance of the radial force can be attributed to the combination of a low depth of cut (50 µm) and

a high nose radius (1.45mm), resulting in a small effective cutting edge angle (K_r) defined in Eq 5 [30].

$$K_r = \cos^{-1}\left(\frac{r_c - a_p}{r_c}\right) \quad (5)$$

Where:

a_p = Depth of cut

r_c = Nose radius

The variations in cutting forces, ΔF_f , ΔF_c , and ΔF_r vs. the cutting length shown in Fig. 26(d) were considered in this study. The trend shown was similar to the variation in each individual material section (Al or GCI), increasing until becoming stable at around 34.9 km of cutting length. However, ΔF_r was always greater than ΔF_f and ΔF_c . ΔF_r increased from 19.1 N at 8.8 km to an average steady value of 43.1 N at 34.9 km of cutting length. At the same length of cut, ΔF_f increased from 3.8 N to 8.3 N and ΔF_c increased from 7.5 N, to 19.7 N.

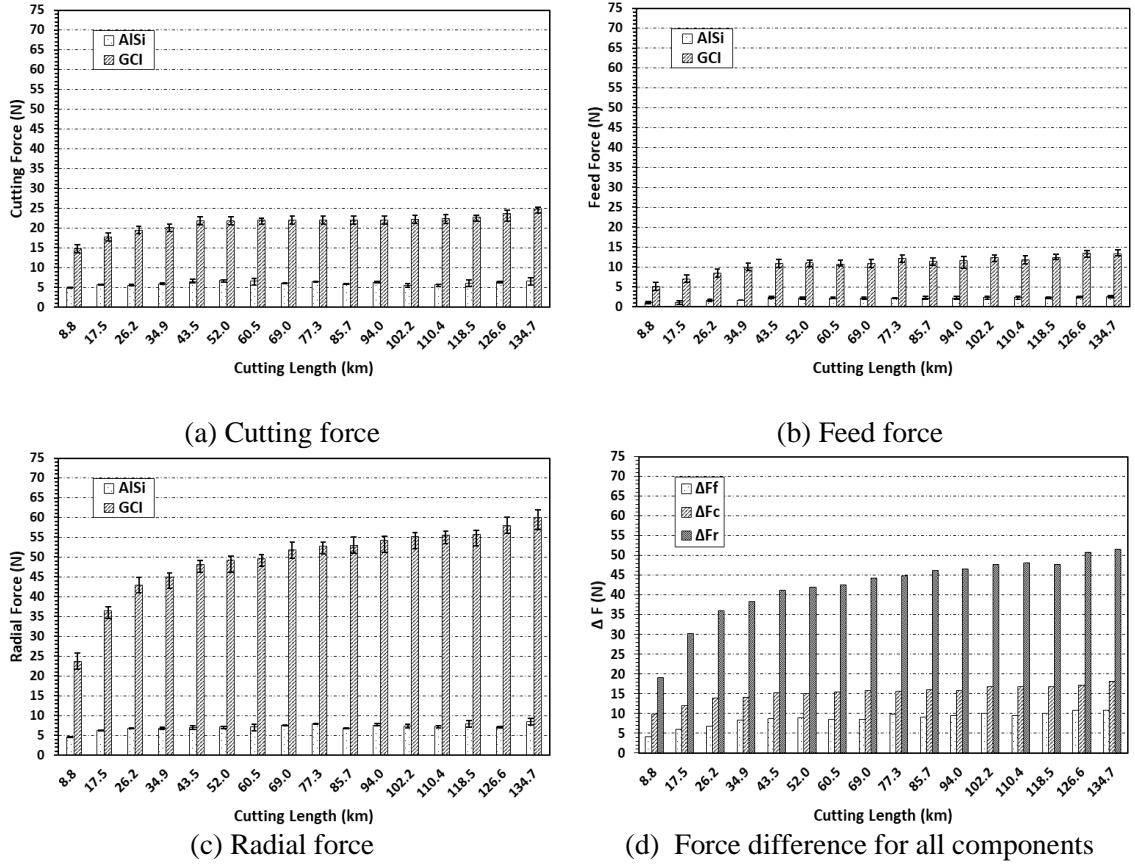


Fig. 26 Variation in force components (a) cutting force, (b) feed force, (c) radial force, and (d) difference in force (Tool Design 1)

Fig. 27 shows the radial force ratio Z (discussed in Chapter 2), with respect to cutting length. It started with a value of 5.1 at 8.8 km and grew to an average steady-state value of 7.0 after 34.9 km.

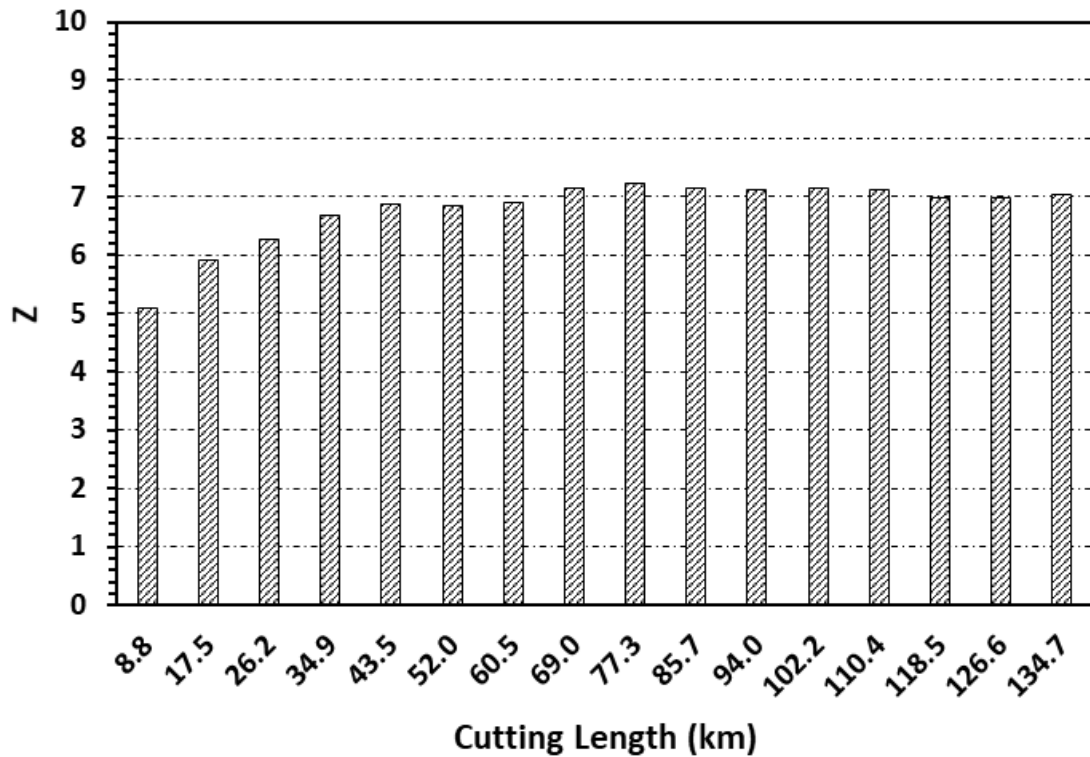


Fig. 27 Progression of Z value with respect to cutting length (Tool Design 1)

Refer to the tool flank wear shown in Fig. 21, in which the cutting tool enters the stable zone of flank wear at a cutting length around 34.9 km. All force components along with the radial force ratio Z show a similar trend, becoming steady at the same cutting length. Therefore, the force increase was attributed to the corresponding increase in friction caused by growing the tool flank wear.

5.1.4 Surface roughness:

Aluminum alloys in general are challenging to machine under dry cutting conditions due to adhesion and BUE formation followed by surface quality deterioration [31]. A study done by Fukui et al. [32], showed significant AlSi surface roughness deterioration after machining with uncoated cemented carbide tools under dry conditions. The surface roughness of the bimetallic workpiece is shown in Fig. 28.

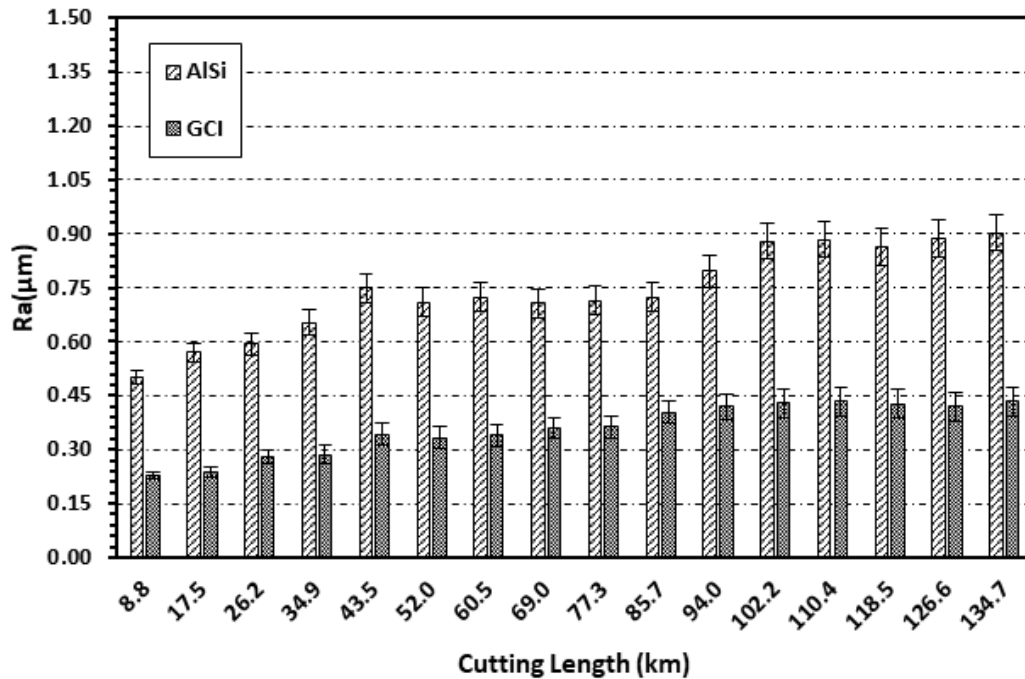


Fig. 28 Variation in surface roughness of machined surface (Tool Design1)

In general, the workpiece surface roughness trend (R_a) of both GCI and AISi, was similar to that of the tool flank wear, with AISi having a higher magnitude. However, surface roughness was also affected by the adhesion of AISi on the cutting edge. For example, the surface roughness drops after 34.9 km of cut in both GCI and AISi, at which point the adhered layer on the cutting tool also was observed to reduce in size.

The significantly higher roughness values of AISi can be mostly attributed to the BUE that forms on the cutting tool. The presence of an unstable BUE on the cutting edge causes the cutting surface depth to vary, which significantly contributes to the degree of surface roughness[4]. However, since the BUE was mostly composed of AISi, it tended to break off more easily due to GCI's much higher hardness. In addition, GCI does not form a BUE since it is a brittle material.

5.2 Tool Design 2

The same machinability study conducted on Tool Design 1 was carried out on Tool Design 2 to understand the effect of tool geometry on the machining performance.

5.2.1 Tool life

The wear pattern of the flank face of Tool 2 under the experimental study conditions is shown in Fig. 29. At first, tool flank wear grew sharply to $48\ \mu\text{m}$ at $18.4\ \text{km}$ of cutting length, entering the steady wear zone of $56\ \mu\text{m}$ at $36.8\ \text{km}$ of cutting length, which then gradually increased to $68\ \mu\text{m}$ at $118.3\ \text{km}$. Finally, the wear rose sharply to $84\ \mu\text{m}$ at $145\ \text{km}$.

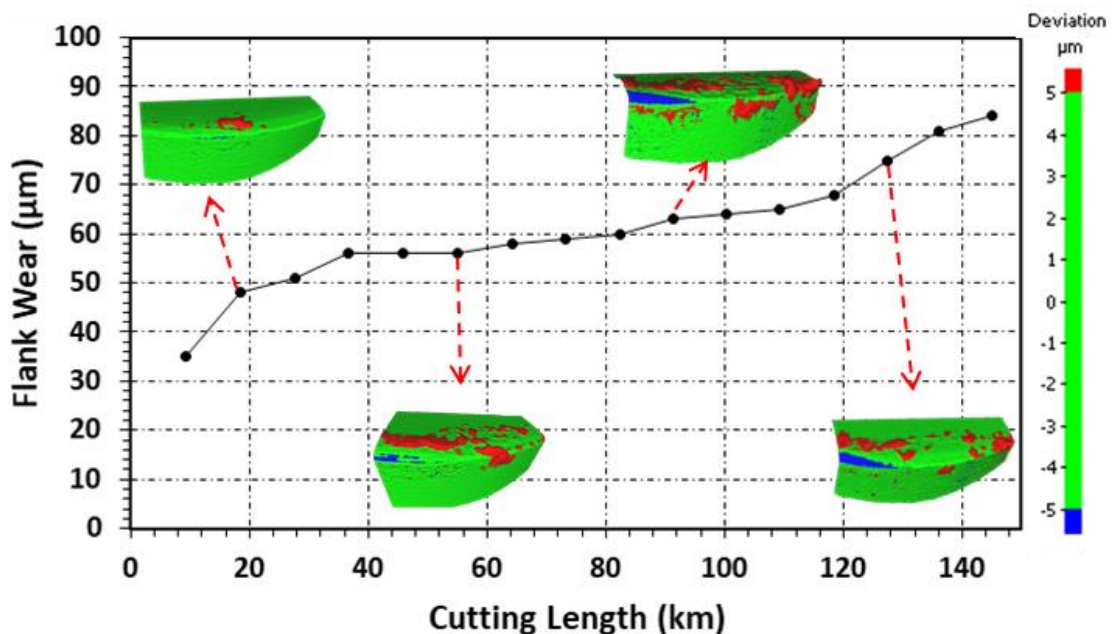
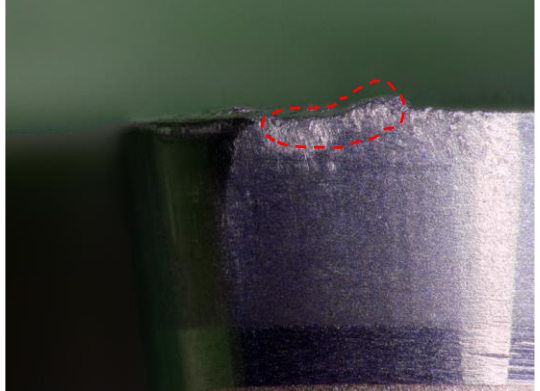
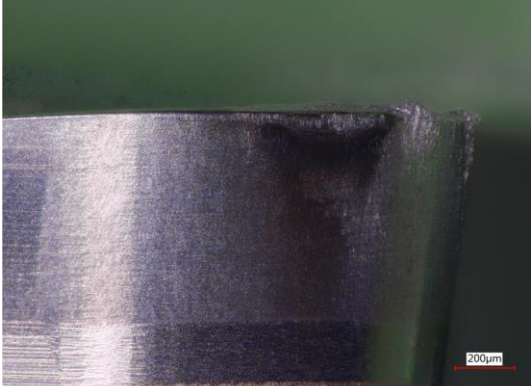
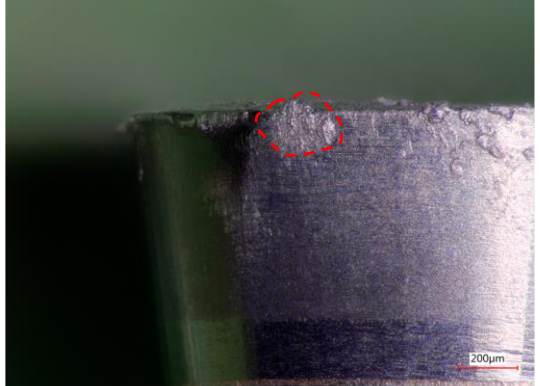


Fig. 29 Flank wear progression with cutting length (Tool Design 2)

5.2.2 Tool Wear behaviour

Table 7 displays the optical images comparing the tool wear progression over time. Moreover, along with the flank wear shown on the cutting side images, adhesion formation is shown on the adhesion side images, with the BUE highlighted in red.

Table 7 Optical images of wear and adhesion progression with respect to cutting length (Tool Design 2)

Cutting Length	Flank face (cutting side)	Flank face (adhesion side)
18.4 km		
36.8 km		
55.0 km		

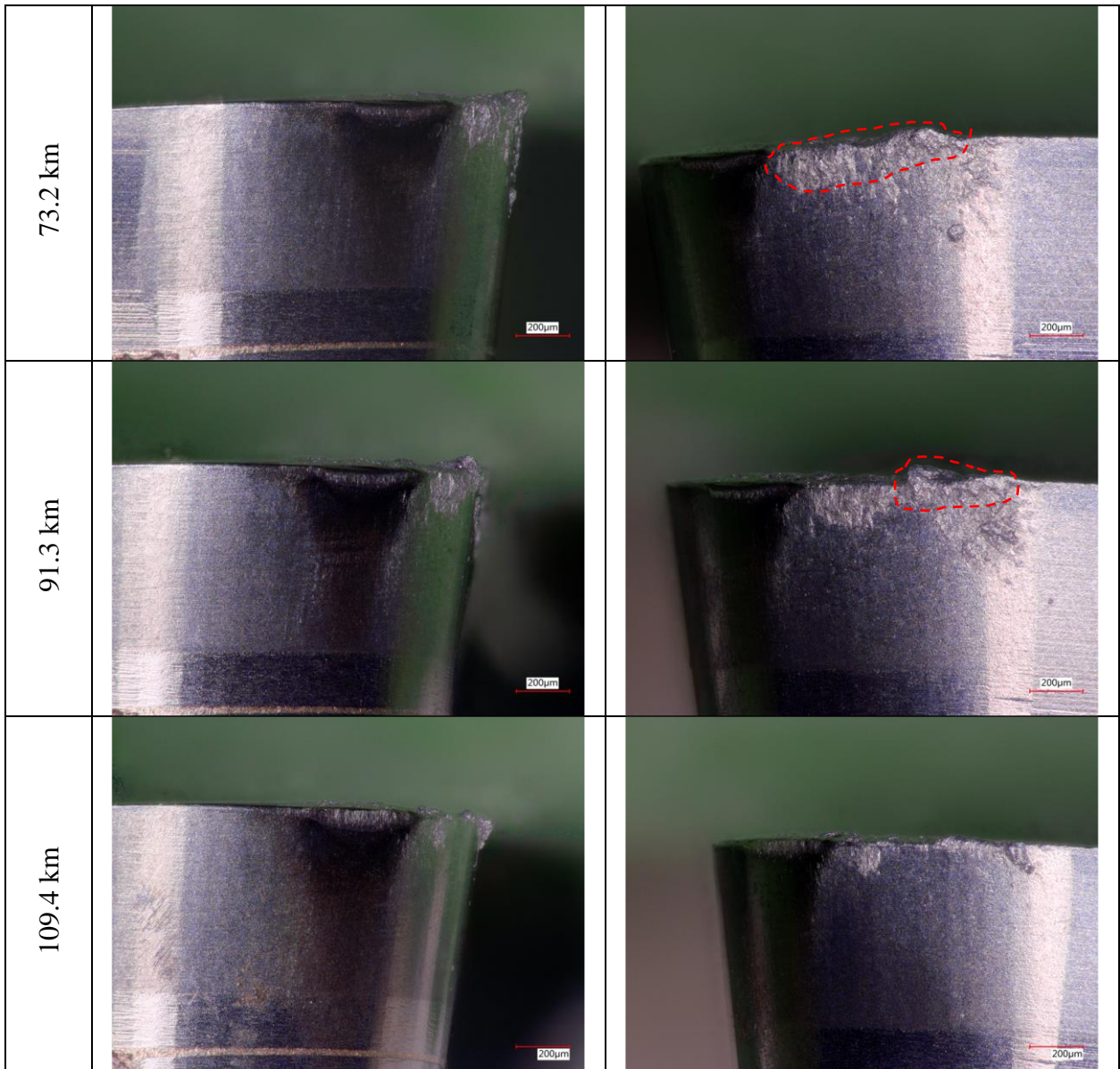


Fig. 30, and Fig. 31 show SEM and EDS analysis results of the tool wear at a cutting length of 134.7 km. Fig. 30(a) shows the entire cutting tool with areas of interest highlighted, i.e. cutting edge, and chip evacuation zone. As shown in Fig. 30(b, c), metal transfer from the workpiece to the cutting tool was considered to be a built-up layer (BUL) at both the cutting edge and the chip evacuation zone. Secondly, as shown in Fig. 30(d),

diffusion was evident on the rake face near the cutting edge. Moreover, abrasion marks were visible on the cutting edge along with accumulated BUL.

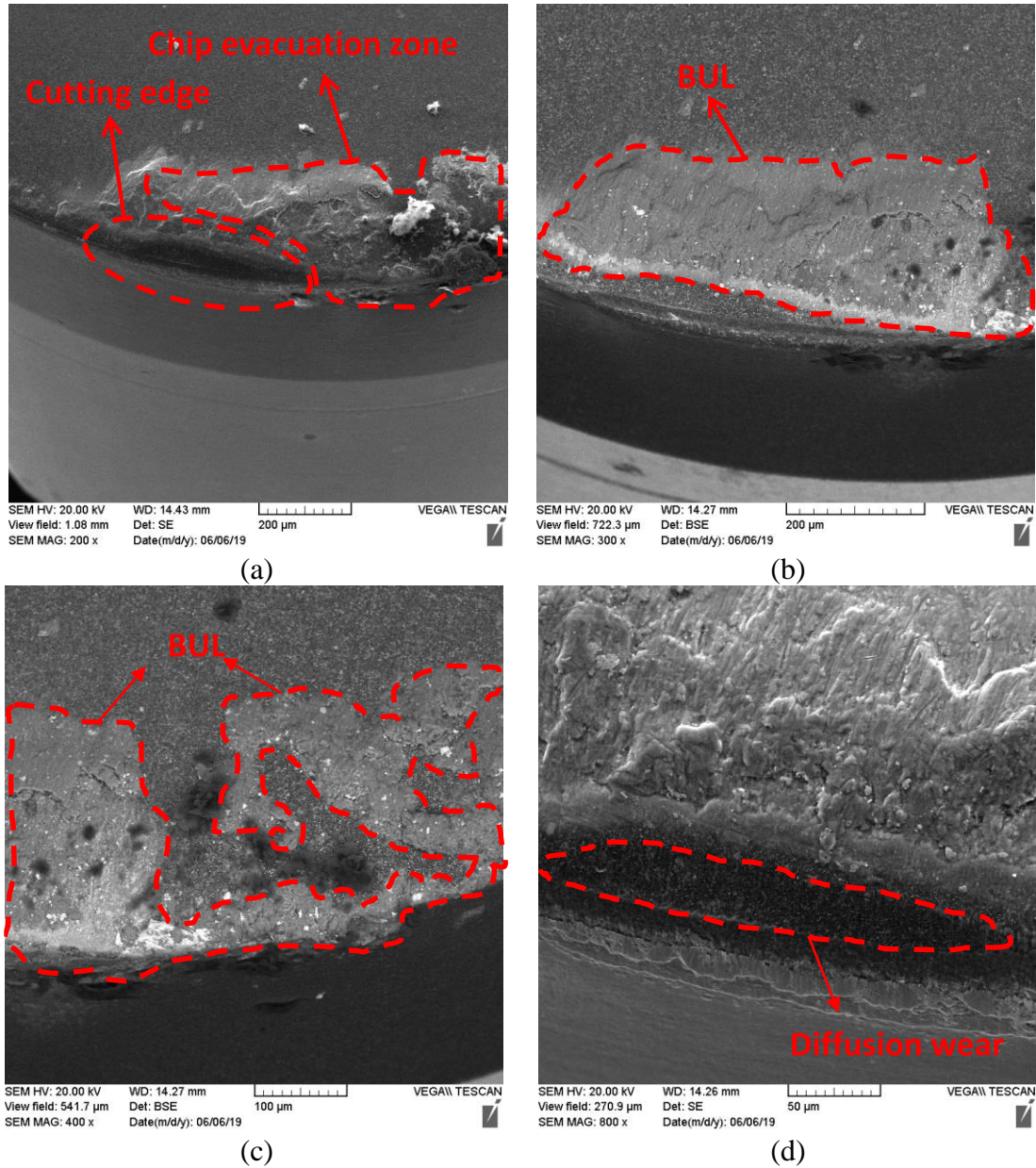
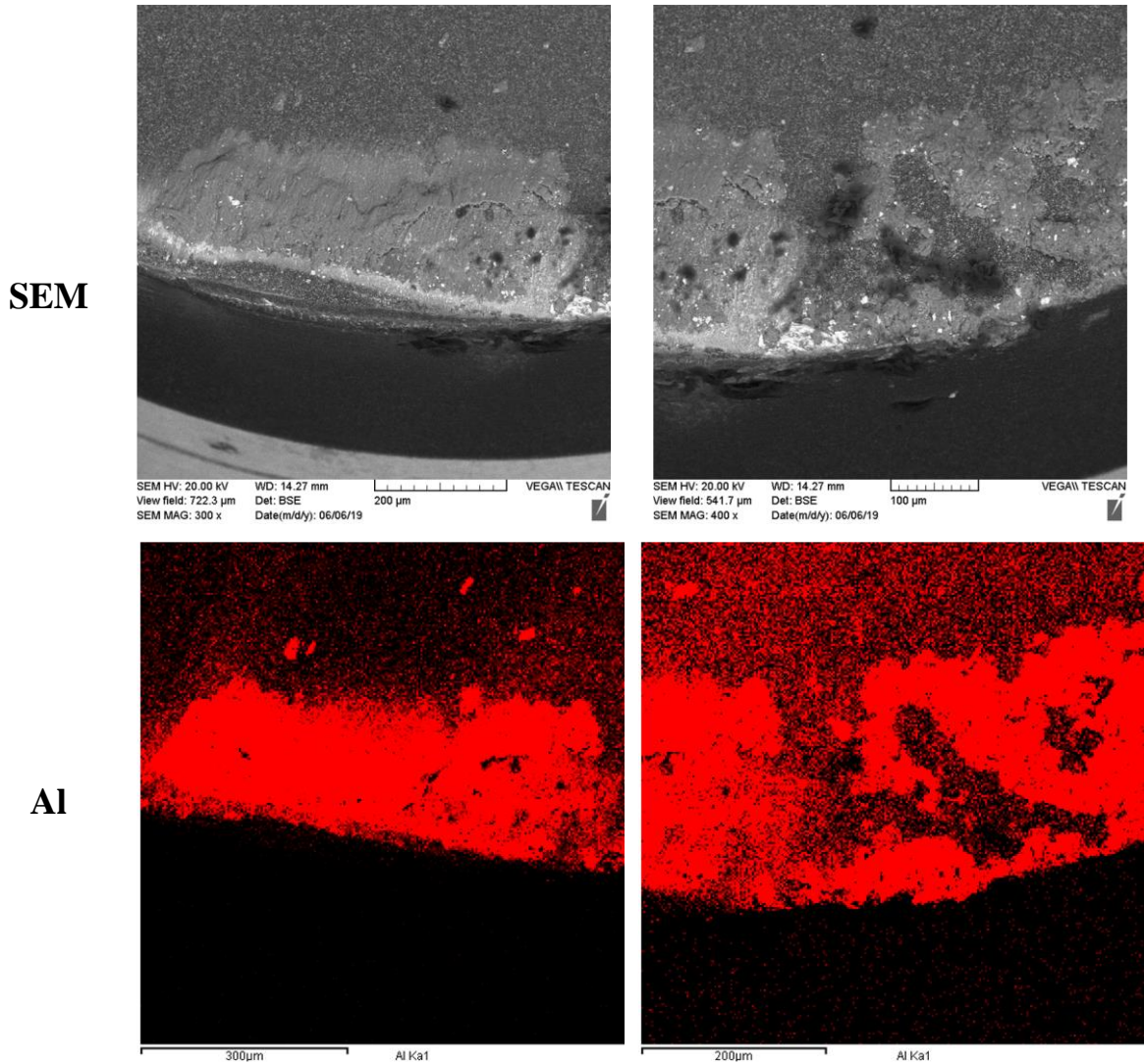


Fig. 30 SEM analysis of Tool Design 2

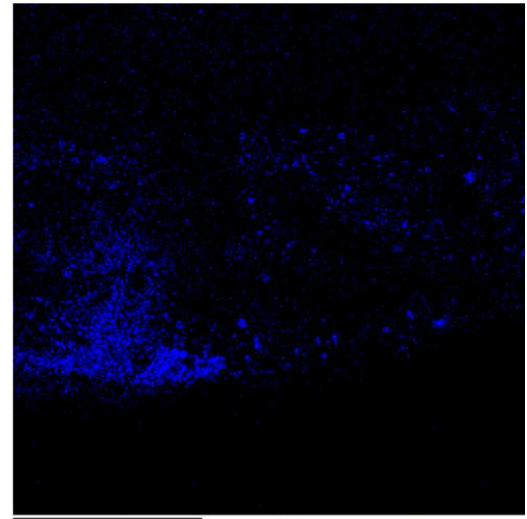
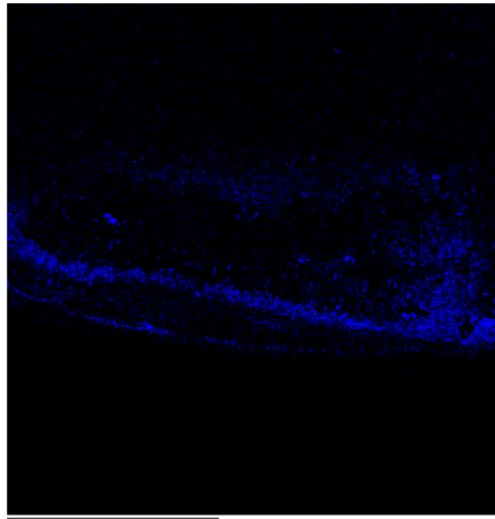
As shown in Fig. 31, the adhered BUL on the cutting edge was found to be composed of aluminum (Al) and iron (Fe), with Al being predominant. However, since the GCI chip

was much smaller than the AISi one, Al was abundant at the chip evacuation zone where Fe was minimal. As the adhered Fe and Al elements were removed during cutting, they carry away CBN particles along with them, causing attrition wear. This attrition was more pronounced on the cutting edge due to the presence of harder Fe particles.

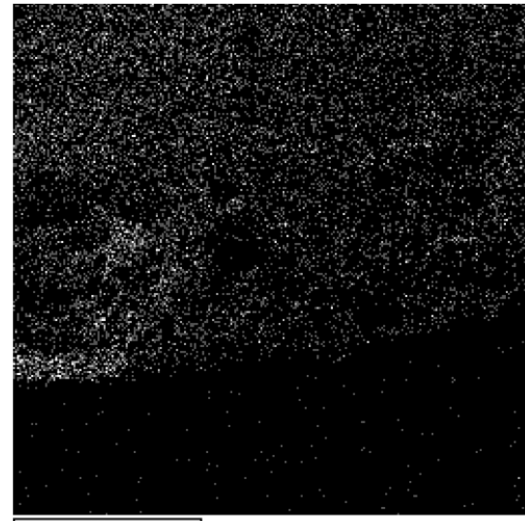
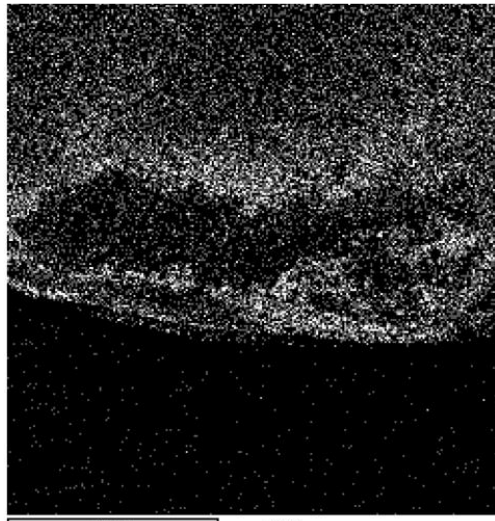
As shown in Fig. 31, the oxide, and MnS layers were observed at both the cutting edge and the chip evacuation zone, where wear progress was limited.



Fe



O



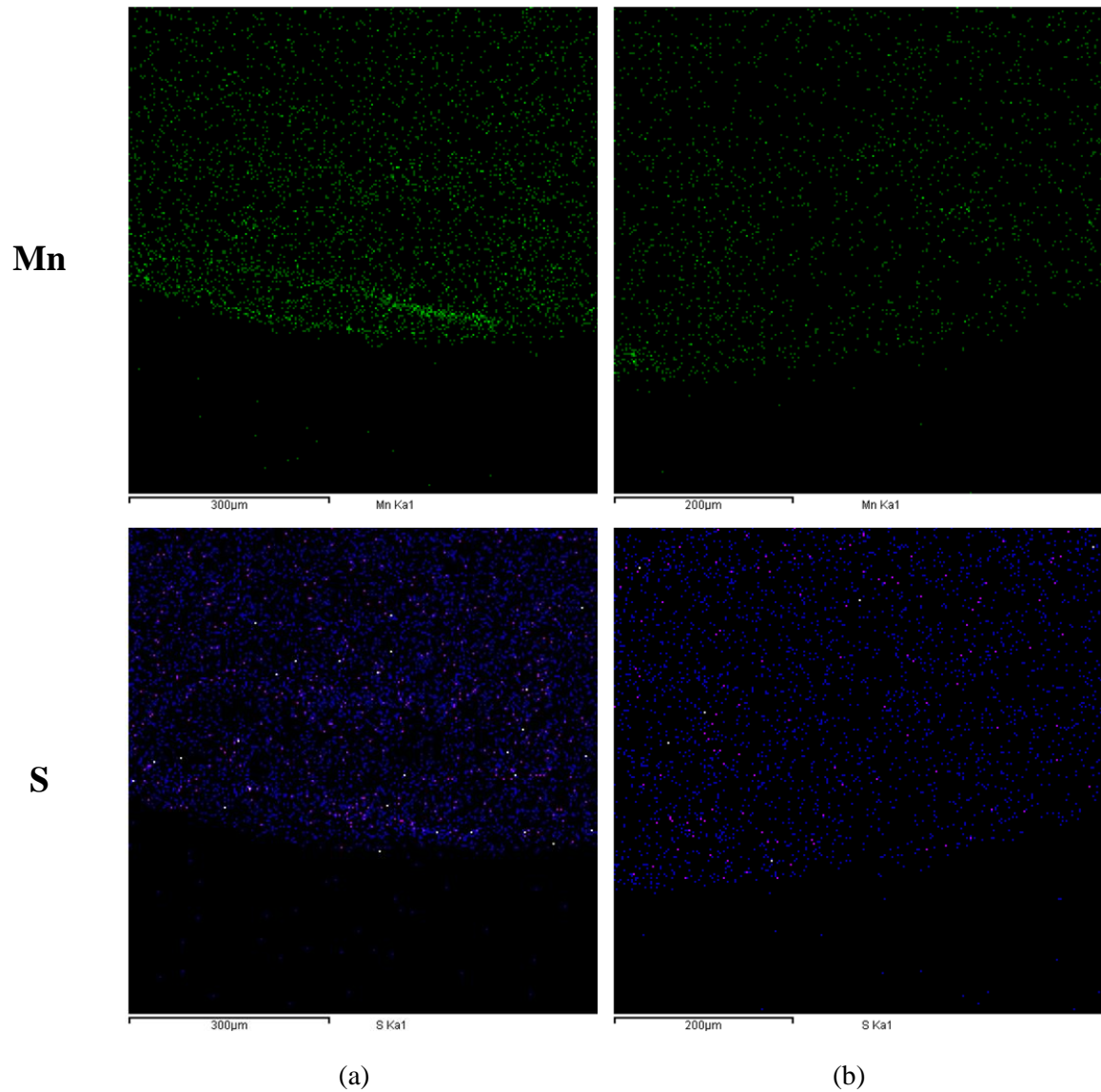


Fig. 31 SEM and EDS analysis of Tool Design2 (a) cutting edge, (b) Chip evacuation zone

In summary, the wear mechanisms of the CBN cutting tool during the turning process of the bimetal AlSi-GCI workpiece were mainly attrition, abrasion, and diffusion.

Aluminum adhesion

Numerical data on the volumetric 3D adhesion measurements is presented in Fig. 32. It was observed that BUL fluctuates between of 0.0002 mm^3 and 0.0028 mm^3 .

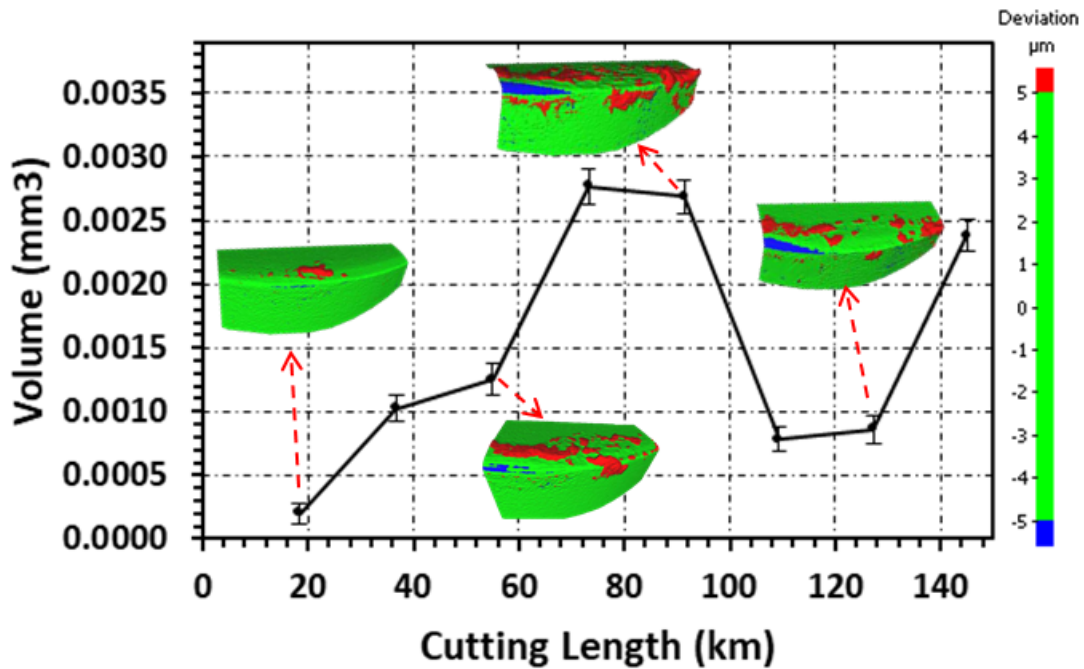


Fig. 32 Accumulation adhesion on the cutting edge with respect to cutting length.

5.2.3 Cutting Forces:

Fig. 33(a) shows that the cutting force increased in both AlSi and GCI until a cutting length of 36.8 km was reached. However, the rate of increase of the GCI part was greater than that of the AlSi section. A similar trend was observed for the feed and radial forces in Fig. 33(b) and Fig. 33(c), respectively. However, the radial force component further increased after 118.3 km. ΔF_f , ΔF_c , and ΔF_r as shown in Fig. 33(d) throughout the cutting length considered in this study.

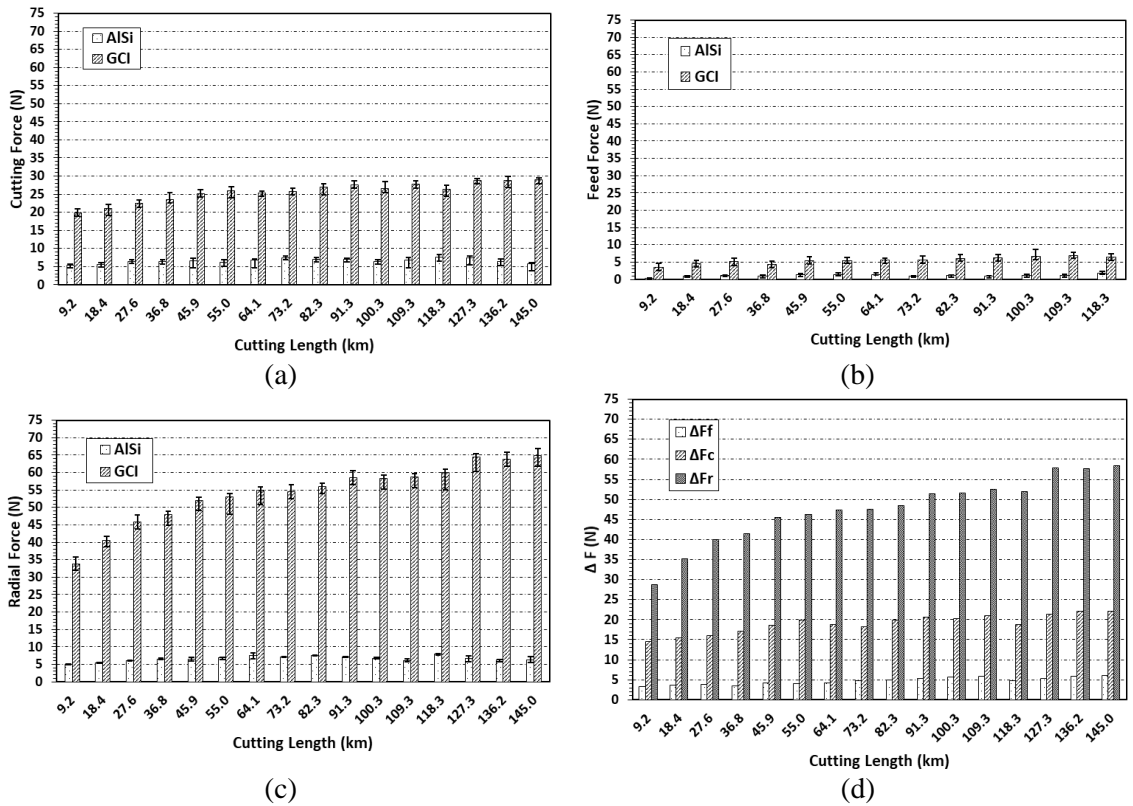


Fig. 33 Variation in force components (a) cutting force, (b) feed force, (c) radial force, and (d) difference in force (Tool Design 2)

ΔF_r increased from 28.8 N at 9.2 km of cutting length to 45.3 N at 36.8 km. After an equal length of cut, ΔF_f increased from 3.3 N to 5.8 N and ΔF_c increased from 14.5 N to 18.6 N.

Fig. 34 shows the radial force ratio Z (demonstrated in Chapter 2), with respect to cutting length. It started with a value of 6.7 at 9.2 km and grew to an average steady-state value of 8.0 after 36.8 km.

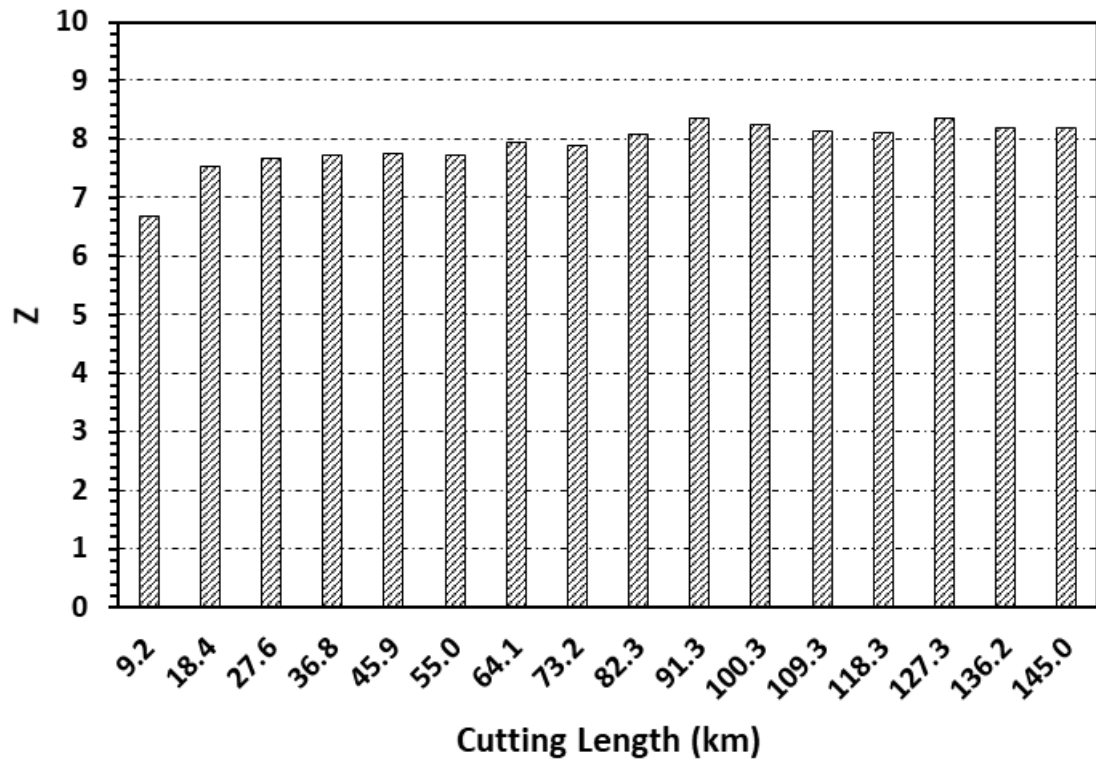


Fig. 34 Progression of Z value with respect to cutting length (Tool Design 2)

5.2.4 Surface roughness:

The measured surface roughness of the AlSi-GCI bimetallic workpiece is shown in Fig. 35. The effects of flank wear progression and adhesion volume were combined in this trend. Like the flank wear trend, shown in Fig. 29, the workpiece roughness stabilized following a gradual increase at the start, with an Ra of 1.05 μm at a cutting length of 37 km. This was influenced by adhesion as shown in Fig. 32. Surface roughness was observed to slowly reduce over the segment of the cutting length from 90 km to 118 km, before rising again at the end of the test.

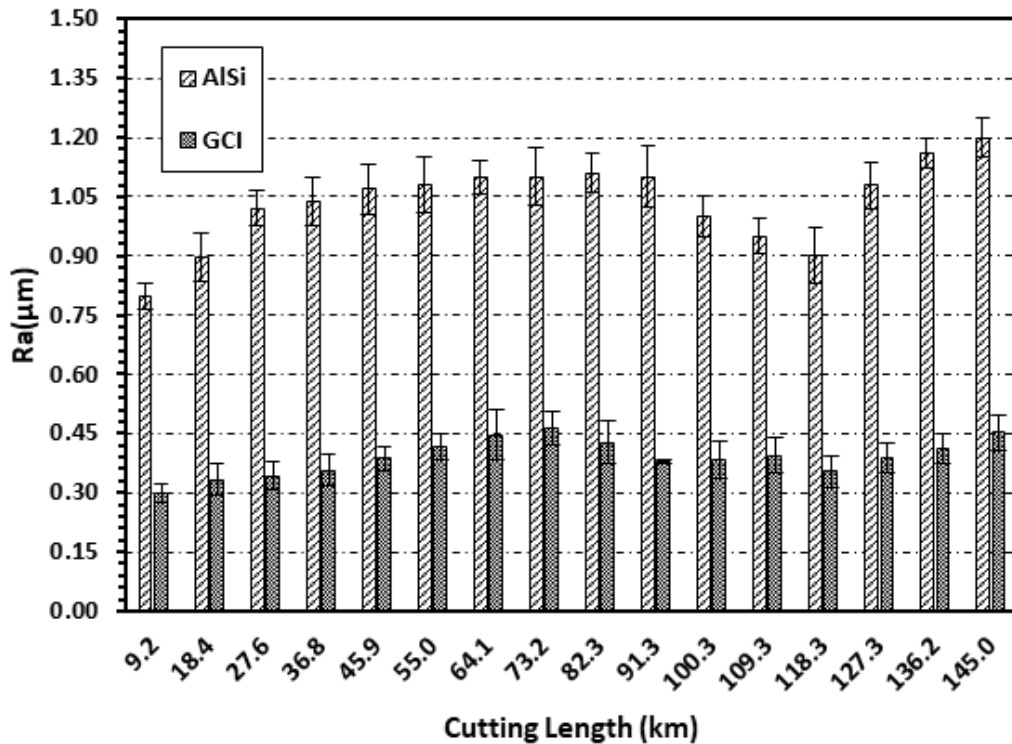


Fig. 35 Variation in surface roughness of machined surface (Tool Design 2)

This pattern can be explained by the corresponding drop in the AlSi adhesion as discussed earlier in Fig. 32. The Ra trend of GCI was very similar to that of AlSi. However, the Ra magnitudes of GCI were less than half of those of AlSi at a corresponding cutting length.

5.3 Comparison

As mentioned in Chapter 3, Tool Design 1 and Tool Design 2 differ only in geometry, with edge radii being $14 \mu\text{m}$ and $22 \mu\text{m}$, respectively. Moreover, Tool Design 1 had an unprepared edge with a rake angle of $+5^\circ$, whereas Tool 2 had a honed edge with a rake angle of -2° . To compare the performance of these two tools, the average magnitudes of the performance metrics (tool life, cutting forces, and workpiece roughness) within the steady-state zone were taken into consideration. The steady-state zones of Tool 1 and Tool

2 were found to be 34.9-118.5 km and 36.8-118.3km, respectively. summarizes the performance of Tool 1 and Tool 2, based on the machinability criteria discussed during this study, i.e. tool life, tool wear behaviour, cutting forces and workpiece surface roughness.

Table 8 summarizes the performance of Tool 1 and Tool 2, based on the machinability criteria discussed during this study, i.e. tool life, tool wear behaviour, cutting forces and workpiece surface roughness.

Table 8 Machinability comparison of Tool 1 against Tool 2

Criteria/Tool#		Tool 1	Tool 2
Tool life	Flank wear	48 μm	56 μm
	Cutting length	83.6 km	81.5 km
Wear behavior	Mechanism	Attrition, Abrasion, and Diffusion	
	MnS	✓	✓
	Oxides	✓	✓
	BUL/BUE	✓	✓
Cutting forces	ΔF_r	45.1 N	48.3 N
	ΔF_c	19.7 N	18.6 N
	ΔF_f	8.3 N	5.8 N
	Z	7.0	8.0
Workpiece roughness	AlSi	0.80 μm	1.07 μm
	GCI	0.35 μm	0.40 μm

5.3.1 Tool life

Tool life was quite similar in Tool Design 1 and Tool Design 2, with the steady-state flank wear lasting up to a cutting length of 118 km.

The slight geometrical differences between Tool 1 and Tool 2, i.e. rake angle and edge radius, had no direct influence on their respective tool life.

5.3.2 Wear behaviour

The primary wear mechanisms of the two CBN tools during turning of a bimetallic AlSi-GCI workpiece under dry cutting conditions were attrition, abrasion and diffusion. However, the magnitudes of adhesion and diffusion were slightly greater in Tool Design 2. Secondly, protective oxide and MnS films were found on both Tool Design 1 and Tool Design 2, with higher concentrations being present in the latter.

The greater adhesion and diffusion of Tool Design 2 are attributed to the higher temperature generation at the cutting zone due to the lower rake angle and the greater edge radius of Tool Design 2. Consequently, AlSi and GCI on Tool Design 2 undergo more thermal softening, increasing the volume of adhesion. However, the higher concentration of oxides and rates of diffusion on Tool Design 2 can be also attributed to its higher cutting temperature at which the CBN binder materials are less stable.

5.3.3 Cutting forces

All cutting force components varied throughout the cutting process, with the variation in radial force ΔF_r 7% lower in Tool Design 1 compared to Tool Design 2. Also, the radial force ratio Z of Tool Design 1 was 13% lower than that of Tool Design 2.

The slightly higher force and radial force ratio of Tool Design 2 were attributed to its smaller rake angle. The smaller rake angle of Tool Design 2 increased the friction between the chip and the cutting tool. Hence, the cutting forces were observed to increase accordingly.

5.3.4 Surface roughness

Workpiece roughness was always higher in AlSi as compared to GCI. However, Ra of Tool Design 1 was 14% lower in the GCI and 25% in the AlSi components compared to Tool Design 2.

This higher workpiece roughness can be attributed to the greater adhesion volume on Tool Design 2 related to BUE formation. The greater rake angle of Tool Design 1 facilitated better chip evacuation and lowered the degree of thermal softening of AlSi. This reduced the degree of adhesion and the amount of BUE formation and, as a consequence, the surface roughness as well.

Chapter 6 NUMERICAL INVESTIGATIONS & MACHINABILITY IMPROVEMENT

Numerical simulations for the experimental work which compared two different tool designs of CBN are discussed in this chapter. A numerical parametric study to improve the machinability of the bimetal workpiece is also presented.

6.1 Impact of tool design on thermo-mechanical behaviour

To further understand the machinability of the bimetallic AlSi-GCI workpiece, the thermo-mechanical behaviour of Tool Design 1 and Tool Design 2 was numerically studied under the experimental study conditions with the developed FEA model. The studies discussed in this section were performed under the assumption that the tools were not worn out.

6.1.1 Tool Design 1

Fig. 36 shows the variation of cutting tool maximum temperature along l_c . As the tool cut through AlSi, its maximum temperature rose to an average steady value of 261°C. The tool temperature increased further in GCI to an average of 576°C. The tool went through the same cycle again until it reached an average of 306°C in AlSi. This slightly higher average was caused by the tool being preheated during GCI cutting in advance of entering the AlSi.

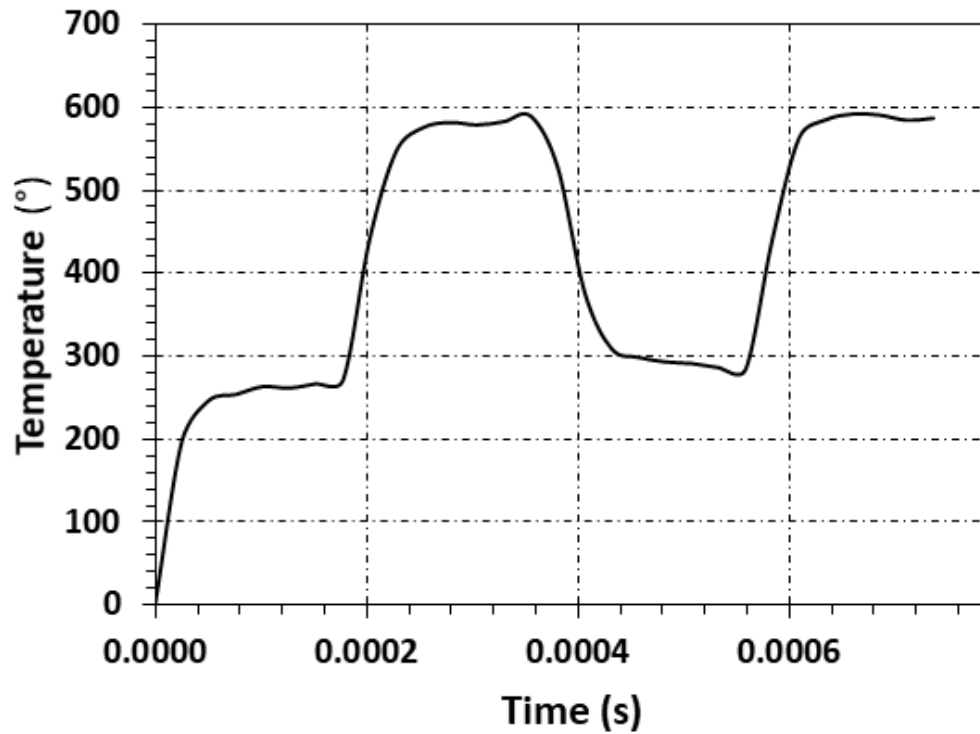
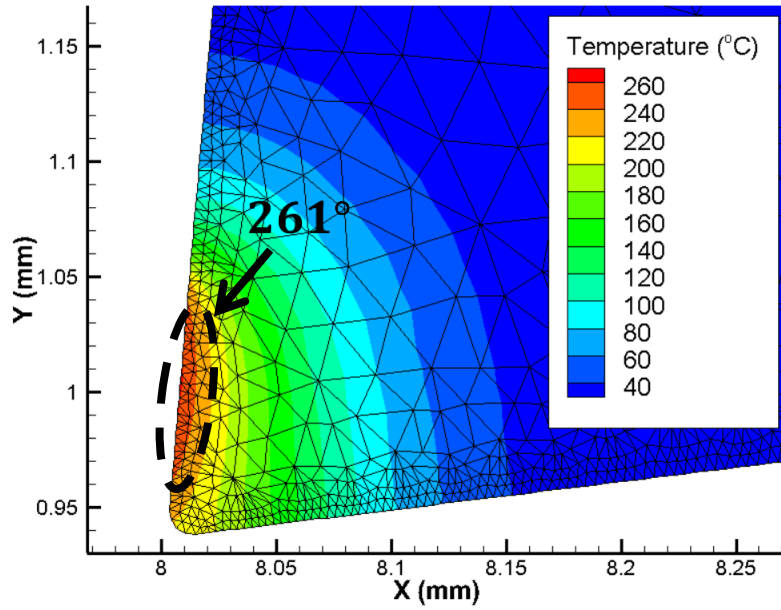
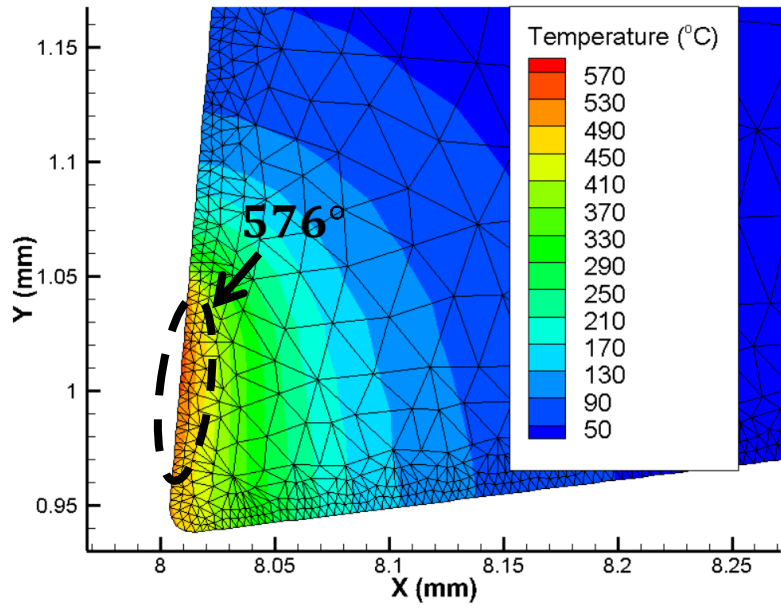


Fig. 36 Variation of maximum tool temperature with respect to time (Tool Design1)

The temperature distributions on the CBN tool that resulted from cutting AlSi and GCI are shown in Fig. 37. It was observed that the maximum tool temperature for both AlSi and GCI occurred at the tool rake face away from the tool tip.



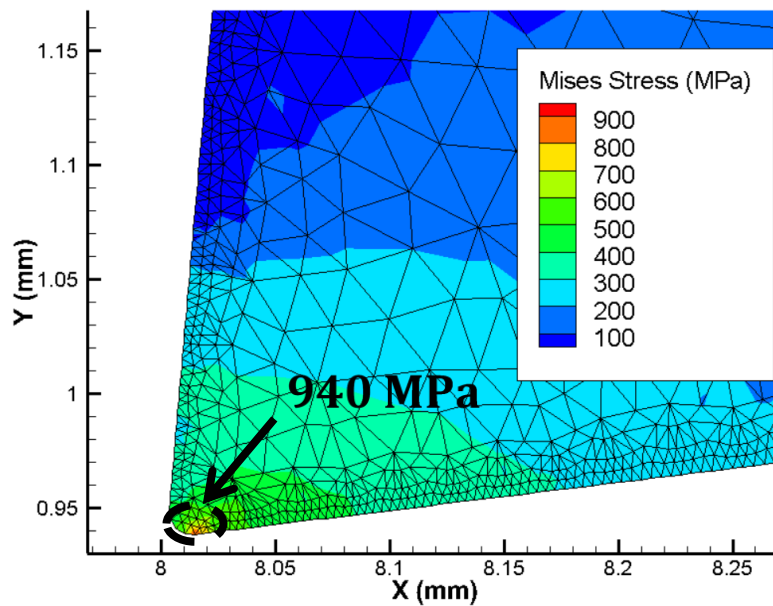
(a)



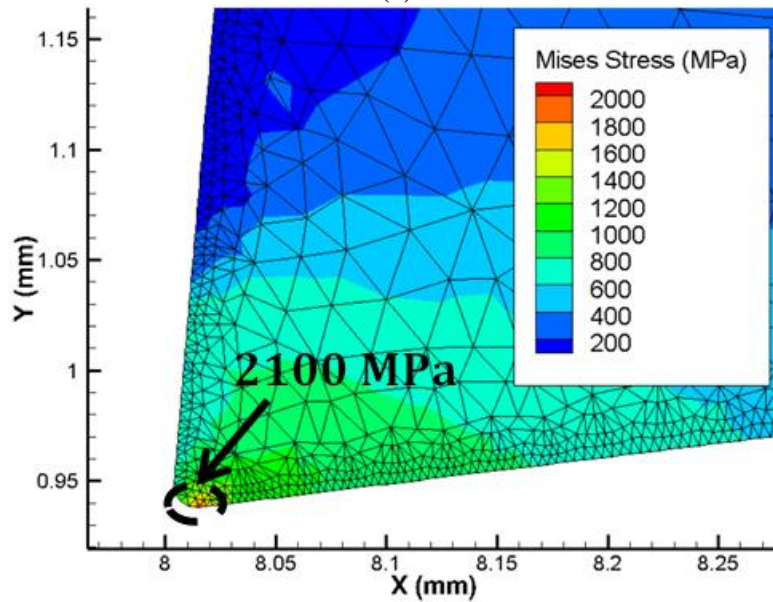
(b)

Fig. 37 Cutting tool temperature distribution on rake face (a) AISi and (b) GCI (Tool Design 1)

The distributions of Von Mises stresses on the CBN cutting tool due to cutting AlSi, and GCI are shown in Fig. 38. The location of maximum stress was observed at the flank side of the tool tip.



(a)



(b)

Fig. 38 Mechanically induced stresses during cutting process (a) AlSi and (b) GCI (Tool Design 1)

6.1.2 Tool Design 2

Fig. 40 shows the variation of cutting tool maximum temperature along l_c . Initially, as the tool cuts through AlSi, its maximum temperature rose to an average steady value of 270°C. The tool temperature increased further in the GCI to reach an average value of 590°C. The tool goes through the same cycle again with an average of 306°C in AlSi. This slightly higher average was attributed to the tool being preheated while cutting the GCI material.

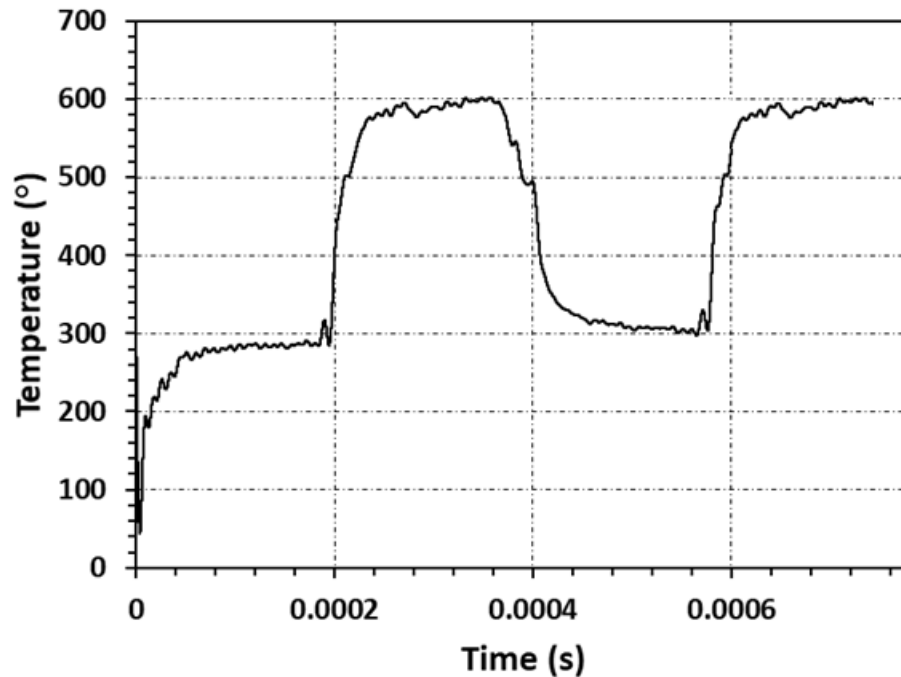
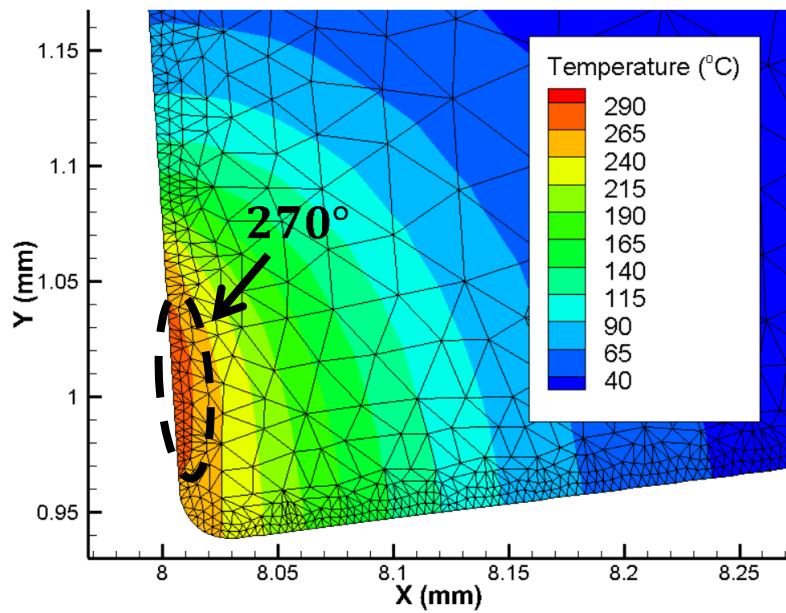
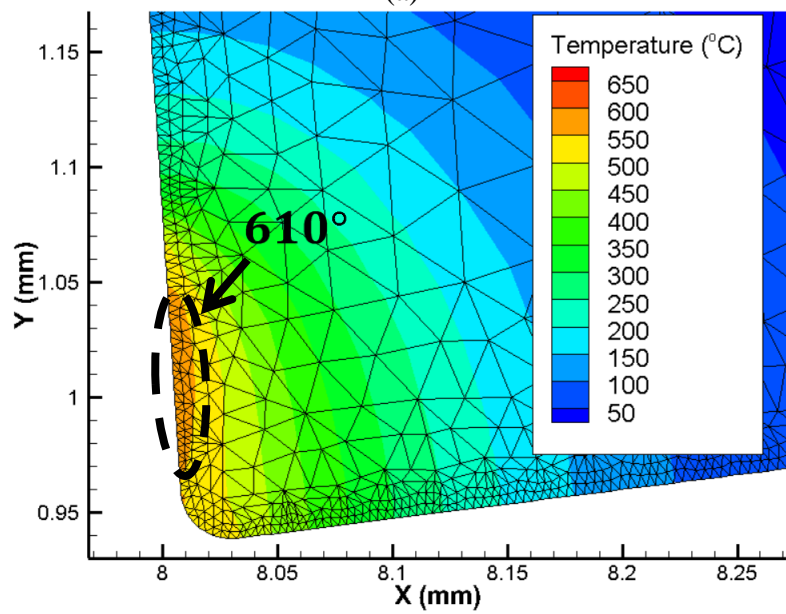


Fig. 39 Variation of maximum tool temperature with respect to time (Tool Design 2)

The temperature distributions on Tool Design 2 that resulted from cutting AlSi, and GCI are shown in Fig. 41. The maximum tool temperature generated when cutting AlSi, and GCI, occurred at the tool rake face away from the tool tip.



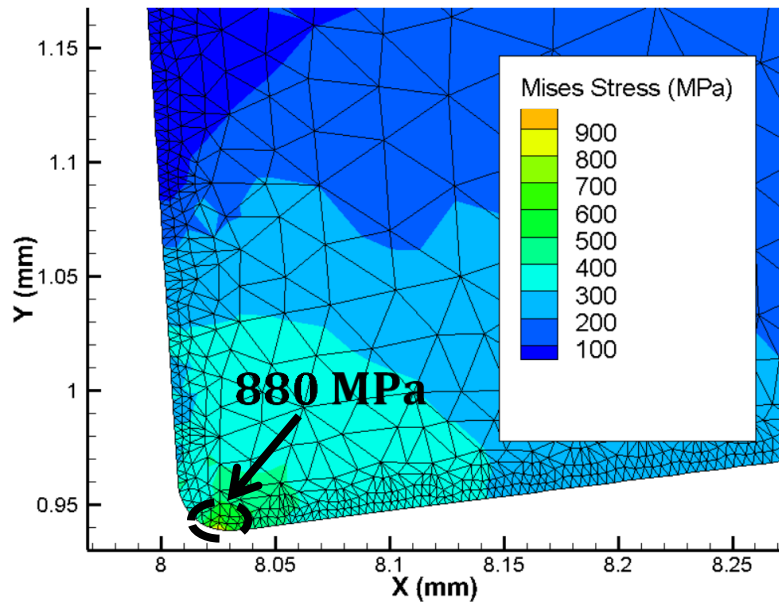
(a)



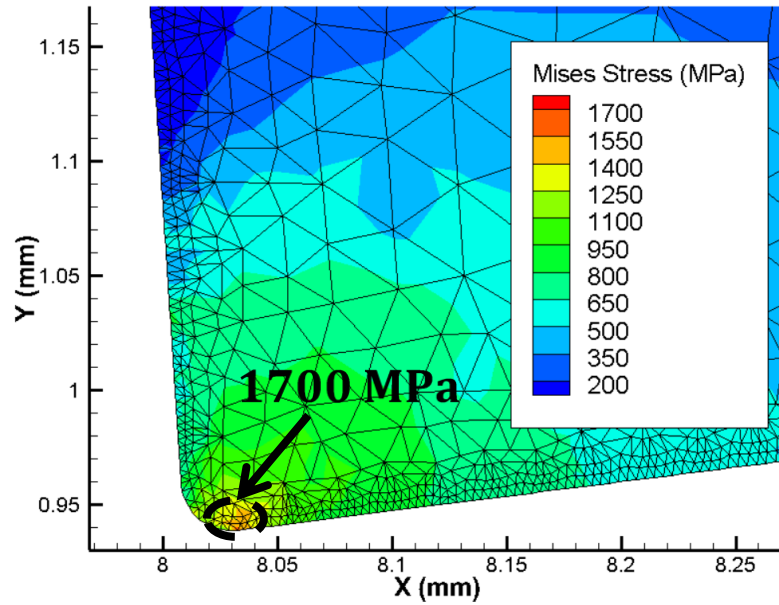
(b)

Fig. 40 Cutting tool temperature distribution on rake face (a) AlSi and (b) GCI (Tool Design 2)

The distributions of Von Mises stresses on Tool Design 2 due to cutting AlSi and GCI are shown in Fig. 42. The location of maximum stress was observed at the flank side of the tool tip.



(a)



(b)

Fig. 41 Mechanically induced stresses during cutting process (a) AlSi and (b) GCI (Tool Design 2)

6.1.3 Discussion and Comparison

Tool cutting temperature

Since the cutting forces associated with cutting GCI were greater than AlSi, its tool temperatures were higher than those of AlSi in both tools. As shown in the FEA material model in Chapter 4, (Eq. 4.2), the generated frictional heat is directly a function of the cutting force.

Since the cutting forces for GCI were greater, its tool temperatures were higher than those of AlSi in both tools. As shown in the FEA material model in Chapter 4, (Eq.4.2), the generated frictional heat was directly a function of the cutting force.

Table 9 summarizes the values of tool temperature on the flank and the rake faces of Tool Design 1, and Tool Design 2 due to cutting AlSi and GCI. Since the cutting forces for GCI were greater, its tool temperatures were higher than those of AlSi in both tools. As shown in the FEA material model in Chapter 4, (Eq.4.2), the generated frictional heat was directly a function of the cutting force.

Table 9 Temperature comparison of Tool Design 1 against Tool Design 2

Material	Temperature, °			
	Flank		Rake	
	Tool 1	Tool 2	Tool 1	Tool 2
AlSi	160	240	261	270
GCI	370	500	576	610

To be specific, Tool Design 2 generated higher temperatures in both the AlSi and GCI parts as compared to Tool Design 1. This temperature difference between Tool Design 2, and Tool Design 1 was higher at the flank face as compared to the rake face. The higher edge radius of Tool Design 2 increased the friction value on the flank face as well as plastic

deformation in the secondary shear zone, which then produced more heat near the cutting edge. However, the increased edge radius was deemed more favourable since it increased the surface area over which the generated heat could be dissipated [33].

Tool mechanical stresses

summarizes the values of maximum Von Mises stresses on the cutting edge and the rake face of Tool Design 1 and Tool Design 2 for both AlSi₁₀Mg, and GCI. The stresses are listed with a minus sign to indicate their compressive nature. The stress magnitudes of Tool 1 were higher than those of Tool 2. Furthermore, compared to the rake face, the stresses at the edge are significantly higher for both tools due to the higher edge radius of Tool 2. It is known that increasing the cutting-edge radius enhances edge stability. Cutting edge rounding was observed to help distribute forces over the tool tip and reduce stress concentration [33].

Table 10 summarizes the values of maximum Von Mises stresses on the cutting edge and the rake face of Tool Design 1 and Tool Design 2 for both AlSi₁₀Mg, and GCI. The stresses are listed with a minus sign to indicate their compressive nature. The stress magnitudes of Tool 1 were higher than those of Tool 2. Furthermore, compared to the rake face, the stresses at the edge are significantly higher for both tools due to the higher edge radius of Tool 2. It is known that increasing the cutting-edge radius enhances edge stability. Cutting edge rounding was observed to help distribute forces over the tool tip and reduce stress concentration [33].

Table 10 Von Mises stresses comparison of Tool Design 1 against Tool Design 2

Material	Mechanical stress, MPa			
	Edge		Rake	
	Tool 1	Tool 2	Tool 1	Tool 2
AlSi	-940	-880	-450	-400
GCI	-2100	-1700	-800	-750

6.2 Numerical study on machinability improvement

Since the experimental studies of AlSi-GCI workpiece machining revealed a significant variation in the machining forces, the objective of this numerical study was to improve the machinability of the AlSi-GCI workpiece by reducing this variation. This was accomplished in this study by performing a parametric study designed with Taguchi's approach and verified with the developed FEA model. Finally, the output was validated experimentally. These studies were carried out on Tool Design 1.

6.2.1 Taguchi's DoE:

Taguchi developed Orthogonal Arrays (OAs), which are a family of fractional factorial experimental matrices. These OAs can be implemented in various situations. The main reason for implementing a Taguchi Design of Experiment (DoE) is to study the main effects and obtain desirable performance at a minimum cost. Taguchi denotes an orthogonal array by:

$$L_N(S^k)$$

where:

N = total number of trials during experimentations.

k = number of factors

s = number of levels for each factor

The advantages of implementing Taguchi can be summarized as follows:

- Taguchi provides desired experimental information with a minimal number of experimental trials. For example, for an experiment with 7 factors and 2 levels, which requires 128 full factorial experimental trials, Taguchi L8 OA (one-sixteenth fractional factorial design) reduces the tests to only 8 trials.
- Taguchi also permits consideration of all potential factors that are suspected to have an impact on the performance (responses). Therefore, the experimenter would be able to uncover the significant factors affecting product performance and therefore track down the most desirable combination of factors which will yield improved results (performance).
- Taguchi's design is simple, easy to perform, and applicable to various engineering applications.

A Taguchi DoE involves the following steps:

- 1- Problem statement and study objectives.
- 2- Determine the output response and its measurements.
- 3- Identify variables that affect the response (Factors).
- 4- Separate the factors into control and noise factors.
- 5- Determine the number of levels and their values for all factors.

- 6- Perform the selection of a suitable orthogonal array for the DOE.
- 7- Conduct the experiment.
- 8- Analyze the data.
- 9- Interpret the results and draw conclusions.

Analysis:

Once the Taguchi design is performed, the effects of control variables should be analyzed and interpreted. To determine the average effects of control factors, average (mean) calculations of the results of the experiments can be implemented, thereby determining the desired operation conditions (Levels). However, simply calculating the average does not capture the variability of data within the parameter group. Therefore, statistical techniques with the ability to capture the variability of a population (factors and levels) were used in this study, particularly signal to noise (S/N) and analysis of variance (ANOVA).

Signal to Noise ratio (S/N):

Contrary to the simple average analysis, the S/N ratio approach uses the mean-squared deviation (MSD) of the results. To accommodate a wide-range of data and for the ease of data linearity, a logarithmic transformation of MSD was used to analyze the results of this study with the logarithmic transformation of the MSD called the S/N ratio.

For the S/N ratio analysis, there are different optimization scenarios, the most common three are listed below:

- 1- Nominal is best:

$$\frac{S}{N} = -10 \times \log_{10}(\sigma^2)$$

- 2- Larger is better

$$\frac{S}{N} = -10 \times \log_{10}\left(\frac{\sum(1/Y^2)}{n}\right)$$

3- Smaller is better

$$\frac{S}{N} = -10 \times \log_{10}\left(\frac{\sum Y^2}{n}\right)$$

Where:

σ = standard deviation of the responses for all noise factors for the given factor level combination

Y = responses for the given factor level combination

n = number of responses in the factor level combination.

Analysis of Variance (ANOVA):

ANOVA is a method that partitions the total variation of a variable (response) into components attributed to accountable sources (factors) of the variation in an experiment.

ANOVA is a statistical approach used to analyze experimental data and draw conclusions about the parameters under study and take decisions accordingly. ANOVA's basic equation is given by:

$$SS_T = SS_F + SS_E$$

Where:

SS_T = Total sum of squares

SS_F = Sum of squares due to factors

SS_E = Sum of squares due to error

ANOVA table:

ANOVA metrics and computed values with their formulae are shown in Table 5.

Table 11 ANOVA computations

Source of Variation	Sum of Squares	Degrees of Freedom	Mean Square Variance	F _o	% Contribution
Factor	SS_F	K - 1	$V_F = \frac{SS_F}{K} - 1$	$\frac{V_F}{V_E}$	$\frac{SS_F}{SS_T}$
Error	SS_E	N - K	$V_E = \frac{SS_E}{N} - K$		
Total	SS_T	N - 1			

Where:

K = Number of levels of factors

N = Number of experiment trials

V_F = Variance of factor

V_E = Variance of error

F_o = Computed F-ratio

F-test

The computed F-ratio is a measure of whether the effects of the factors are significant or not. For example, if the experiment has two factors being studied, there would be an F-value associated with each factor. Comparing the F-values, the factor with higher F-value would have more significance on the response variation.

Percent contribution

Percent contribution for each factor is calculated to have a measure of how much each factor contributes to the response variance by simply dividing the sum of squares of the factor by the total sum of squares.

Now that both F-ratios and % contributions of the factors are calculated, the experimenter would have measures of how much each factor contributes to the performance; thus, conclusions could be drawn more confidently.

6.2.2 DOE setup

Following Taguchi's procedure mentioned above, the noise factors, the control factors and their levels, and the suitable orthogonal array were determined as follows:

Response/noise factors

Based on the study objectives, the response parameter of Taguchi's design was the difference between the GCI and AISi cutting forces denoted by ΔF_c .

Control factors and their levels

In metal cutting mechanics, the estimation of machining forces can be best achieved in terms of total specific cutting energy (u). The specific cutting energy is essentially independent of the cutting speed (v) over a broad range of values. In addition, the following factors have a considerable impact on cutting forces [4]:

- 1- Workpiece physical, chemical, and mechanical properties. Specific cutting energy is approximately proportional to material hardness.
- 2- Cutting tool rake angle (α). Specific cutting energy decreases by about 1% per degree increase in the rake angle.
- 3- Undeformed chip thickness(f).

In addition to these factors, during discontinuous chip and BUE formation, the cutting forces might vary during discontinuous chip and BUE formation as follows: Discontinuous chip formation would usually generate lower forces.

- Generally, the presence of BUE would reduce the forces by an amount depending on its size.
- Cutting forces would tend to increase along with strain-hardening.
- Cutting forces can usually be reduced by controlled contact length tool design. This depends on whether the standard contact length is larger or smaller than the optimal contact length.
- Cutting forces would grow when using a chamfer protected tool tip. [4]

The factors in the current study that could affect the output response the most were taken to be the cutting parameters and tool design, particularly the feed, cutting speed, and rake angle of the tool, making $k=3$. **Error! Reference source not found.** shows three control factors (feed, cutting speed, and rake angle of the tool) considered at four different levels. Level two values represent the experimental study conditions. One output response, ΔF_c , represents the design's noise factor.

Table 12 Cutting parameters and their levels

Factor	Symbol	Level 1	Level 2	Level 3	Level 4
Feed (mm/rev)	A	0.0309	0.0618	0.1236	0.2472
Speed (m/min)	B	430	630	830	1030
Rake angle (°)	C	0	5	10	15

A Taguchi $L_{16}(4^3)$ orthogonal array with 16 experimental trials was selected to perform a numerical parametric study, as shown in Table 13.

Table 13 Orthogonal array of Taguchi $L_{16}(4^3)$

Experiment no.	Factor A	Factor B	Factor C
1	1	1	1
2	1	2	2
3	1	3	3
4	1	4	4
5	2	1	2
6	2	2	1
7	2	3	4
8	2	4	3
9	3	1	3
10	3	2	4
11	3	3	1
12	3	4	2
13	4	1	4
14	4	2	3
15	4	3	2
16	4	4	1

6.2.3 Parametric study- Results and Discussion

The experiments based on the developed orthogonal array (16 experiments) were numerically carried out using AdvantEdge. After 16 AdvantEdge trials, the results of ΔF_c were recorded in Table 8.

Signal to Noise ratio (S/N)

As shown in Table 8, S/N ratios were computed for each experimental trial of ΔF_c .

Table 14 The results of experiments and S/N ratios

Experiment no.	Control factors			ΔF_c (N)	S/N for ΔF_c (dB)
	Feed (mm/rev)	Cutting Speed (m/min)	Rake Angle (°)		
1	0.0309	430	0	1.75	-4.86
2	0.0309	630	5	1.62	-4.19
3	0.0309	830	10	1.11	-0.91
4	0.0309	1030	15	1.46	-3.29
5	0.0618	430	5	2.95	-9.40
6	0.0618	630	0	3.11	-9.86
7	0.0618	830	15	3.20	-10.10
8	0.0618	1030	10	3.23	-10.17
9	0.1236	430	10	6.40	-16.12
10	0.1236	630	15	6.50	-16.26
11	0.1236	830	0	6.45	-16.19
12	0.1236	1030	5	6.75	-16.59
13	0.1854	430	15	6.80	-16.65
14	0.1854	630	10	7.15	-17.09
15	0.1854	830	5	7.70	-17.73
16	0.1854	1030	0	8.03	-18.09

Table 15 lists the calculated average S/N ratio for each control factor per level. For example, trials numbered, 1, 2, 3, and 4, correspond to factor 1 at level one and their average was calculated as:

$$S/N_{average, \Delta F_c} = \frac{-4.86 + (-4.19) + (-0.91) + (-3.29)}{4} = -3.31$$

Table 15 S/N response table for ΔF_c factor

Levels	Control Factors		
	Average S/N for Cutting Force Difference (ΔF_c)		
	Feed	Speed	Rake Angle
Level 1	-3.311*	-11.758	-12.25
Level 2	-9.881	-11.847	-11.976
Level 3	-16.29	-11.233*	-11.072*
Level 4	-17.39	-12.035	-11.575
Delta	14.079	0.802	1.179
Rank	1	3	2

* indicate the best levels of control factors

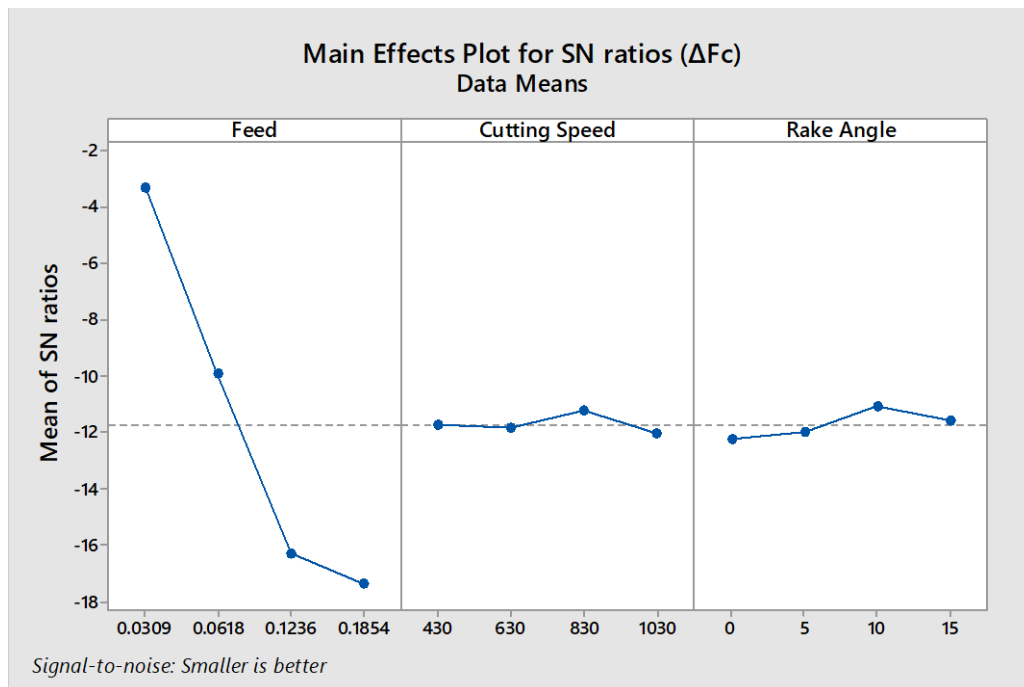


Fig. 42 Effect of process parameters on average S/N ratios for ΔF_c

Since the formula used to analyze Taguchi DOE is ‘smaller is better’, the lowest response value was obtained by maximizing the S/N ratios. The S/N values denoted with “*” in Table 15 correspond to the lowest responses. Also, Fig. 42 shows the S/N ratios for all the factors and their levels with respect to the overall mean.

The lowest value of ΔF_c was obtained when the control factors, i.e. feed, cutting speed and rake angle were set to 0.0309 mm/rev, 830 m/min and 10° , respectively.

ANOVA

ANOVA was carried out to measure the degree that each factor contributed to the response variance. Table 16 shows the results of the ANOVA analysis. Feed was revealed to be by far the most dominant contributor to the cutting force variability ΔF_c with a contribution percentage of 98.68%. Rake angle and cutting speed contributed a negligible 0.43% and 0.34% respectively.

Table 16 Results for ANOVA for ΔF_c

Variance Source	Degree of freedom	Sum of Squares SS	Mean Squares	F Ratio	Contribution %
Feed*	3	94.17	31.39	359.83	98.68
Cutting Speed	3	0.32	0.1081	1.24	0.34
Rake Angle	3	0.41	0.1363	1.56	0.43
Error	6	0.52	0.0872		0.55
Total	15	95.43			

* indicate the highest contributing control factor

This parametric study revealed that the feed rate was by far the most significant control factor and the best performance could be achieved at 0.0309 mm/rev. However, operating at such a low feed rate (30 $\mu\text{m}/\text{rev}$) is not advisable since ploughing takes place as the feed

approaches the cutting tool edge radius (10 to 25 μm). Therefore, a slightly higher feed of 0.045 mm/rev was recommended for practical use.

6.2.4 Experimental validation

To validate the output of the numerical parametric study, an experimental machining test was conducted for Tool Design 1. The validation experiment was carried out at a reduced feed rate of 0.045 mm/rev (f_2) and all other conditions unchanged from the experimental study. Fig. 43 shows the variation in force components and difference in forces during the machining of the two different materials.

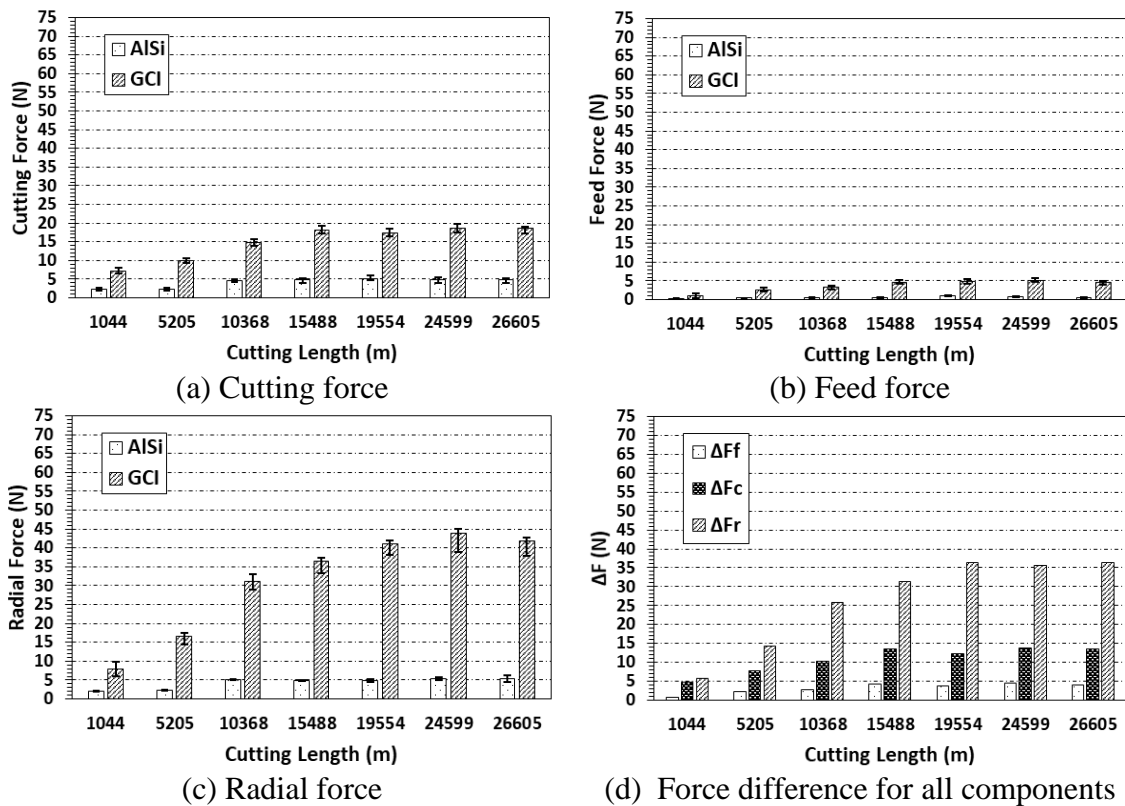


Fig. 43 Variation in force components (a) cutting force, (b) feed force, (c) radial force, and (d) difference in force.

Fig. 43(a) shows that the cutting force increased in both AlSi and GCI until a cutting length of 8.2 km was reached, after which it stabilized. However, the rate of increase in the GCI part was greater than that of the AlSi section. A similar trend can be observed in the feed and radial forces in Fig. 43(b) and Fig. 43(c), respectively.

ΔF_f , ΔF_c , and ΔF_r are shown in Fig. 43(d) throughout the cutting length considered in this study. ΔF_r increased from 5.8 N at 1.1 km to 36.4N at 25.4 km of cutting length. During the same duration, ΔF_f increased from 0.7 N to 3.9 N; ΔF_c increased from 4.7 N to 13.6 N.

Fig. 44 shows the radial force ratio Z, with respect to cutting length. It started at a value of 3.8 at 1.0 km and grew to an average steady-state value of 6.2 after 15.5 km.

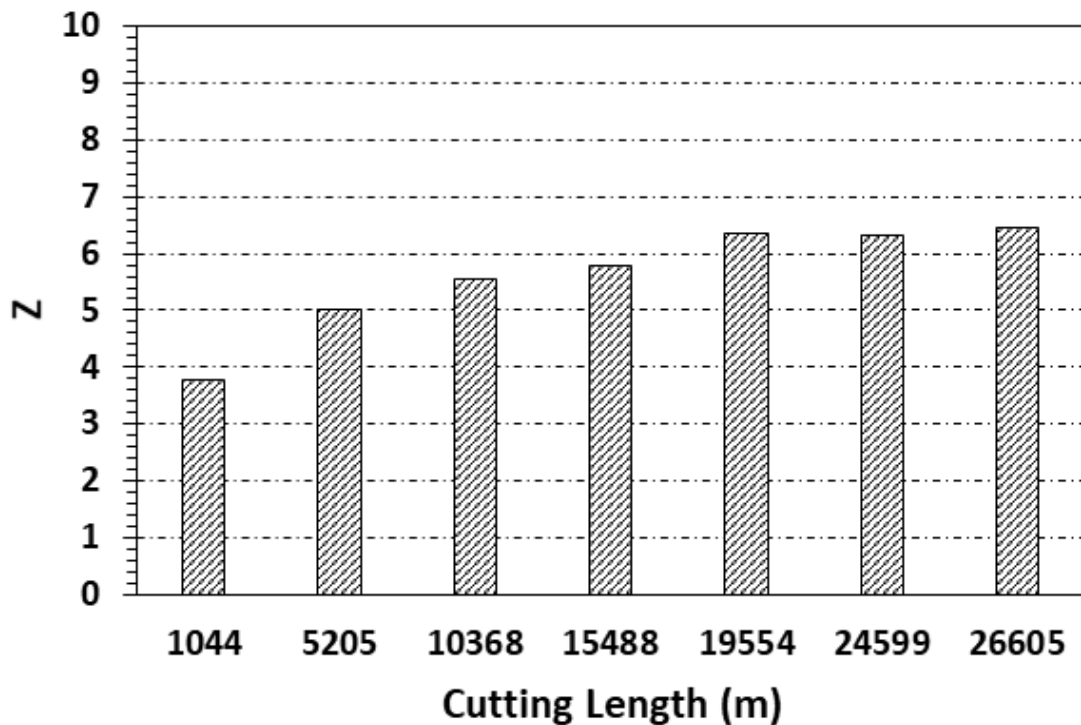


Fig. 44 Progression of Z value with respect to cutting length

To compare the force variation (ΔF) results of the experimental study with the current validation study, the average steady-state magnitudes of force variation, ΔF_r , ΔF_c , and ΔF_f were taken into consideration. **Error! Reference source not found.** lists the results of force variation in both the experimental study (f_1) and validation study (f_2).

Table 17 Comparison of ΔF for f_1 and f_2

Feed	State-state force, N			
	ΔF_r	ΔF_c	ΔF_f	Z
f_1	45.1	19.7	8.3	7.0
f_2	35.5	13	4	6.2
% reduction	22	34	52	11

Chapter 7. Conclusions & Future Work

7.1 Conclusions

The machinability of an AlSi-GCI workpiece using CBN tools under dry cutting conditions was investigated in this study. The results obtained from the machinability study were discussed in detail. A summary of key findings follows:

1. A new robust experimental setup for studying the machinability of an AlSi-GCI bimetal workpiece was developed and produced. The setup consisted of four AlSi and GCI pieces joined mechanically with bolts to form a circular rod. The setup successfully captured the fluctuating cyclic cutting forces.
2. The machinability of the AlSi-GCI workpiece was studied considering two different edge geometries: Tool Design 1 with an unprepared edge and Tool Design 2 with a honed edge. In general, the performance of Tool Design 1 was better in terms of wear behaviour, cutting forces and workpiece surface roughness. However, Tool Design 2 showed an enhanced thermo-mechanical behaviour. The following are the findings of the machinability study:
 - a. The edge geometry had negligible effect on tool wear. The steady-state flank wear for Tool Design 1 and Tool Design 2 were similar, with magnitudes below $80\ \mu\text{m}$ and lasting up to a cutting length of 118 km under the experimental cutting conditions, i.e. a feed of $0.062\ \text{mm/rev}$, a depth of cut of $0.05\ \text{mm}$ and a cutting speed of $630\ \text{m/min}$.

- b. The wear mechanisms of the CBN cutting tools under the preliminary cutting conditions were abrasion, diffusion and attrition wear. Tool Design 2 exhibited greater volumes of adhesion and diffusion.
 - c. Protective Oxide and MnS layers were evident on both Tool Design 1, and Tool Design 2, with higher concentrations present on Tool Design 2.
 - d. The variations of cutting forces, i.e. ΔF_r , ΔF_c , and ΔF_f , along the cutting length, were clearly captured. Among the force components, ΔF_r was by far the most predominant. The variation in radial force ΔF_r was 7% lower for the tool with lower edge radius and greater rake angle (Tool Design 1). Similarly, the radial force ratio Z of Tool Design 1 was 13% lower.
 - e. The workpiece surface roughness was quantified on both AlSi and GCI components of the tool. Tool Design 1 generated slightly better surfaces with Ra of 0.80 μm and 0.35 μm , in the AlSi and GCI parts, respectively. The Ra magnitudes of Tool Design 2 were 25% and 14% higher in the AlSi and GCI parts.
3. A parametric study was performed with the developed FEA model to reduce ΔF_r and Z . The feed was found to have the most significant effect on ΔF_r . The numerical results were experimentally validated with a reduced feed, i.e. $f_2 = 0.045$ mm/rev and all other conditions unchanged from the experimental study. Hence, the average steady-state variation of radial force ΔF_r and the radial force ratio Z , were reduced by 22% and 11%, respectively.

In summary, the contributions of this research included developing a robust and efficient experimental setup and a FEA orthogonal model for machining AlSi-GCI bimetal components. Through experimental and numerical studies, this research established a better understanding of bimetal machining, especially in terms of fluctuating cutting forces, as well as wear and thermo-mechanical behaviours of the CBN cutting tools.

7.2 Future work

Based on the findings of this research, the following are recommendations for future studies:

1. Since the CBN tool wear mechanisms include adhesion and diffusion, the impact of metal cutting fluids on AlSi-GCI bimetallic component machining should be assessed.
2. An investigation of potential tool coatings for AlSi-GCI bimetallic component machining.
3. A study of the fluctuating and radial forces' influence on workpiece dimensional accuracy to increase the tooling efficiency of bimetal cutting processes.
4. A detailed fatigue analysis of cutting tools to understand the effect of the cyclic forces on tool life.

References

- [1] Wright, P. K., and Trent, E. M., 2000, *Metal Cutting*.
- [2] Chowdhury, M., 2016, “WEAR BEHAVIOUR OF COATED CARBIDE TOOLS DURING MACHINING OF Ti6Al4V AEROSPACE ALLOY.”
- [3] Yen, Y. C., Söhner, J., Lilly, B., and Altan, T., 2004, “Estimation of Tool Wear in Orthogonal Cutting Using the Finite Element Analysis,” *Journal of Materials Processing Technology*, **146**(1), pp. 82–91.
- [4] Milton C. Shaw, 2005, *Metal Cutting Principles*, Oxford University Press, Inc.
- [5] Fallböhmer, P., Rodríguez, C. A., Özel, T., and Altan, T., 2000, “High-Speed Machining of Cast Iron and Alloy Steels for Die and Mold Manufacturing,” *Journal of Materials Processing Technology*, **98**(1), pp. 104–115.
- [6] Mod. Cast, 2010, “44th Census of World Casting Production.”
- [7] Gastel, M., Konetschny, C., Reuter, U., Fasel, C., Schulz, H., Riedel, R., and Ortner, H. M., 2000, “Investigation of the Wear Mechanism of Cubic Boron Nitride Tools Used for the Machining of Compacted Graphite Iron and GCI,” *International Journal of Refractory Metals and Hard Materials*, **18**(6), pp. 287–296.
- [8] Abele, E., Sahn, A., and Schulz, H., 2002, “Wear Mechanism When Machining Compacted Graphite Iron,” *CIRP Annals - Manufacturing Technology*, **51**(1), pp. 53–56.
- [9] Liu, J., Yamazaki, K., Ueda, H., Narutaki, N., and Yamane, Y., 2002, “Machinability of Pearlitic Cast Iron With Cubic Boron Nitride (CBN) Cutting Tools,” *Journal of Manufacturing Science and Engineering*, **124**(4), p. 820.

- [10] Thamizhmanii, S., and Hasan, S., 2006, “Analyses of Roughness , Forces and Wear in Turning Gray Cast Iron,” **17**(1), pp. 401–404.
- [11] Sahin, Y., 2008, “Comparison of Tool Life between Ceramic and Cubic Boron Nitride (CBN) Cutting Tools When Machining Hardened Steels,” *Journal of Materials Processing Technology*, **209**, pp. 3478–3489.
- [12] Chakraborty, A., and Ray, K. K., 2000, “Comparative Wear Behavior of Ceramic and Carbide Tools During High Speed Machining of Steel,” **15**(2), pp. 269–300.
- [13] Ammar, H. R., Samuel, A. M., and Samuel, F. H., 2008, “Porosity and the Fatigue Behavior of Hypoeutectic and Hypereutectic Aluminum-Silicon Casting Alloys,” *International Journal of Fatigue*, **30**(6), pp. 1024–1035.
- [14] Warmuzek, M., *Atlas of Microfractographs*.
- [15] Barooah, R., 2018, “INVESTIGATION ON IMPROVED TAPPING LIFE IN AUTOMOTIVE DIE CAST ALUMINUM-SILICON ALLOY APPLICATIONS,” McMaster University.
- [16] Dwivedi, D. K., 2010, “Adhesive Wear Behaviour of Cast Aluminium-Silicon Alloys: Overview,” *Materials and Design*, **31**(5), pp. 2517–2531.
- [17] Ng, E.-G., Sokolowski, D., M., D., Elbestaw, M. A., and Sokolowski, J. H., 2004, “High Speed Face Milling,” *CIRP Annals*, **53**(1), pp. 69–72.
- [18] López de Lacalle, L. N., Lamikiz, A., Sánchez, J. A., and Cabanes, I., 2001, “Cutting Conditions and Tool Optimization in the High-Speed Milling of Aluminium Alloys,” *Proceedings of the Institution of Mechanical Engineers, Part B: Journal of Engineering Manufacture*, **215**(9), pp. 1257–1269.

- [19] Malakizadi, A., Sadik, I., and Nyborg, L., 2013, "Wear Mechanism of CBN Inserts during Machining of Bimetal Aluminum-GCI Engine Block," *Procedia CIRP*, **8**, pp. 188–193.
- [20] Uthayakumar, M., Prabhakaran, G., and Aravindan, S., 2012, "Influence of Cutting Force on Bimetallic Piston Machining by a Cubic Boron Nitride (CBN) Tool," *Materials and Manufacturing Processes*, **27**(October), pp. 1078–1083.
- [21] Uthayakumar, M., Prabhakaran, G., and Aravindan, S., 2009, "Precision Machining of an Aluminum Alloy Piston Reinforced with a Cast Iron Insert," *INTERNATIONAL JOURNAL OF PRECISION ENGINEERING AND MANUFACTURING*, **10**(1), pp. 7–13.
- [22] Uthayakumar, M., Prabhakaran, G., and Aravindan, S., 2008, "Study on Aluminum Alloy Piston Reinforced with Cast Iron Insert," *International Journal of Material Science*, **3**, pp. 1–10.
- [23] Corrê, D. C., Falco, W., Cardoso, S., and Sales, E., 2005, "Machinability of Bimetallic Bearings Using Cemented Carbide Tools: Evaluation of the Wear Mechanisms," *Journal of Materials Processing Technology*, **159**, pp. 435–444.
- [24] Bartarya, G., and Choudhury, S. K., 2012, "Effect of Cutting Parameters on Cutting Force and Surface Roughness during Finish Hard Turning Aisi52100 Grade Steel," *Procedia CIRP*, **1**(1), pp. 651–656.
- [25] Pugh, S., 1996, *Creating Innovative Products Using Total Design: The Living Legacy of Stuart Pugh*, Addison-Wesley.
- [26] Sadeghifar, M., Sedaghati, R., Jomaa, W., and Songmene, V., 2018, "A

Comprehensive Review of Finite Element Modeling of Orthogonal Machining Process: Chip Formation and Surface Integrity Predictions,” *International Journal of Advanced Manufacturing Technology*, **96**(9–12), pp. 3747–3791.

[27] Thakare, A., and Nordgren, A., 2015, “Experimental Study and Modeling of Steady State Temperature Distributions in Coated Cemented Carbide Tools in Turning,” *Procedia CIRP*, **31**, pp. 234–239.

[28] BİL, H., 2003, “SIMULATION OF ORTHOGONAL METAL CUTTING BY FINITE ELEMENT ANALYSIS A.”

[29] Krishnaiah, K., and Shahabudeen, P., 2012, *APPLIED DESIGN OF EXPERIMENTS AND TAGUCHI METHODS*.

[30] Chen, W., 2000, “Cutting Forces and Surface Finish When Machining Medium Hardness Steel Using CBN Tools,” *International Journal of Machine Tools and Manufacture*, **40**(3), pp. 455–466.

[31] Suresh Kannan, I., and Ghosh, A., 2014, “Dry Machining of AA7075 by H-DLC Coated Carbide End Mill,” *Procedia Materials Science*, **5**, pp. 2615–2621.

[32] Fukui, H., Okida, J., Omori, N., Moriguchi, H., and Tsuda, K., 2004, “Cutting Performance of DLC Coated Tools in Dry Machining Aluminum Alloys,” *Surface and Coatings Technology*, **187**(1), pp. 70–76.

[33] Denkena, B., and Biermann, D., 2014, “Cutting Edge Geometries,” *CIRP Annals - Manufacturing Technology*, **63**(2), pp. 631–653.